

Advanced Optofluidic Sensing and Imaging
Technologies

ADVANCED OPTOFLUIDIC SENSING AND IMAGING
TECHNOLOGIES

By

Bo Xiong, M.Eng

A Thesis

Submitted to the School of Graduate Studies

In Partial Fulfilment of the Requirements for the Degree

Doctor of Philosophy

McMaster University

©Copyright by Bo Xiong, December 2020

Abstract

Water contaminations are currently threatening ecosystems and human health on a world-wide scale. Monitoring the water quality is one of the most essential steps to provide better understanding and mitigation of water contamination. Among the water quality monitoring techniques, optofluidic technologies have created a burgeoning number of novel devices designed to test water quality in an efficient and portable format. However, current optofluidic devices have yet to be successfully translated to onsite monitoring applications due to their high cost, high maintenance and dependence on delicate laboratory instruments or bulky instruments.

In this work, we developed two optofluidic platforms for onsite water quality monitoring: a fluorescence-based optofluidic platform for chemical analysis and an imaging-based optofluidic platform for microbe detection. Several technologies associated to optical sensing modules were developed to overcome the above challenges, making the optofluidic platforms compatible with onsite monitoring applications. First, excitation coupling mechanism and frequency domain time-resolved fluorescence (TRF) were developed on the fluorescence-based optofluidic platform to improve sensing sensitivity and stability, while reducing dependence on costly instruments. Their effectiveness was demonstrated by dissolved oxygen (DO) measurements and ray-tracing simulation. Second, a low-cost and portable imaging system with dual modalities were developed on the imaging-based optofluidic platform. Thus, both morphological features and fluorescent features can be observed for microbe detection without using bulky microscope setups. The effectiveness of dual-modality imaging was demonstrated by experimental results of phytoplankton analysis. Third, a fluorescence lifetime imaging (FLIM) approach was developed under a low-cost (Complementary metal–

oxide–semiconductor) CMOS format. This approach enables integrating FLIM module in portable optofluidic platforms for onsite monitoring.

These advances bring optofluidic platforms closer to realizing the requirements of onsite water quality monitoring and provide a clear picture for future improvements and research directions.

Acknowledgments

I would like to thank my supervisor Dr. Qiyin Fang for his support and advice. I am grateful to have worked under a supervisor who provided me opportunities to study what I am interested in. I also want to thank the other members of my supervisory committee: Dr. Herb Schellhorn and Dr. P. Ravi Selvaganapathy. My research progress always received a significant boost following a committee meeting.

I feel lucky to have been surrounded by a great collection of colleagues from our lab group. I would like to thank Eric Mahoney, Ian Phillips, Morgan Richards, Michael Zon, Tianqi Hong, Nehad Hirmiz, Anthony Tsikouras, Fahad Aljekhedab, Fares Badr, Alex Ianovski, Colleen Chau, Jessica Kun, Jacob Saunders, Melissa Temkov and Ishita Paliwal. I value their help about my research and making my life easier and more enjoyable during my PhD studying. Moreover, I would like to thanks to my friends Jie Yang, Yushan Zhang, and Wei Jiang who have always been helpful throughout these years at McMaster University.

Thank you to my parents as well, who have always been supportive of me. And a special thank you to my girlfriend Lin Liu, for always being by my side through every stage of the Ph.D.

Table of Contents

ABSTRACT	III
ACKNOWLEDGMENTS.....	V
TABLE OF CONTENTS	VI
LIST OF FIGURES	IX
LIST OF TABLES	XI
LIST OF ABBREVIATIONS.....	XII
CHAPTER 1. INTRODUCTION	1
1.1 MOTIVATION	1
1.2 OPTOFLUIDICS FOR WATER QUALITY MONITORING	3
1.2.1 Chemical Analysis.....	4
1.2.2 Microbe Detection.....	5
1.2.3 Requirements of Onsite Monitoring.....	7
1.2.4 Summary.....	8
1.3 OPTOFLUIDIC FLUORESCENCE SENSING.....	9
1.3.1 Architectures of Optofluidic Fluorescence Sensing.....	9
1.3.2 Fluorescence Measurement Methods.....	12
1.3.3 Frequency Domain Measurements	13
1.4 OPTOFLUIDIC IMAGING.....	16
1.4.1 Conventional Imaging	16
1.4.2 Lensless Imaging.....	20
1.4.3 Miniaturization of Imaging System	24
1.5 ROADMAP TOWARD ONSITE MONITORING.....	25
1.6 THESIS OVERVIEW.....	29
1.7 THESIS OUTLINE	30
REFERENCES	32
CHAPTER 2.....	40
INTRODUCTION TO PAPER I:	41

CONTENTS OF PAPER I.....	42
ABSTRACT	42
2.1 INTRODUCTION	43
2.2 MATERIALS AND METHODS.....	46
2.2.1 Reagents	46
2.2.2 Sensor Design	46
2.2.3 Chip Fabrication.....	47
2.2.4 Simulation and Optimization	47
2.3 EXPERIMENTAL SETUP.....	50
2.4 RESULTS AND DISCUSSION	51
2.4.1 Enhancement of Fluorescence Signal	51
2.4.2 DO Sensing Performance.....	52
2.4.3 Accelerated Photobleaching Test.....	57
2.5 CONCLUSION	58
REFERENCES	60
CHAPTER 3.....	64
INTRODUCTION TO PAPER II:.....	65
CONTENTS OF PAPER II.....	66
ABSTRACT	66
3.1 INTRODUCTION	66
3.2 MATERIALS AND METHODS.....	69
3.2.1 Materials	69
3.2.2 System Design.....	70
3.2.3 Microfluidic Chip Design	72
3.2.4 Image Processing Algorithms.....	73
3.2.5 Sample Preparation.....	74
3.3 RESULTS	75
3.3.1 Particle Classification.....	75
3.3.2 Particle Counting.....	79
3.4 DISCUSSION	82
3.4.1 Performance of Fluorescence Camera	82
3.4.2 Volumetric Throughput.....	84
3.4.3 Analysis of Natural Water	84
3.5 CONCLUSION	85
REFERENCES	86

CHAPTER 4.....	91
INTRODUCTION TO THE PAPER III:	92
CONTENTS OF PAPER III	93
ABSTRACT	93
4.1 INTRODUCTION	93
4.2 MATERIALS AND METHODS.....	94
4.3 RESULTS AND DISCUSSION	98
4.4 CONCLUSION	102
REFERENCES	103
CHAPTER 5. SUMMARY AND FUTURE WORK.....	106
5.1 DISCUSSION AND FUTURE WORK	106
5.1.1 Fluorescence-based Optofluidic Platform.....	106
5.1.2 Imaging-based Optofluidic Platform	110
5.1.3 FLIM under Low-Cost CMOS Format	117
5.2 CONTRIBUTION	121
5.3 CONCLUSION	122
REFERENCES	123

List of Figures

Figure 1-1 Schematic of optofluidic sensing with autofluorescence	10
Figure 1-2 Schematic of optofluidic sensing with fluorophore functionalized film	11
Figure 1-3 Schematic of optofluidic sensing with fluorescence assay	12
Figure 1-4 Schematic of time domain and frequency domain measurements.....	14
Figure 1-5 Schematic of a simple microscope	17
Figure 1-6 Schematic of Rayleigh criterion.....	18
Figure 1-7 Gaussian beam focusing with a convex lens.....	19
Figure 1-8 Schematic of lensless shadow imaging.....	21
Figure 1-9 Schematic of lensless fluorescence imaging	22
Figure 1-10 Schematic of lensless holographic imaging	23
Figure 1-11 A roadmap towards onsite water quality monitoring.....	28
Figure 2-1 Schematic of fluidic module	47
Figure 2-2 Ray tracing models and simulation results	49
Figure 2-3 Customized frequency domain DO setup	51
Figure 2-4 Comparison of fluorescence intensity between two excitation configurations: TIR and no TIR.....	53
Figure 2-5 Measured phase shift as a function of DO concentration.....	54
Figure 2-6 Repeatability results of DO measurements using two samples	56
Figure 2-7 Response curves of frequency domain DO device when switching between two samples at two different oxygen concentration.....	57
Figure 2-8 Accelerated photobleaching test of frequency domain DO device.....	58
Figure 3-1 Description of experimental setup.....	70
Figure 3-2 Four frames captured at 0 s, 0.2 s, 0.4 s, and 0.6 s respectively	71
Figure 3-3 Description of chip design	72
Figure 3-4 The logic flow of image processing algorithms	74
Figure 3-5 Overview of particle dataset	76
Figure 3-6 Images of 10 μm polystyrene bead, Chlamydomonas and Euglena	77
Figure 3-7 The Chlamydomonas count per 150 μl in the four samples	80
Figure 3-8 The measurement results of mixed samples.....	81
Figure 3-9 Images captured during natural water test	83

Figure 3-10 Images captured during natural water test	85
Figure 4-1 Conceptual design of the fluorescence lifetime imager	96
Figure 4-2 Luminescence lifetime calculation in the captured images	98
Figure 4-3 Measured luminescent lifetime images and raw images	100
Figure 4-4 Measured luminescence lifetime curve of two sub-images	102
Figure 5-1 A potential solution for coupling of emission light	109
Figure 5-2 Schematic of compact design for fluorescence sensing	110
Figure 5-3 Objected detection using HOG and SVM	112
Figure 5-4 Two potential architectures for rapid holographic reconstruction	115
Figure 5-5 Illustration of a time gated method for TRF	119
Figure 5-6 Detection of long-lifetime fluorophores with suitable time-gated window	120
Figure 5-7 A potential optofluidic design that use the FLIM approach under a low-cost CMOS format	121

List of Tables

Table 1-1 Comparison of methods for chemical analysis in optofluidic devices.....	8
Table 1-2 Comparison of methods for microbe detection in optofluidic devices	9
Table 3-1 Ingredient of samples	75
Table 3-2 Confusion matrix of classifier using lensless images and fluorescent images	78
Table 3-3 Confusion matrix of classifier using fluorescent images	79
Table 3-4 Confusion matrix of classifier using lensless images	79

List of Abbreviations

BOD	Biochemical oxygen demand
CCD	Charge-coupled device
CMOS	Complementary metal–oxide–semiconductor
CNN	Convolutional neural network
CSR-DCF	Discriminative correlation filter with channel and spatial reliability
DO	Dissolved oxygen
DoF	Depth of focus
ERS	Electronic rolling shutter
FLIM	Fluorescence lifetime imaging
FoV	Field of view
FPN	Feature pyramid network
HOG	Histogram of oriented gradients
PDMS	Polydimethylsiloxane
PLIM	Phosphorescent lifetime imaging
PS	Polystyrene
R-CNN	Regions with convolutional neural networks
SBR	Signal-to-background ratio
SD	Standard deviation
SERS	Surface-enhanced Raman scattering
SNR	Signal-to-noise ratio
SPR	Surface plasmon resonance
SVM	Support vector machine
TCSPC	Time-correlated single-photon counting
TIR	Total internal reflection
TRF	Time resolved fluorescence

Chapter 1. Introduction

1.1 Motivation

Optofluidics is a research area that combines optics and microfluidics. Optofluidic devices can analyze fluidic sample using the integration of optical technologies on microfluidic platforms. Optofluidic technologies provide several advantages including portable devices, high throughput, enhanced sensitivity, fast response, reduced reagent consumption, and low-cost [1, 2].

Optofluidic devices have found a wide range of applications. Specifically, it is well-suited for analysis of biological and chemical samples of small volume [3]. The emergence of microfluidics technologies allows the precise processing or manipulation of small-volume fluid sample [4]. Multiple optical properties have been used for chemical analysis in the optofluidic devices, such as fluorescence, absorption, scattering, Raman scattering, refraction index, and polarization [5]. Imaging technologies and particle manipulation technologies contribute to biological analysis with optofluidic devices [6,7]. Thus, optofluidic devices is suitable for water quality tests which commonly require chemical and biological analysis.

Many water quality tests are run in the lab where manual lab work and transportation of water sample are needed. Onsite water quality monitoring refers to the continuous water quality tests performed at the site where the trial is being conducted without the sophisticated laboratory equipment. Realizing onsite water quality monitoring is challenging but has significant benefits. For instance, onsite monitoring contributes to the optimization of water treatment processes [8], early warning of and better mitigation of health and environmental issues [9].

Optofluidic devices are promising for onsite water quality monitoring, since a variety of optofluidic devices for water quality tests are demonstrated in the lab and their advantages match some of the general requirements for onsite monitoring

devices, such as low cost, portable, and autonomous operation [10-12]. Water quality tests includes two main categories: (a) chemical analysis, such as DO sensing, heavy metal ion testing; (b) microbe detection, such as E. coli and cyanobacteria. Fluorescence is widely used in chemical analysis since fluorescence sensing presents advantages of long working lifetime and high sensitivity. Thus, fluorescence-based optofluidic devices has been developed for sensing a variety of chemical elements in the water, such as dissolved oxygen [13], ammonia [14], and chlorine [15]. Imaging and microscopy technologies have been demonstrated as a powerful tool for microbe detection. Imaging enables analyzing the microbe properties of absorption, scattering, and fluorescence at the cellular level and observation of morphology which are crucial to microbe recognition. Thus, imaging-based optofluidic devices have been developed for detecting various microbes in the water, such as algae [16], bacteria [17], and parasites [18].

Many optofluidic devices for chemical analysis or microbe detection have been reported. However, these proof-of-concept devices often remain in academic laboratories, and their progression to real-world onsite monitoring is still very limited [2]. A main reason is that the current optical sensing modules in the optofluidic devices are not suitable for onsite monitoring due to a tradeoff between miniaturization and sensing performance [5, 7, 10, 19]. Although some optical components and electronic components can be integrated in an optofluidic chip, many optofluidic devices still require manual operation and sophisticated laboratory instruments to achieve adequate optical sensing performance, such as spectrometers [20], photomultiplier tubes [21], and microscopes [7]. Some optofluidic devices have already integrated a miniaturized optical sensing module. However, miniaturized optical sensing modules commonly lack tunability or resistance to environmental disturbance, and it is difficult to keep their sensing performance optimal in the field [19]. These optofluidic devices are “chip-in-a-lab” [22] and not suitable for onsite monitoring applications. The goal of this research is to make optofluidic devices compatible with onsite water quality monitoring.

Several optofluidic technologies are developed to combat the main limitation of optical sensing module, i.e., tradeoff between miniaturization and sensing performance.

1.2 Optofluidics for Water Quality Monitoring

Optofluidic device technology underwent a rapid development in the recent two decades. Numerous optofluidic components have been developed such as optofluidic waveguides [19], on-chip lens [23], on-chip interferometers [24], miniaturized diode lasers [25], low-cost photodetectors [25], and low-cost CMOS imagers [26]. Recent advances in optical materials such as nanoparticles [27], advanced fluorophores [28] and fluorescence super-quenchers [29] have improved the sensing performance. Integrating optical sensing in the microfluidic devices results in several advantages, such as device portability, enhanced sensing sensitivity, reduced reagent consumption, low instrumentation cost, and low operating costs. Thus, optofluidic devices show promise in many fields such as environment monitoring [10, 11], healthcare monitoring [12, 30], food monitoring [12], drug screening [31].

A common application of optofluidic devices is water quality test and monitoring. The current water quality tests and monitoring can be divided into three categories: (a) manually sampling and off-site analysis with laboratory instruments, (b) manually sampling and onsite testing with portable devices, and (c) Onsite monitoring with automated devices. Off-site analysis with laboratory instruments is inefficiency. Moreover, it cannot provide real-time results which are necessary for process control. Manually testing with portable devices still requires manual labour and it is difficult to achieve continuous measurement. Onsite monitoring minimizes the cost of labour. And it can provide a large amount of data in real-time and further helps decision making for health and environmental issues [32, 33].

Chemical pollutants and microbial pollutants are two main issues in water

quality. According to guidelines for Canadian drinking water quality [34], more than 90 chemical parameters need to be tested. Moreover, routine tests of harmful microorganisms such as giardia, cryptosporidium, enteric viruses, E. coli, total coliforms are recommended. The common optofluidic technologies used in chemical analysis and microbe detection are described in the following section.

1.2.1 Chemical Analysis

Chemical analysis refers the detection and quantification of a wide range of molecules or ions dissolved in water. Detection of chemical pollutants, such as heavy metal ions and organic toxins, is necessary for ensuring water is safe to drink and use. Furthermore, many chemical elements are important indicators of water quality such as dissolved oxygen in surface water and free chlorine in drinking water. A variety of sensing mechanisms have been used in optofluidic devices for chemical analysis.

(i) Colorimetric methods

Colorimetric methods provide chemical analysis by sensing the color change of reagents caused by chemical reaction. Colorimetric methods enjoy several advantages including low cost, high specificity, and simplicity. Thus, colorimetric optofluidic devices have been used for a variety of water quality tests such as heavy metal ion [35], Nitrate [36], and phosphate tests [37]. Moreover, the sensitivity of colorimetric methods can be enhanced with recent micro and nano technologies such as microscale resonators [37] and functionalized gold nanoparticles [38]. However, these methods consume chemical reagents and therefore not suitable for continuous monitoring.

(ii) Fluorescence methods

Fluorescence-based sensing can rely on a variety of fluorophore features, such as fluorescence intensity, lifetime, spectrum, and decay curves [39]. For instance, dissolved ammonia can be quantified by measuring the fluorescence lifetime of extrinsic fluorophore [14], and heavy metal ions can be detected by

monitoring the reduction of fluorescence intensity caused by quenching [40]. Fluorescence sensing enjoys high sensitivity since the background is relatively dark. When autofluorescence and reusable fluorescent film are used, fluorescence sensing does not consume chemical reagent, providing a unique advantage in continuous monitoring. Fluorescence sensing techniques will be further described in Section 1.3.

(iii) Surface Plasmon Resonance (SPR)

SPR-based sensors measure the changes in the refractive index on the sensing surface. These changes are caused by binding between target analytes and a metal film which is typically coated with antibodies. Due to high sensitivity and high selectivity, SPR-based sensors have been used in the detection of trace amounts of organic pollutants such as microcystins [41] and atrazine [42]. However, miniaturization of SPR-based optofluidic sensors can be an issue. Furthermore, the majority of SPR sensors are not suitable for continuous monitoring since the antibody functionalized film needs to be replaced or reset before the next measurement.

(iv) Surface-enhanced Raman scattering (SERS)

SERS is a technology that dramatically enhances Raman scattering using metal nanostructures. Due to its high sensitivity, SERS-based sensors have been developed for detecting trace amounts of water contamination, such as As (III) ions [43] and Malachite green [44]. However, SERS is highly sensitive to environmental changes. Moreover, integrating SERS within a portable optofluidic platform could be difficult due to the usage of bulk instrumentations, such as spectrometers.

1.2.2 Microbe Detection

Detection of microbes such as bacteria, viruses, and parasites are widely required in the water quality tests and monitoring. For instance, the parasites,

enteric viruses, *E. coli*, and total coliforms in the drinking water need to be monitored [34]. In the rivers or lakes, harmful algae were monitored to secure water quality and provide warnings of algae bloom [32]. During wastewater treatments microbial community were characterized for optimization of process control [33]. A variety of sensing mechanisms have been used in optofluidic devices for microbe detection.

(i) Flow cytometry

In the conventional flow cytometry, particles are hydrodynamically focused into a narrow stream. Thus, individual particles can be analyzed and characterized using forward scattering, side scattering and fluorescence signals. With the development of microfluidic techniques some components, such as flow cells and lenses, can be integrated on a chip to improve system portability. Many microfluidic flow cytometry devices have been developed for the detection of various microbes in the water such as algae [45], *E. coli* [46], and enteroviruses [47]. However, the narrow stream limits the volumetric throughput. Furthermore, conventional flow cytometry cannot observe morphology features which are important to microbial identification and characterization.

(ii) Imaging-based flow cytometry

Imaging or microscopy can be applied on flow cytometers, allowing the observation of cell morphology. Imaging-based flow cytometers have been used to detect microbes for water quality tests, such as algae [16], bacteria [48], and parasites tests [49]. Recent advances in imaging processing algorithms promote the performance of microbial classification and analysis. Moreover, portable image-based flow cytometers can be realized by various advanced imaging techniques, which are described in detail in Section 1.4.

(iii) Immunoassay-based sensing.

Microbes can be analyzed by measuring the concentration of characteristic biomolecules in the fluidic sample using antibodies or antigens. The reaction between the immunoassay and characteristic biomolecules results in a change

in color, fluorescence, or refraction index. Then, the target microbes with the characteristic biomarkers can be quantified. For instance, fluorescently labeled antibodies can be used to detect *E. coli* [50]. SPR-based sensors that use antibody modified nanostructures can detect bacterial contamination [51]. Antibody modified nanoparticles can be used to detect *Salmonella* with colorimetric methods [52]. Immunoassay-based sensing typically enjoy high selectivity. However, Immunoassay-based sensing consumes reagents, making it difficult to be adopted in optofluidic systems for continuous monitoring applications.

1.2.3 Requirements of Onsite Monitoring

Here, we conclude five requirements for devices that conduct onsite water quality monitoring.

First, the devices should be capable of continuous monitoring and autonomous operations. These operations include sample reloading, testing, self-calibration, etc. When chemical reagents need to be added during testing, continuous monitoring and autonomous operations become more difficult due to reagent consumptions and additional reagent operations.

Second, the devices should have adequate sensing performance, including sensing sensitivity, sensing selectivity, response time, and throughput, etc.

Third, the cost of the device's instrumentation and operation should be kept relatively low. The cost issue could become more serious when a large number of devices are needed to build a distributed monitoring system.

Fourth, the devices should be portable. Since the devices are deployed in the field, bulky devices or benchtop instruments are not suitable.

Fifth, the sensing devices should be low maintenance. The optofluidic devices could be deployed in the remote areas, such as sewer, river bottom, and ocean. Thus, the sensing devices should not need frequently optical alignment,

calibration, reagent refill, component replacement, or cleaning.

1.2.4 Summary

Table 1-1 summarizes advantages and disadvantages of common optofluidic methods for chemical analysis. SPR and SERS based sensors enjoy high selectivity, however, these devices typically consume expensive reagents and require delicate lab instruments to achieve high sensing performance. Colorimetric methods are commonly used in portable devices since they are relative low-cost and simple. However, colorimetric method consumes chemical reagents, making it difficult in continuous monitoring. Fluorescence-based optofluidic platforms are suitable in many onsite monitoring applications, since fluorescence sensing is sensitive, simple, and enable continuous monitoring without consumption of reagent. However, fluorescence sensing often suffer from photobleaching issues. Furthermore, lacking intrinsic fluorophore and available extrinsic fluorophores could limit its applications.

Table 1-1 Comparison of methods for chemical analysis in optofluidic devices

Methods	Advantages	Disadvantages
Colorimetric	<ul style="list-style-type: none"> • Simple device • Portable device 	<ul style="list-style-type: none"> • Consume reagents
Fluorescent	<ul style="list-style-type: none"> • Simple device • Portable device 	<ul style="list-style-type: none"> • Limited to fluorophores
SPR	<ul style="list-style-type: none"> • High sensitivity • High selectivity 	<ul style="list-style-type: none"> • Bulky device • High cost • Consume reagent
SERS	<ul style="list-style-type: none"> • High selectivity 	<ul style="list-style-type: none"> • Bulky device • High cost • Consume reagent

Table 1-2 summarizes advantages and disadvantages of current optofluidic

methods for microbe detection. Although immunoassay-based sensing is suitable for portable devices, it is difficult to detect rare microbes present in the sample due to their low sensitivity and volumetric throughput. Conventional flow cytometers and imaging-based flow cytometers are sensitive since they can detect a single cell or particle as it flows through a fluidic channel. Compared with conventional flow cytometers, imaging-based flow cytometers show two main advantages: (i) capability of observing morphological features which contributes to microbe identification; (ii) high-throughput since a wide and thick fluidic stream can be used. However, conventional imaging systems require expensive objective lens and complex fine adjustments to provide high-spatial resolution. Miniaturization of imaging systems, while keeping adequate imaging performance is still a challenge [7, 19].

Table 1-2 Comparison of methods for microbe detection in optofluidic devices

Methods	Advantages	Disadvantages
Flow cytometry	<ul style="list-style-type: none"> Cellular level analysis 	<ul style="list-style-type: none"> Consume sheath fluid Bulky device
Imaging-based	<ul style="list-style-type: none"> Cellular level analysis 	<ul style="list-style-type: none"> Bulky device
Flow cytometry	<ul style="list-style-type: none"> Morphology analysis High volumetric throughput 	
Immunoassay-based sensing	<ul style="list-style-type: none"> Simple device Portable device 	<ul style="list-style-type: none"> Low volumetric throughput Low sensitivity Consume reagent

1.3 Optofluidic Fluorescence Sensing

1.3.1 Architectures of Optofluidic Fluorescence Sensing

Fluorescence sensing has been widely used in optofluidic devices. Various optofluidic architectures have been developed. These architectures can be divided into three broad categories.

(i) Autofluorescence architectures

Autofluorescence is the emission of light from organisms and biological structures under excitation lights. As shown in **Figure 1-1**. Detection of autofluorescence does not require fluorescence labels or additional chemical reagents, thus, measuring autofluorescence can reduce the system complexity and cost which are desirable in onsite monitoring. However, many target analytes cannot emit autofluorescence with distinguishing features, limiting the usages of autofluorescence.

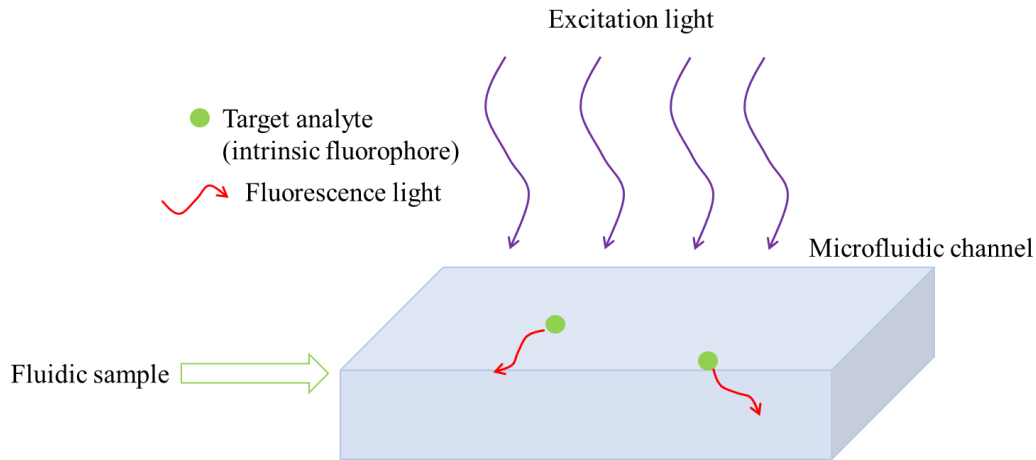


Figure 1-1. Schematic of optofluidic sensing with autofluorescence

(ii) Fluorophore functionalized films

Many fluorescence-based optofluidic devices rely on fluorophore functionalized films. The fluorescence emitted from the film can be turned-on or turned-off by physical or chemical reaction between the target analyte and the fluorophore functionalized film, as shown in **Figure 1-2**. Thus, the target analyte in the fluid sample can be quantified. Several strategies have been developed to make films reusable, such as using collisional quenching [53], using reversible chemical reactions [54], and resetting the film by chemical assays [55]. Moreover, recent advances in nanotechnologies can enhance the

light-fluorophore interaction and improve the sensing sensitivity [27]. However, fluorophore functionalized films create some issues for long-term monitoring such as dye leaching, film aging, and photobleaching problems.

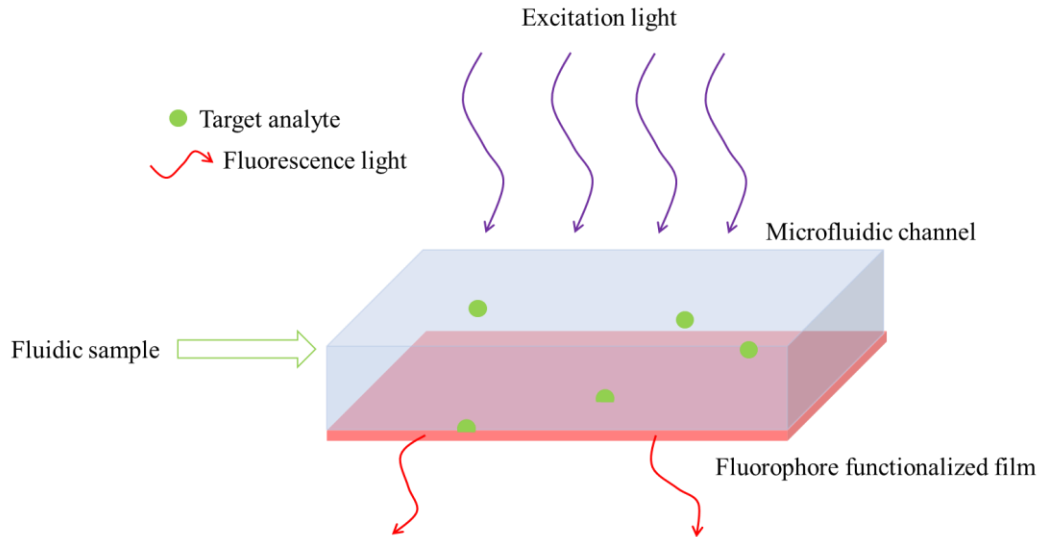


Figure 1-2. Schematic of optofluidic sensing with fluorophore functionalized film

(iii) Fluorescence liquid assays

Many optofluidic sensing devices require additional fluorescence liquid assays [19, 50]. The fluorescence can be turned on or turned off by the physical or chemical reaction between the target analyte and the extrinsic fluorophore in the assay, as shown in **Figure 1-3**. This requires precise delivery of the fluidic sample as well as the fluorescence assay, increasing the system cost and complexity. Furthermore, reagent consumption could lead to problems in continuous monitoring.

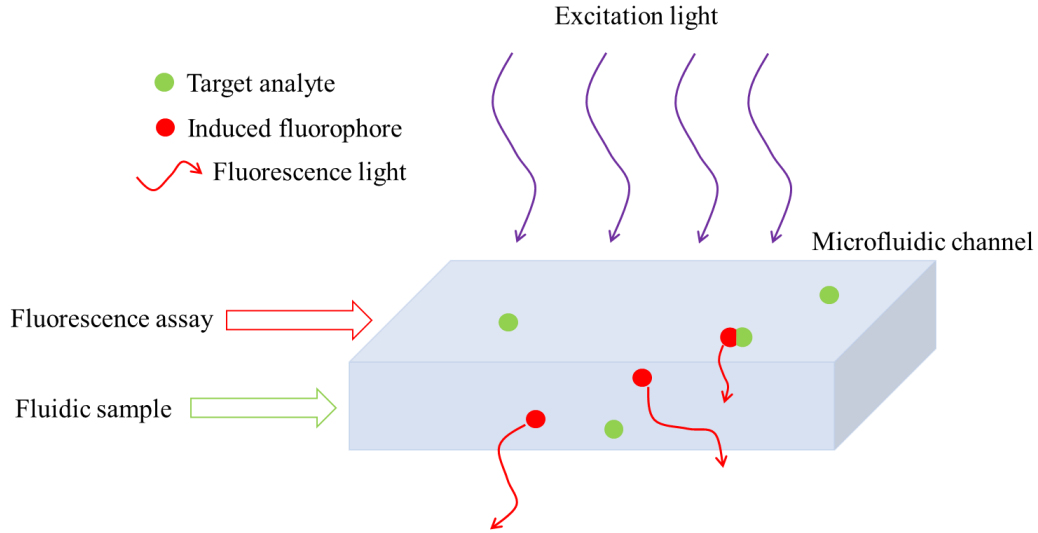


Figure 1-3. Schematic of optofluidic sensing with fluorescence assay

1.3.2 Fluorescence Measurement Methods

Both static fluorescence approaches and time resolved fluorescence (TRF) approaches have been used to analyze fluorophores [56]. Static fluorescence approaches measure the fluorescence intensity; thus, it suffers from intensity variation artifacts which commonly occur in onsite monitoring. On the other hand, TRF approaches retrieve lifetime features from dynamic fluorescence decay. TRF approaches are attractive in onsite monitoring since intensity variations caused by photobleaching, dye leaching, detector drift, laser output fluctuation, and change in optical path have less effects on the fluorescence lifetime. Several TRF approaches have been developed [56].

(i) Time-correlated single-photon counting (TCSPC)-based detection

In a TCSPC system, the sample is excited by a pulsed laser with a high repetition rate. The emission is collected one photon at a time by either photomultiplier tube (PMT) or single-photon avalanche diodes (SPAD). Then, a histogram of the photons with respect to their arrival time is built to retrieve the lifetime. TCSPC can be applied in time-resolved fluorescence imaging by

using SPAD arrays or a point detector with raster scanning. TCSPC provides high temporal resolution and is capable of weak fluorescence detection.

(ii) Time gated method

In the time-gated sampling method, a high-speed camera with a global shutter, or an image intensifier, is used to collect emission light. The exposure time window (“time-gate”) is synchronized with light sources and scans along the fluorescence decay. Then, the fluorescence decay curve can be reconstructed after repetitively sampling. Time-gated methods provide a good spatial resolution since cameras with high pixel-counts can be used.

(iii) High speed sampling

In this method, the emission signal is detected by point detectors and then acquired by high speed data acquisition devices, such as digitizers. This method is simple and fast since fluorescence decay can be retrieved without repetitively sampling. However, the temporal resolution of measured fluorescence decay is limited by the max sampling rate of the acquisition devices. Combined with raster scanning, high speed sampling can be applied in time-resolved fluorescence imaging.

1.3.3 Frequency Domain Measurements

Both time domain measurements and frequency domain measurements are widely used in TRF [56]. In time domain measurements, a pulsed light source is used to excite the fluorescent sample, as shown in **Figure 1-4** (a). Then the time depended emission intensity is measured to calculate the lifetime. In the frequency domain measurements, the intensity of excitation light is modulated, as shown in **Figure 1-4** (b). The fluorescence decay can cause a phase delay of emission signal as well as a decrease in the amplitude of the modulated emission signal. Therefore, the fluorescence lifetime can be calculated by measuring phase shift or modulation information.

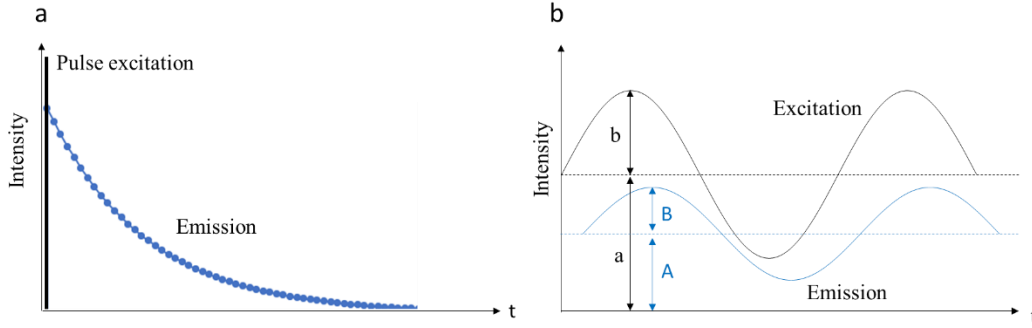


Figure 1-4. Schematic of time domain and frequency domain measurements. (a) The excitation and emission signal in the time domain measurements. (b) The excitation and emission signal in the frequency domain measurements.

In the frequency domain measurements, the relationship between the excitation and emission can be expressed:

$$y(t) = x(t) \otimes h(t) \quad (1.3.1)$$

Here, $h(t)$ is pulse response function which is fluorescence decay curve. $x(t)$ is the input signal, i.e., intensity of excitation light. $y(t)$ is the output signal, i.e., intensity of emission light. Measurement of phase shift is simple and widely used in the frequency-domain measurements. In the simplified model, the fluorescence decay can be regard as an exponential decay:

$$h(t) = \alpha \exp\left(-\frac{t}{\tau}\right) \quad (1.3.2)$$

Here, t is time, τ is meaning of the fluorescence lifetime, α is a coefficient depends on absorption and quantum yield. Thus, the Eq. (1.3.1) and Eq. (1.3.2) can be transformed to frequency domain:

$$Y(f) = X(f) * H(f) \quad (1.3.3)$$

$$H(f) = \frac{\alpha\tau(1-i2\pi f\tau)}{1+(2\pi f)^2\tau^2} \quad (1.3.4)$$

Here, $Y(f)$, $X(f)$ and $H(f)$ are the Fourier transform results of $y(t)$, $x(t)$, $h(t)$. Assuming that input signal is sinusoidal waves with a frequency of f_0 , the phase shift $\phi(f_0)$ between the excitation light and emission light can be expressed:

$$\phi(f_0) = \tan^{-1}\left(\frac{I[H(f_0)]}{R[H(f_0)]}\right) = \tan^{-1}(2\pi f_0\tau) \quad (1.3.5)$$

Here, $I[H(f_0)]$ and $R[H(f_0)]$ refer imaginary and real components of $H(f_0)$. Therefore, the fluorescence lifetime τ is can be calculated using the selected f_0 and measured phase shift $\phi(f_0)$. Alternatively, the fluorescence lifetime can be qualified by measuring demodulation factor. Assuming that input signal is sinusoidal waves with a frequency of f_0 , a DC offset of a and a modulation amplitude of b , demodulation factor M is defined:

$$M = \frac{\left(\frac{B}{A}\right)}{\left(\frac{b}{a}\right)} \quad (1.3.6)$$

Here, A and B are the DC offset and the amplitude of output signal. Considering the Fourier transform results of sinusoidal waves, M can be rewritten:

$$M = \frac{\left(\frac{B}{b}\right)}{\left(\frac{A}{a}\right)} = \frac{\left(\frac{|Y(f_0)|}{|X(f_0)|}\right)}{\left(\frac{|Y(0)|}{|X(0)|}\right)} \quad (1.3.7)$$

Considering Eq. (1.3.3) and Eq. (1.3.4), M can be rewritten:

$$M = \frac{|H(f_0)|}{|H(0)|} = \frac{1}{\sqrt{1+(2\pi f_0)^2 \tau^2}} \quad (1.3.8)$$

Therefore, the fluorescence lifetime τ is can be calculated using the selected f_0 and measured demodulation factor M .

Frequency domain measurements can be implemented with time gated method and high-speed sampling method. With a modulated excitation light with a specific frequency, both phase shift and demodulation factor can be calculated by analyzing the measured emission signals, thus the fluorescence lifetime can be estimated. Moreover, frequency domain methods can be achieved with gain-modulated detectors. The gain of image intensifier or the gain of photodetector is modulated with a same frequency as the excitation light. Thus, the measured signal is maximum when the modulated gain and emission lights are in-phase; the measured signal is minimum when the modulated gain and emission lights are out-of-phase. Therefore, both phase shift and demodulation factor can be calculated by tuning the phase of gain's modulation.

Frequency domain measurements have been used to study multi-exponential intensity decays. A common approach is phasor analysis which makes

use of the properties of the Fourier transform of exponential decay. Another common approach is analyzing the frequency response of the sample. In this method, phase shift and demodulation factor are measured over a wide range of frequencies, thus the multiple lifetime components and their contributions can be retrieved from the frequency response curves.

Time domain measurements and frequency domain measurements have comparable precision [57]. From the instrumental point of view, frequency domain methods can reduce the TRF system complexity and cost. Frequency domain method uses an intensity-modulated light source instead of an expensive pulse laser. Furthermore, the continuous excitation light provides more energy, resulting in a high emission intensity. Thus, cheaper detectors with relative low sensitivity and slow response time can be used in the frequency domain TRF.

1.4 Optofluidic Imaging

The imaging technologies used in optofluidic devices can be divided into two broad categories. The first category is conventional imaging, which uses lenses to magnify the sample under observation. The second category is lensless imaging, in which samples are placed closer to the image without lens focusing.

1.4.1 Conventional Imaging

Conventional imaging typically relies on microscopes which use a combination of lenses to achieve a high magnification and a high spatial resolution. **Figure 1-5** shows a schematic of a simple microscope. An objective lens projects an intermediate image of the sample onto a plane. Then, this intermediate image is projected once again by an ocular for final imaging or viewing. The magnification of the microscope is equal to the production of magnification of the objective lens and magnification of the ocular. A typical objective magnification ranges from 4x

to 100x. A typical ocular magnification is 10x. Therefore, a microscope typically can provide magnification of up to 1000x. In some applications, an extra tube lens is used after the objective lens to form an intermediate image, and at the same time, keep beams parallel between the objective lens and the tube lens. In this design, some optical components, such as polarizers, dichroic mirrors, and beam splitters, can be added between the objective lens and the tube lens without disturbing the beam focusing.

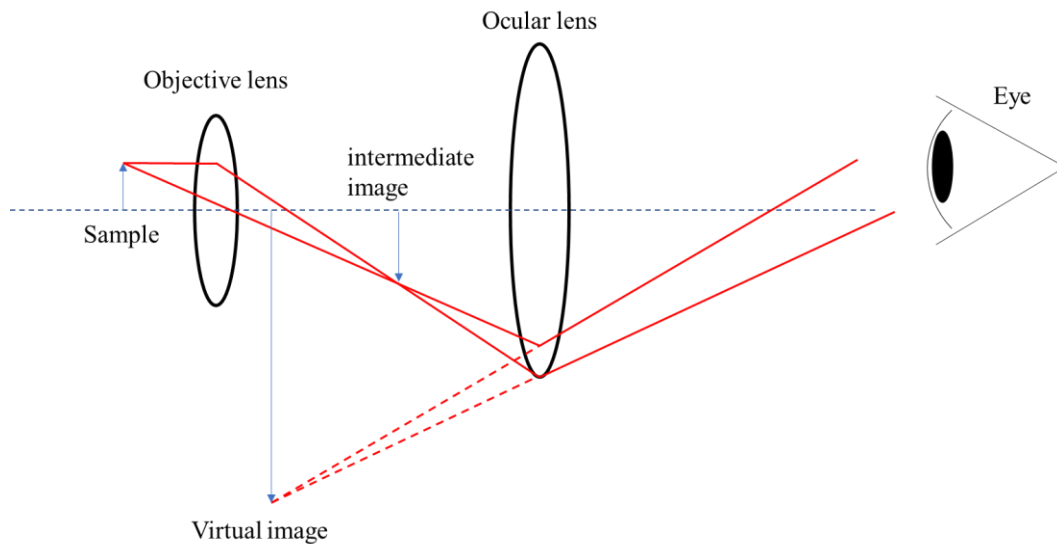


Figure 1-5. Schematic of a simple microscope

The spatial resolution of a microscope is typically governed by the objective lens and the diffraction limitation. According to Rayleigh criterion, two observed points can be perceived as two separate points when the distance between them is larger than the distance between the principal diffraction maximum and the first diffraction minimum. Thus, the spatial resolution d is defined [56]:

$$d = \frac{1.22\lambda}{2NA} \quad (1.4.1)$$

Here, λ is the wavelength and NA is the numerical aperture of the objective lens, which is defined as:

$$NA = n\sin(\theta) \quad (1.4.2)$$

Here, n is the refraction index of the medium, θ is the maximum incidence angle of light that can enter and exit the objective lens. Therefore, a microscope can achieve a better spatial resolution when an objective lens with large NA is used. For instance, a microscope can provide a resolution of 300 nm at a wavelength of 500 nm when the NA of objective lens is 1.

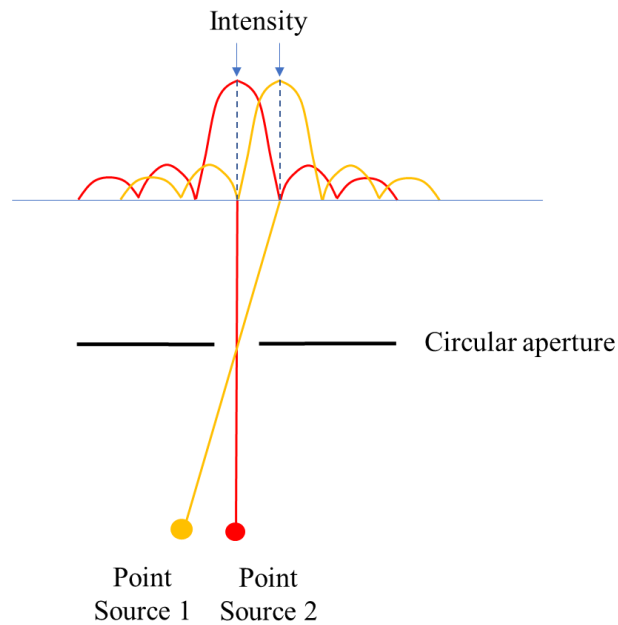


Figure 1-6. Schematic of Rayleigh criterion. The overlapping diffraction pattern produced by two point light sources. According to the Rayleigh criterion, these two observed points can be perceived as two separate points.

The depth of focus indicates the tolerance of the placement of the image plane in the microscope system. Assuming a Gaussian beam, the depth of focus can be determined by the Rayleigh range. Rayleigh range is defined as the distance from the beam waist to a plane where the cross-sectional area of the beam is double of beam waist, as shown in **Figure 1-7**. The depth of focus z_R can be expressed as [58]:

$$z_R = \frac{\pi\omega_0^2}{\lambda} \quad (1.4.3)$$

Here, λ is the wavelength and ω_0 is the beam width. ω_0 can be expressed as [58]:

$$\omega_0 = \frac{\lambda}{\pi\theta} \quad (1.4.4)$$

Thus, the depth of focus become smaller when a better spatial resolution is achieved. For instance, the depth of focus is about 600 nm, when the beam width is 300 nm at a wavelength of 500 nm. Therefore, conventional microscopes require fine adjustments for focusing.

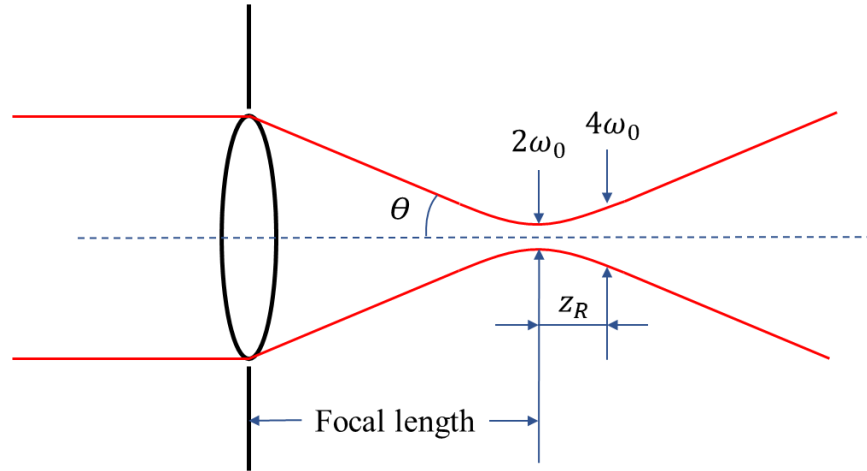


Figure 1-7. Gaussian beam focusing with a convex lens.

Several selections of microscopy techniques are available to observe samples in the optofluidic devices. Among these techniques, bright field microscopy is the simplest one [7]. Typically, a white light source is used to illuminate fluidic samples. Then, morphological features can be observed based on the attenuation of transmitted light. Another technology is dark-field microscopy, which can enhance the contrast, i.e., difference between sample and background [59]. In this method, illumination lights are coupled into the fluidic channel at a carefully selected angle. As a result, transmitted lights that ordinarily passes through the fluidic sample is blocked, while scattered lights and diffracted lights can reach the imager. Therefore, dark-field microscopes provide high-contrast

images. Another technology is fluorescence microscopy, which is suitable to detect characteristic molecules in a biological sample [31]. In this method, the fluid sample is illuminated by excitation light sources. Then, the emission lights are generated by the intrinsic fluorophores or fluorescent labels. Emission filters are used to filter out the excitation lights while transmitting the emission lights. Fluorescent microscopes provide high contrast images that highlight the selected fluorophores in the biological samples.

1.4.2 Lensless Imaging

Lensless imaging has been proven as a promising detection tool in optofluidic devices [48, 49, 60]. Imaging without lens provides a variety of advantages, including portability, low-cost, a large field of view, high throughput, and capability of 3D reconstruction, etc. There are three common lensless imaging approaches: shadow imaging, fluorescence imaging, and holographic imaging.

1.4.2.1 Lensless Shadow Imaging

Shadow imaging is the simplest approach [60], as shown in **figure 1-8**. In this case, a fluid sample is placed on an imager. Like bright field imaging, the sample is illuminated by an incoherent point light source placed above. Then, the sample can be observed based on the attenuation of transmitted light.

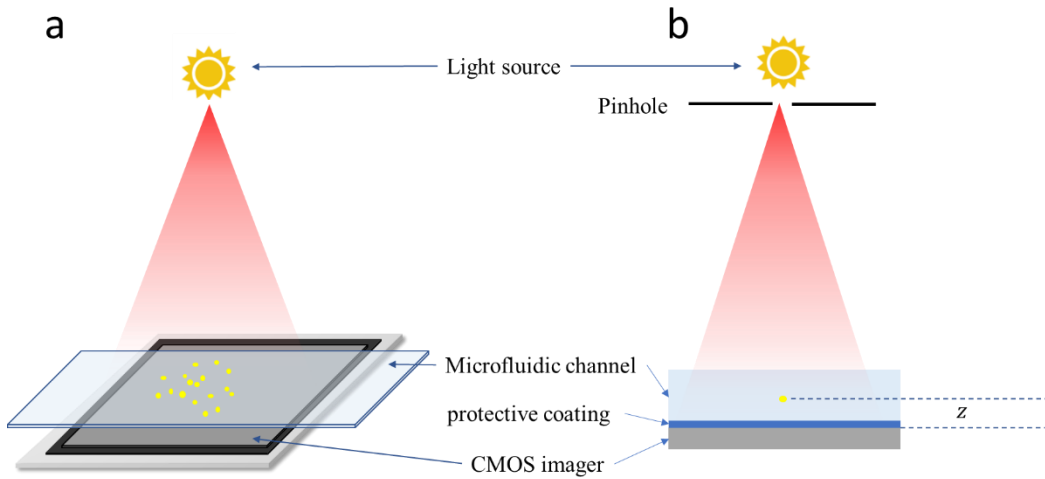


Figure 1-8. Schematic of lensless shadow imaging. (a) A bird's eye view. (b) A side view.

The spatial resolution of shadow imaging is determined by two main factors: (i) z , which is the distance between the sample and the imager and (ii) the pixel size of the imager. When z is large, the shadow projected on the imager is blurred since the lights are diffracted as they pass through the sample. Thus, z should be reduced to improve spatial resolution in a shadow imaging system. Using a thin microfluidic channel helps reduce z . However, a thin microfluidic channel reduces the volumetric throughput and increases the chance of channel clogging. The other factor is pixel size. The pixel size of current CMOS and CCD imagers typically ranges from $1\ \mu\text{m}$ to a few μm . To improve the spatial resolution, several subpixel resolving technologies have been developed. For instance, a resolution of $800\ \text{nm}$ is achieved by placing a mask with apertures between the imager and the sample [61]. Sub-pixel sweeping microscopy (SPSM) achieves a resolution of $660\ \text{nm}$ by moving the illumination source [49].

Shadow imaging has been used to observe and recognize cells in optofluidic devices, such as blood cells [62, 63] and waterborne parasites [49]. Furthermore, Shadow imaging has been developed for microbe tracking and motility analysis [18, 68].

1.4.2.2 Lensless Fluorescence Imaging

In order to avoid the set-up of a bulk fluorescence microscope, fluorescence imaging (**Figure 1-9**) has been adapted to lensless imaging devices [60]. In this case, the fluidic sample is illuminated by an excitation light source, such as a laser and an LED. An emission filter is placed between the sample and the imager to reject excitation light.

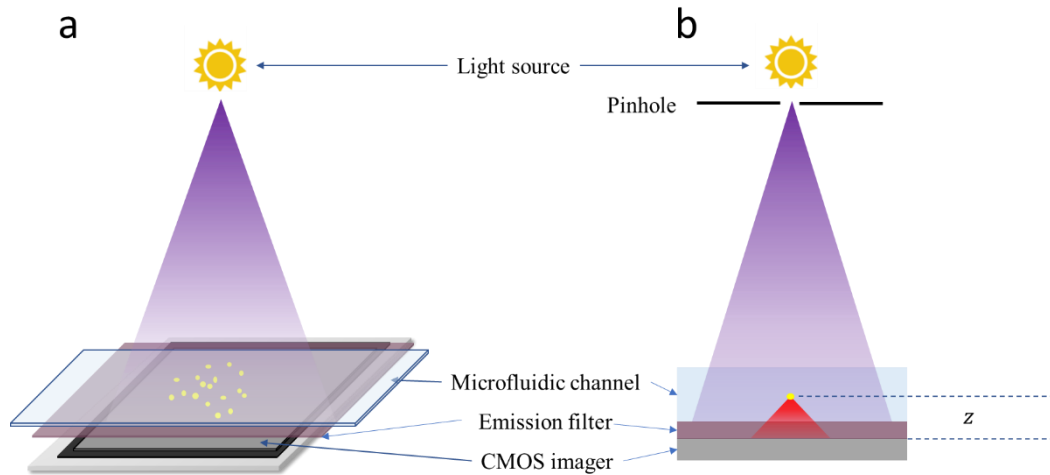


Figure 1-9. Schematic of lensless fluorescence imaging. (a) A bird's eye view. (b) A side view.

The spatial resolution of lensless fluorescence imaging is determined by the point spread function (PSF), which describes the pattern recorded on an imager from a single fluorescent point. When the distance z is larger, the PSF becomes flat and wide, deteriorating the resolution of imaging. Unfortunately, the z in the lensless fluorescence imaging is relatively large due to the placement of the emission filter. Considering a typically z of 200 μm , the resolution is about 200 to 300 μm , which is too large for microbe detection or recognition in many applications [64].

Although the resolution of lensless fluorescence imaging is worse than that of conventional fluorescence microscopy, lensless fluorescence imaging has been used in biological or biomedical applications where miniaturized devices are required. For instance, brain activities of rodents are observed by an implantable

lensless fluorescence device [67]. Cancer cell clusters are detected in vivo by a lensless fluorescence device [68].

1.4.2.3 In-line Holographic Imaging

In-line holography can be adapted to lensless imaging systems, as shown in **Figure 1-10**. The sample is illuminated by a coherent light source, such as a laser. Unlike traditional off-line holography, in-line holography does not require additional optical components to split light into two beams [60]. The object beam is generated by the scattering of cells in the fluidic channel. The reference beam is the transmitted light that ordinarily passes through the fluidic sample without scattering. An interference pattern can be recorded due to the interference of the object beam and the reference beam.

Holographic reconstruction algorithms, such as angular spectrum [69], can be used to recover the cells information from the interference patterns. There are two types of holographic reconstructions. The first one is amplitude reconstruction, which provides spatial-varying amplitude at a plane where the incident light wave interacts with the cell. The second is phase reconstruction, which provides spatial-varying phase delay at the plane. Thus, both transmission and optical thickness of the cell can be estimated after holographic reconstruction.

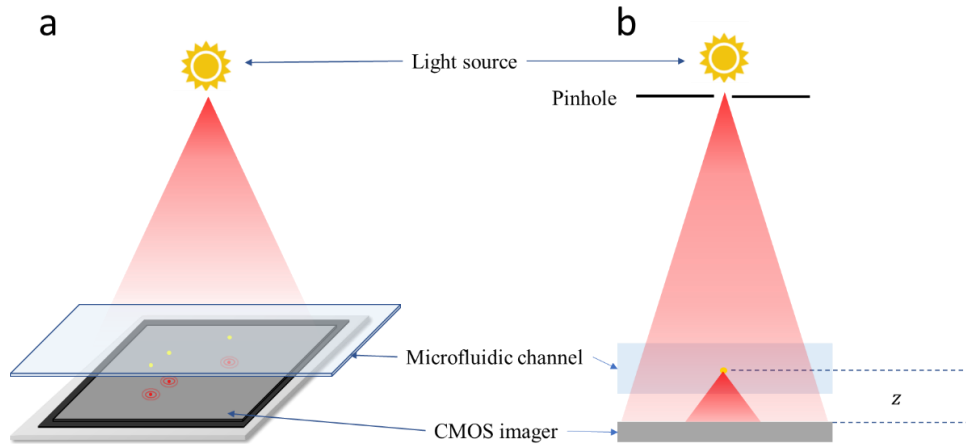


Figure 1-10. Schematic of lensless holographic imaging. (a) A bird's eye view. (b) A side view.

The spatial resolution of a reconstructed image is equal to the resolution of a raw hologram, which is limited by the pixel size of the imager. Like lensless shadow imaging, several subpixel resolving techniques have been used in lensless holographic imaging, such as multiframe pixel super-resolution [70], multilayer pixel super-resolution [71], and incorporating 2D pixel function [72]. Unlike shadow imaging or fluorescence imaging, the holographic imaging does not suffer from the shadow blurring or PSF. Therefore, high-quality holograms can be obtained over a wide range of z , which is typically a few hundred μm .

Holographic imaging has been widely used in cells analysis, such as algae [16], *Staphylococcus aureus* [17], *E. coli* [48], and red blood cells [48]. Furthermore, holographic imaging has been developed for 3D profiling and 3D tracking of cells [73].

1.4.3 Miniaturization of Imaging System

Several miniaturized versions of conventional imaging systems are developed for optofluidic systems. For instance, a miniaturized optofluidic imaging platform with a lateral resolution of $0.8\ \mu\text{m}$ is developed based on a self-interlocking structure of the modular blocks [74]. A fluorescence microscope with a compact size ($2.4\ \text{cm}^3$) and a lateral resolution of $2.5\ \mu\text{m}$ was developed [75]. In order to reduce the complexity of the system, these miniaturized microscopes typically do not use an ocular lens to increase the magnification. However, a costly objective lens with a high NA is still required to achieve a high spatial resolution. Furthermore, miniaturized microscopes typically lack fine adjustments, could create challenges for alignment and focusing for onsite monitoring.

Lensless imaging is particularly well-suited in a miniaturized optofluidic device. Compared with conventional imaging systems, lensless imaging eliminates the need for complex optical elements and focus adjustments, providing opportunities for on-chip integration. Nevertheless, spatial resolution is still a main

limitation of lensless imaging, especially for lensless fluorescence imaging due to a wide PSF. Moreover, lensless fluorescence imaging could suffer from intense background noises in a compact design since the transmitted illumination lights can reach the imager when the emission filter is not efficient [76].

1.5 Roadmap Toward Onsite Monitoring

Figure 1-11 shows a roadmap guiding optofluidic devices towards onsite water quality monitoring. Realization of onsite monitoring has been organized in three stages: development of sensing platforms, onsite deployment, and integration of monitoring systems. The work presented in this research is at the first stage: development of sensing platforms. This stage can be broken down into four tasks.

(i) Identification of analyte

The target analytes could be intrinsic chemical matters and/or microbe properties, such as dissolved oxygen, total nitrogen, pigments, DNA, and morphology features. Alternatively, extrinsic analytes can be induced to improve detection sensitivity and specificity such as fluorescent labels, chemical reagent, and thin films with biomolecular probes. However, additional extrinsic analytes increase the complexity of devices instrumentation and cause reliability and maintenance issues.

(ii) Development of fluid handling module

Fluid handling modules deliver fluidic samples into optofluidic platforms and enable necessary preprocessing procedures, such as fluidic mixing, particle manipulation, and incubating. Many existing optofluidic devices rely on manual sample processing or lab instruments. It is essential to develop fluid handling modules with capability of autonomous operations since an operator is not available to control the device in onsite monitoring applications.

(iii) Development of optics sensing module

A suitable sensing mechanism shall be selected based on the target analyte and required sensing performances. Then light source modules and detection modules shall be developed. Considerations of the light sources and detectors includes intensity, sensitivity, response time, portability, cost, requirements for spatial and spectrum information, etc. Development of optical sensing modules for onsite monitoring could be difficult due to opposing constraints of the aforementioned considerations. For instance, pulse lasers are powerful and have a fast response but are also expensive. Microscopes enable high spatial resolution, but they are typically bulky.

(iv) Data analysis

Algorithms shall be developed to process raw signals or raw images and output final sensing results. In the simple models, curve fitting and thresholding can solve the regression and classification problems, respectively. Machine learning assisted algorithms can be used in complex models and improve the efficiency of data processing and. However, complex algorithms require intensive computing which are difficult to realize in many portable devices.

Once a sensing platform has been built for a target analyte, this sensing platform could be modified for the detection of alternative analytes using a similar sensing mechanism. Then, several analytes could be detected on one platform, sharing same components, such as light sources, detectors, and microcontrollers.

The second stage is the deployment of suitable platforms in the locations where onsite monitoring is required. The demands, such as required sensing performance and devices maintenance cycle, should be identified. Then, the platforms developed at the first stage should be modified, integrated, and tested onsite. The recorded data should be used to tune, optimize, and validate the platform. Finally, performance evaluation can be addressed after enough monitoring duration time.

The third stage is integration of platforms into existing or new created

monitoring systems. Ideal location includes water treatment plants as well as the nodes distributed in the monitoring systems, such as wastewater sewers, buoys, and hydrological stations. There are several issues to be addressed in this stage. These issues include but are not limited to risk regulation, manufacturing, distribution of platforms, networking, and maintenance.

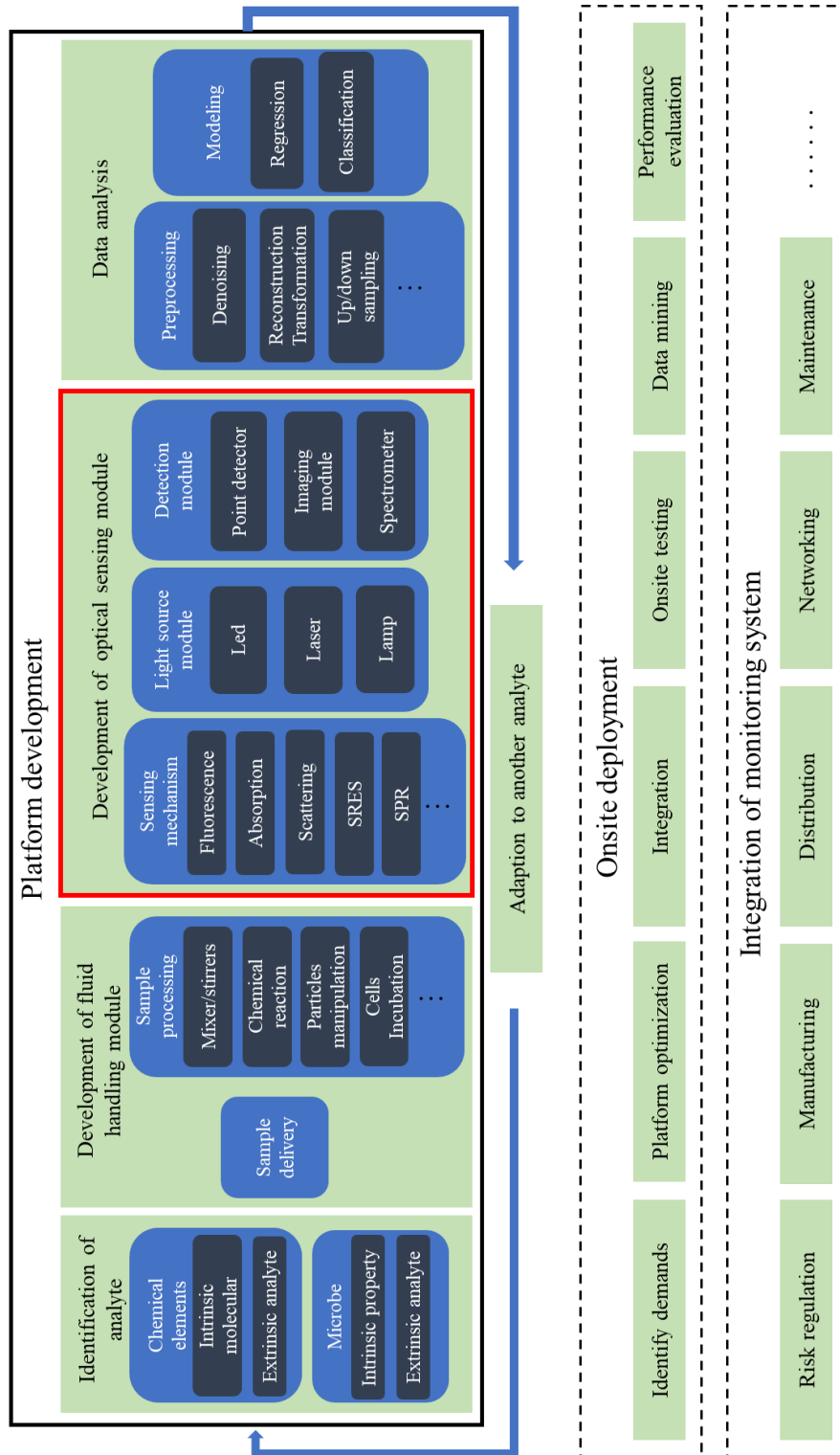


Figure 1-11. A roadmap towards onsite water quality monitoring. There are three stages in the roadmap: (i) Platform development; (ii) Onsite deployment and (iii) Integration of monitoring system.

1.6 Thesis Overview

The goal of this research is to make optofluidic devices compatible with onsite water quality monitoring. We developed two optofluidic platforms for onsite monitoring applications: a fluorescence-based optofluidic platform for chemical sensing and an imaging-based optofluidic platform for microbe detection. Efforts are made in the development of optical sensing module to make optofluidic platform suitable for onsite monitoring. Several novel technologies are developed to overcome the tradeoff between miniaturization and sensing performance. Five milestones were achieved:

First, a fluorescence-based optofluidic platform was developed for chemical sensing. To resist intensity variations that are common occurred in the onsite monitoring, TRF was applied on the fluorescence-based optofluidic platform. Frequency domain method was used to realize TRF with relative miniaturized light sources and detectors.

Second, a 3D ray tracing-based model was built for the optimization of optical path. A method for excitation light coupling was explored to improve the interaction between light and analytes. The efficiency of the optimized platform was demonstrated by DO measurements.

Third, an imaging-based optofluidic platform was developed for microbe detection. To mitigate the bulky microscope setups that are not suitable for onsite monitoring, a dual-modality imaging approach using two portable cameras were developed. By applying this approach, both morphology and fluorescence feature can be observed by a portable imaging device.

Fourth, algorithms were developed to enable cell analysis using the optofluidic platform with dual-modality imaging. The performance of the platform was demonstrated by phytoplankton detection experiments.

Fifth, a Fluorescence Lifetime Imaging (FLIM) approach was developed

under a low-cost CMOS format which can be integrated in a miniaturized optofluidic platform. The potential applications of this FLIM approach in onsite water quality monitoring were explored.

1.7 Thesis Outline

This introduction chapter provides the motivations, overall background, and research roadmap. The thesis outline is summarized as follows.

Chapter 2 presents the development of a fluorescence-based optofluidic platform for chemical sensing. The importance of excitation light coupling and frequency domain TRF are discussed. Both ray tracing simulation and DO experiments are performed. The simulation results indicate that signal-to-noise ratio (SNR) and signal-to-background ratio (SBR) are improved when excitation light is coupled with a prism and an optimized incident angle. The DO measurements results indicate that frequency domain TRF can minimize artifacts causing drift in fluorescence measurements. DO sensing was performed using the fluorescence-based optofluidic platform and demonstrated the efficient of this platform in onsite monitoring. This chapter is based on our paper “A Frequency-Domain Optofluidic Dissolved Oxygen Sensor with Total Internal Reflection Design for in Situ Monitoring” published in IEEE Journal of Selected Topics in Quantum Electronics (27.4, 6900107, 2021).

Chapter 3 presents the development of an imaging-based optofluidic platform for microbe detection. We developed a portable and low-cost imaging approach with two imaging modalities for cell analysis: the lensless imaging mode for morphological features and the fluorescence imaging mode for autofluorescence signal. The particles in the water flow channel can be detected and classified with automated image processing algorithms and machine learning models using integrated morphology and fluorescence features. Photoplankton detection was performed using the imaging-based optofluidic platform and demonstrated the

efficiency of this platform in onsite monitoring. This chapter is based on our manuscript “Dual-modality imaging optofluidic cytometer for in situ detection and analysis of phytoplankton”.

Chapter 4 presents a low-cost FLIM approach based on a portable camera with an electronic rolling shutter. The fluorescence lifetime was obtained by measuring the phase shift of optical fringes captured by the portable camera. The FLIM was validated by mapping the interaction of oxygen and an oxygen-sensitive fluorescent film. This approach can be applied in optofluidic devices that require both spatial resolution and TRF measurements. This chapter is based on our paper “Luminescence lifetime imaging using cellphone camera with electronic rolling shutter” published in *Optics Letters* (45.1, 81-84, 2020).

Chapter 5 summarizes the contribution to the research field, future work, and conclusions of this research.

The research work is presented as three first-author articles from **Chapter 2 - Chapter 4**. My contributions include developing experimental setups, performing the experiments, analyzing the results, and writing the manuscript.

I also developed image/video processing algorithms for a lensless shadow imaging platform. I helped Ms. Jessica Kun to process data acquired by the lensless shadow imaging platform and prepare manuscript. This work has been included in “The Use of Motion Analysis as Particle Biomarkers in Lensless Optofluidic Projection Imaging for Point of Care Urine Analysis” published in *Scientific Reports* (9.1, 1-2, 2019). I assisted Dr. Eric Mahoney with development of a 3D ray tracing model. This work has been included in “Optical model of light propagation in total internal reflection fluorescence sensors” published in *Applied Optics* (59.34, 10651-60, 2020).

References

- [1] Minzioni P, Osellame R, Sada C, Zhao S, Omenetto FG, Gylfason KB, Haraldsson T, Zhang Y, Ozcan A, Wax A, Mugele F. Roadmap for optofluidics. *Journal of Optics*. 2017 Aug 22;19(9):093003.
- [2] Song, Chaolong, Nam-Trung Nguyen, and Say Hwa Tan. "Toward the commercialization of optofluidics." *Microfluidics and Nanofluidics* 21.8 (2017): 139.
- [3] Fan X, White IM. Optofluidic microsystems for chemical and biological analysis. *Nature photonics*. 2011 Oct;5(10):591.
- [4] Zhang J, Yan S, Yuan D, Alici G, Nguyen NT, Warkiani ME, Li W. Fundamentals and applications of inertial microfluidics: a review. *Lab on a Chip*. 2016;16(1):10-34.
- [5] Kuswandi B, Huskens J, Verboom W. Optical sensing systems for microfluidic devices: a review. *Analytica chimica acta*. 2007 Oct 10;601(2):141-55.
- [6] Yun H, Kim K, Lee WG. Cell manipulation in microfluidics. *Biofabrication*. 2013 Feb 13;5(2):022001.
- [7] Wu J, Zheng G, Lee LM. Optical imaging techniques in microfluidics and their applications. *Lab on a Chip*. 2012;12(19):3566-75.
- [8] Bourgeois W, Burgess JE, Stuetz RM. On-line monitoring of wastewater quality: a review. *Journal of Chemical Technology & Biotechnology: International Research in Process, Environmental & Clean Technology*. 2001 Apr;76(4):337-48.
- [9] Strobl RO, Robillard PD. Network design for water quality monitoring of surface freshwaters: A review. *Journal of environmental management*. 2008 Jun 1;87(4):639-48.
- [10] Jaywant SA, Arif KM. A Comprehensive Review of Microfluidic Water Quality Monitoring Sensors. *Sensors*. 2019 Jan;19(21):4781.
- [11] Wang N, Dai T, Lei L. Optofluidic technology for water quality monitoring. *Micromachines*. 2018 Apr;9(4):158.

- [12] Chen YF, Jiang L, Mancuso M, Jain A, Oncescu V, Erickson D. Optofluidic opportunities in global health, food, water and energy. *Nanoscale*. 2012;4(16):4839-57.
- [13] Xiong B, Mahoney E, Lo JF, Fang Q. A Frequency-domain optofluidic dissolved oxygen sensor with total internal reflection design for in situ monitoring. *IEEE Journal of Selected Topics in Quantum Electronics*. 2020 May 28.
- [14] Waich K, Mayr T, Klimant I. Fluorescence sensors for trace monitoring of dissolved ammonia. *Talanta*. 2008 Oct 19;77(1):66-72.
- [15] Elmas S, Pospisilova A, Sekulska AA, Vasilev V, Nann T, Thornton S, Priest C. Photometric Sensing of Active Chlorine, Total Chlorine, and pH on a Microfluidic Chip for Online Swimming Pool Monitoring. *Sensors*. 2020 Jan;20(11):3099.
- [16] Göröcs Z, Tamamitsu M, Bianco V, Wolf P, Roy S, Shindo K, Yanny K, Wu Y, Koydemir HC, Rivenson Y, Ozcan A. A deep learning-enabled portable imaging flow cytometer for cost-effective, high-throughput, and label-free analysis of natural water samples. *Light: Science & Applications*. 2018 Sep 19;7(1):1-2.
- [17] Veli M, Ozcan A. Computational sensing of *Staphylococcus aureus* on contact lenses using 3D imaging of curved surfaces and machine learning. *ACS nano*. 2018 Mar 9;12(3):2554-9.
- [18] Kun J, Smieja M, Xiong B, Soleymani L, Fang Q. The Use of Motion Analysis as Particle Biomarkers in Lensless Optofluidic Projection Imaging for Point of Care Urine Analysis. *Scientific reports*. 2019 Nov 21;9(1):1-2.
- [19] Măriuța D, Colin S, Barrot-Lattes C, Le Calvé S, Korvink JG, Baldas L, Brandner JJ. Miniaturization of fluorescence sensing in optofluidic devices. *Microfluidics and Nanofluidics*. 2020 Sep;24(9):1-28.
- [20] Wang M, Jing N, Chou IH, Cote GL, Kameoka J. An optofluidic device for surface enhanced Raman spectroscopy. *Lab on a Chip*. 2007;7(5):630-2.

- [21] Guo T, Wei Y, Xu C, Watts BR, Zhang Z, Fang Q, Zhang H, Selvaganapathy PR, Deen MJ. Counting of *Escherichia coli* by a microflow cytometer based on a photonic–microfluidic integrated device. *Electrophoresis*. 2015 Jan;36(2):298-304.
- [22] Mohammed MI, Haswell S, Gibson I. Lab-on-a-chip or Chip-in-a-lab: Challenges of Commercialization Lost in Translation. *Procedia Technology*. 2015 Jan 1;20:54-9.
- [23] Zhang Y, Watts BR, Guo T, Zhang Z, Xu C, Fang Q. Optofluidic device based microflow cytometers for particle/cell detection: a review. *Micromachines*. 2016 Apr;7(4):70.
- [24] Gao Y, Xin Z, Zeng B, Gan Q, Cheng X, Bartoli FJ. Plasmonic interferometric sensor arrays for high-performance label-free biomolecular detection. *Lab on a Chip*. 2013;13(24):4755-64.
- [25] Capitan-Vallvey LF, Palma AJ. Recent developments in handheld and portable optosensing—A review. *Analytica chimica acta*. 2011 Jun 24;696(1-2):27-46.
- [26] Wei L, Yan W, Ho D. Recent advances in fluorescence lifetime analytical microsystems: Contact optics and CMOS time-resolved electronics. *Sensors*. 2017 Dec;17(12):2800.
- [27] Amendola V, Pilot R, Frasconi M, Maragò OM, Iatì MA. Surface plasmon resonance in gold nanoparticles: a review. *Journal of Physics: Condensed Matter*. 2017 Apr 20;29(20):203002.
- [28] Faulkner S, Pope SJ, Burton-Pye BP. Lanthanide complexes for luminescence imaging applications. *Applied Spectroscopy Reviews*. 2005 Jan 1;40(1):1-31.
- [29] Zheng P, Wu N. Fluorescence and sensing applications of graphene oxide and graphene quantum dots: a review. *Chemistry—An Asian Journal*. 2017 Sep 19;12(18):2343-53.
- [30] Huang NT, Zhang HL, Chung MT, Seo JH, Kurabayashi K. Recent advancements in optofluidics-based single-cell analysis: optical on-chip cellular manipulation, treatment, and property detection. *Lab on a Chip*. 2014;14(7):1230-45.

- [31] Zhang YS, Ribas J, Nadhman A, Aleman J, Selimović Š, Leshner-Perez SC, Wang T, Manoharan V, Shin SR, Damilano A, Annabi N. A cost-effective fluorescence mini-microscope for biomedical applications. *Lab on a Chip*. 2015;15(18):3661-9.
- [32] Benincà E, Huisman J, Heerkloss R, Jöhnk KD, Branco P, Van Nes EH, Scheffer M, Ellner SP. Chaos in a long-term experiment with a plankton community. *Nature*. 2008 Feb;451(7180):822-5.
- [33] Gilbride KA, Lee DY, Beaudette LA. Molecular techniques in wastewater: understanding microbial communities, detecting pathogens, and real-time process control. *Journal of microbiological methods*. 2006 Jul 1;66(1):1-20.
- [34] Guidelines for Canadian Drinking Water Quality - Summary Table. <https://www.canada.ca/en/health-canada/services/environmental-workplace-health/reports-publications/water-quality/guidelines-canadian-drinking-water-quality-summary-table.html>. Visited in 2021 Jan.
- [35] Chen W, Fang X, Li H, Cao H, Kong J. A simple paper-based colorimetric device for rapid mercury (II) assay. *Scientific reports*. 2016 Aug 24;6(1):1-7.
- [36] Jayawardane BM, Wei S, McKelvie ID, Kolev SD. Microfluidic paper-based analytical device for the determination of nitrite and nitrate. *Analytical chemistry*. 2014 Aug 5;86(15):7274-9.
- [37] Cho YB, Jeong SH, Chun H, Kim YS. Selective colorimetric detection of dissolved ammonia in water via modified Berthelot's reaction on porous paper. *Sensors and Actuators B: Chemical*. 2018 Mar 1;256:167-75.
- [38] Nath P, Arun RK, Chanda N. A paper based microfluidic device for the detection of arsenic using a gold nanosensor. *Rsc Advances*. 2014;4(103):59558-61.
- [39] Li Z, Askim JR, Suslick KS. The optoelectronic nose: colorimetric and fluorometric sensor arrays. *Chemical reviews*. 2018 Sep 12;119(1):231-92.
- [40] Qi J, Li B, Wang X, Zhang Z, Wang Z, Han J, Chen L. Three-dimensional paper-based microfluidic chip device for multiplexed fluorescence detection of

Cu²⁺ and Hg²⁺ ions based on ion imprinting technology. *Sensors and Actuators B: Chemical*. 2017 Nov 1;251:224-33.

[41] Herranz S, Bocková M, Marazuela MD, Homola J, Moreno-Bondi MC. An SPR biosensor for the detection of microcystins in drinking water. *Analytical and bioanalytical chemistry*. 2010 Nov 1;398(6):2625-34.

[42] Farré M, Martínez E, Ramón J, Navarro A, Radjenovic J, Mauriz E, Lechuga L, Marco MP, Barceló D. Part per trillion determination of atrazine in natural water samples by a surface plasmon resonance immunosensor. *Analytical and bioanalytical chemistry*. 2007 May 1;388(1):207-14.

[43] Qi N, Li B, You H, Zhang W, Fu L, Wang Y, Chen L. Surface-enhanced Raman scattering on a zigzag microfluidic chip: towards high-sensitivity detection of As (III) ions. *Analytical Methods*. 2014;6(12):4077-82.

[44] Lee S, Choi J, Chen L, Park B, Kyong JB, Seong GH, Choo J, Lee Y, Shin KH, Lee EK, Joo SW. Fast and sensitive trace analysis of malachite green using a surface-enhanced Raman microfluidic sensor. *Analytica chimica acta*. 2007 May 8;590(2):139-44.

[45] Hashemi N, Erickson JS, Golden JP, Ligler FS. Optofluidic characterization of marine algae using a microflow cytometer. *Biomicrofluidics*. 2011 Sep 20;5(3):032009.

[46] McClain MA, Culbertson CT, Jacobson SC, Ramsey JM. Flow cytometry of *Escherichia coli* on microfluidic devices. *Analytical chemistry*. 2001 Nov 1;73(21):5334-8.

[47] Yang SY, Lien KY, Huang KJ, Lei HY, Lee GB. Micro flow cytometry utilizing a magnetic bead-based immunoassay for rapid virus detection. *Biosensors and Bioelectronics*. 2008 Dec 1;24(4):855-62.

[48] Seo S, Su TW, Tseng DK, Erlinger A, Ozcan A. Lensfree holographic imaging for on-chip cytometry and diagnostics. *Lab on a Chip*. 2009;9(6):777-87.

- [49] Lee SA, Erath J, Zheng G, Ou X, Willems P, Eichinger D, Rodriguez A, Yang C. Imaging and identification of waterborne parasites using a chip-scale microscope. *PloS one*. 2014 Feb 26;9(2):e89712.
- [50] Golberg A, Linshiz G, Kravets I, Stawski N, Hillson NJ, Yarmush ML, Marks RS, Konry T. Cloud-enabled microscopy and droplet microfluidic platform for specific detection of *Escherichia coli* in water. *PloS one*. 2014 Jan 27;9(1):e86341.
- [51] Ozcelik D, Cai H, Leake KD, Hawkins AR, Schmidt H. Optofluidic bioanalysis: fundamentals and applications. *Nanophotonics*. 2017 Mar 16;6(4):647-61.
- [52] Yao L, Zheng L, Cai G, Wang S, Wang L, Lin J. A Rapid and Sensitive Salmonella Biosensor Based on Viscoelastic Inertial Microfluidics. *Sensors*. 2020 Jan;20(9):2738.
- [53] Quaranta M, Borisov SM, Klimant I. Indicators for optical oxygen sensors. *Bioanalytical reviews*. 2012 Dec 1;4(2-4):115-57.
- [54] Waich K, Mayr T, Klimant I. Fluorescence sensors for trace monitoring of dissolved ammonia. *Talanta*. 2008 Oct 19;77(1):66-72.
- [55] Gayathri P, Moon D, Anthony SP. Rewritable fluorescent platform and reusable hydrazine sensing thin film using aldehyde functionalized fluorophore integrated PMMA polymer matrix. *Materials Chemistry and Physics*. 2019 Sep 1;235:121753.
- [56] Lakowicz JR, editor. Principles of fluorescence spectroscopy. Springer science & business media; 2013 Apr 17.
- [57] Boens N, Qin W, Basarić N, Hofkens J, Ameloot M, Pouget J, Lefevre JP, Valeur B, Gratton E, VandeVen M, Silva ND. Fluorescence lifetime standards for time and frequency domain fluorescence spectroscopy. *Analytical chemistry*. 2007 Mar 1;79(5):2137-49.
- [58] Alda J. Laser and Gaussian beam propagation and transformation. *Encyclopedia of optical engineering*. 2003 Jan;2013:999-1013.

- [59] Haiden C, Wopelka T, Jech M, Keplinger F, Vellekoop MJ. A microfluidic chip and dark-field imaging system for size measurement of metal wear particles in oil. *IEEE Sensors Journal*. 2015 Nov 17;16(5):1182-9.
- [60] Ozcan A, McLeod E. Lensless imaging and sensing. *Annual review of biomedical engineering*. 2016 Jul 11;18:77-102.
- [61] Cui X, Lee LM, Heng X, Zhong W, Sternberg PW, Psaltis D, Yang C. Lensless high-resolution on-chip optofluidic microscopes for *Caenorhabditis elegans* and cell imaging. *Proceedings of the National Academy of Sciences*. 2008 Aug 5;105(31):10670-5.
- [62] Liu X, Huang X, Jiang Y, Xu H, Guo J, Hou HW, Yan M, Yu H. A microfluidic cytometer for complete blood count with a 3.2-megapixel, 1.1- μm -pitch super-resolution image sensor in 65-nm BSI CMOS. *IEEE Transactions on Biomedical Circuits and Systems*. 2017 Jul 18;11(4):794-803.
- [63] Huang X, Guo J, Wang X, Yan M, Kang Y, Yu H. A contact-imaging based microfluidic cytometer with machine-learning for single-frame super-resolution processing. *PloS one*. 2014 Aug 11;9(8):e104539.
- [64] Coskun AF, Su TW, Ozcan A. Wide field-of-view lens-free fluorescent imaging on a chip. *Lab on a Chip*. 2010;10(7):824-7.
- [67] Ohta J, Ohta Y, Takehara H, Noda T, Sasagawa K, Tokuda T, Haruta M, Kobayashi T, Akay YM, Akay M. Implantable microimaging device for observing brain activities of rodents. *Proceedings of the IEEE*. 2016 Jul 28;105(1):158-66.
- [68] Papageorgiou EP, Zhang H, Giverts S, Park C, Boser BE, Anwar M. Real-time cancer detection with an integrated lensless fluorescence contact imager. *Biomedical Optics Express*. 2018 Aug 1;9(8):3607-23.
- [69] Latychevskaia T, Fink HW. Practical algorithms for simulation and reconstruction of digital in-line holograms. *Applied optics*. 2015 Mar 20;54(9):2424-34.

- [70] Zheng G, Lee SA, Antebi Y, Elowitz MB, Yang C. The ePetri dish, an on-chip cell imaging platform based on subpixel perspective sweeping microscopy (SPSM). *Proceedings of the National Academy of Sciences*. 2011 Oct 11;108(41):16889-94.
- [71] Wang M, Feng S, Wu J. Multilayer pixel super-resolution lensless in-line holographic microscope with random sample movement. *Scientific Reports*. 2017 Oct 6;7(1):1-8.
- [72] Greenbaum A, Luo W, Khademhosseini B, Su TW, Coskun AF, Ozcan A. Increased space-bandwidth product in pixel super-resolved lensfree on-chip microscopy. *Scientific reports*. 2013 Apr 24;3(1):1-8.
- [73] Yu X, Hong J, Liu C, Kim MK. Review of digital holographic microscopy for three-dimensional profiling and tracking. *Optical engineering*. 2014 Apr;53(11):112306.
- [74] Lee Y, Kim B, Oh I, Choi S. Optofluidic Modular Blocks for On-Demand and Open-Source Prototyping of Microfluidic Systems. *Small*. 2018 Dec;14(52):1802769.
- [75] Ghosh KK, Burns LD, Cocker ED, Nimmerjahn A, Ziv Y, El Gamal A, Schnitzer MJ. Miniaturized integration of a fluorescence microscope. *Nature methods*. 2011 Oct;8(10):871.
- [76] Coskun AF, Sencan I, Su TW, Ozcan A. Lensfree fluorescent on-chip imaging of transgenic *Caenorhabditis elegans* over an ultra-wide field-of-view. *PloS one*. 2011 Jan 6;6(1):e15955.

Chapter 2.

Paper I - A Frequency-Domain Optofluidic Dissolved Oxygen Sensor with Total Internal Reflection Design for in Situ Monitoring

Bo Xiong¹, Eric Mahoney¹, Joe F. Lo³, and Qiyin Fang^{1,2,*}

School of Biomedical Engineering, McMaster University, Hamilton L8S 4L8, Canada

Department of Engineering Physics, McMaster University, Hamilton L8S 4L8, Canada

Department of Mechanical Engineering, University of Michigan Dearborn, Dearborn 48128, US

Published in IEEE Journal of Selected Topics in Quantum Electronics; 27(4):
6900107, 2021

Printed with permission

doi: 10.1109/JSTQE.2020.2997810

Introduction to Paper I:

Sensing of chemical elements, such as dissolved oxygen, heavy metal ions, and organic toxins, is necessary for water quality monitoring. This chapter describes the development of a fluorescence-based optofluidic sensing platform for the onsite monitoring of chemical elements. DO measurements were demonstrated on this platform by using a thin Ru complex functionalized film. To make fluorescence-based optofluidic devices compatible for onsite monitoring, several technologies were developed to enhance fluorescence sensing and improve long-term stability.

In this work, frequency domain TRF was implemented to minimize artifacts causing long-term drift in fluorescence measurements, while reducing dependence on costly detectors and light sources. Moreover, an excitation beam was coupled into the sensing chip with a prism, and TIR took place on the surface between fluorophore functionalized film and water. This coupling design enhanced fluorescence signal in the integrated device and minimized background autofluorescence emitted by fluidic sample. DO measurement results show a resolution of 0.2ppm, and a drift less than ± 0.4 ppm in an accelerated photobleaching test. In short, this work shows the effectiveness of the frequency-domain optofluidic platform with TIR design and prism assisted coupling as a solution for onsite monitoring.

The original optofluidic platform presented in this work was developed by Dr. Eric Mahoney. To realized frequency domain TRF measurements, I improved optical design and developed software using MATLAB. I performed the DO measurements and optimized the platform with prism-assisted coupling. I took a lead role in manuscript writing and addressing reviewers' questions.

Contents of Paper I

Abstract

Continuous measurements of dissolved oxygen (DO) variation are important in water monitoring and biomedical applications, which require low-cost and low-maintenance sensors capable of automated operation. A frequency-domain optofluidic DO sensor with total internal reflection (TIR) design has been developed based on fluorescence quenching of Ruthenium complex ($\text{Ru}(\text{dpp})_3\text{Cl}_2$). To minimize artifacts causing drift in fluorescence measurements such as background autofluorescence, photobleaching, optical alignment variation, a low-cost frequency-domain approach is implemented in an optofluidic platform to measure the phase shift between the excitation and emission light. We show that the frequency domain optofluidic DO sensor provides absolute DO concentrations in repeated measurements. TIR design can enhance fluorescence signal in the integrated device and minimize background autofluorescence in the sample, which can subsequently improve overall sensitivity. Furthermore, photobleaching in the samples would be mitigated as the incident light does not enter the microfluidic channel. Our results demonstrate a measurement resolution of 0.2 ppm and response times of less than one minute. In accelerated photobleaching conditions, the long-term drift is shown to be less than ± 0.4 ppm. These results suggest the potential of this optofluidic DO sensor as an in situ platform for water monitoring and biomedical applications.

2.1 Introduction

Dissolved oxygen (DO) concentration is an important indicator for water quality. In a stable body of fresh water, the concentration of DO ranges from 8 ppm to 14 ppm and varies in different conditions including temperature [1]. Marine creatures require a DO concentration of at least 5 ppm to survive [1], while anaerobic condition (<1 ppm) promotes the release of pollution from sediments into overlying water [2]. DO monitoring can be used for early warning of algae blooming [3], drink water quality [4], and other contamination events. DO concentration is also monitored and controlled in wastewater treatments [5-6]. By monitoring DO concentration decreasing rate, organic pollution in water can be evaluated using BOD (Biochemical Oxygen Demand) tests [7-8], which are used to forecast the incoming load for wastewater treatment plants to optimize treatment strategy [9-10]. At present, DO is usually manually measured on site (e.g. in river, lake, or water treatment bioreactors) while BOD tests are generally performed in a lab. Automatic and continuous monitoring of DO/BOD values in the waterbody is highly desired.

Monitoring the oxygenation of cells and tissues is also of interest in metabolic imaging applications. The metabolic status and rate of oxygen consumption can be used to assess functional and dysfunctional cells, and to determine cellular responses to treatment for disease or cancers [11-12]. Measurement of embryonic oxygen consumption may also indicate the quality of embryos for applications in In-Vitro Fertilization [13]. Metabolic status of cells has been determined by monitoring the oxygen reduction ratio of electron acceptors in cells using Fluorescence Lifetime Imaging (FLIM) [14-15]. Oxygenation of cells and tissues has been accomplished by measuring the collisional quenching of oxygen sensitive phosphorescent dyes using Phosphorescent Lifetime Imaging (PLIM) which is complementary to FLIM [16].

There are two main requirements for DO monitoring sensors in such applications: (i) automated, continuous and repeated measurement must be

performed without manual intervention; and (ii) low maintenance, calibration free, low power consumption, and free of chemical reagent.

Chemical, electrochemical and optical methods have been used in the DO sensing. In the chemical DO sensing, titration that produces color change has been the standard for accuracy and precision when measuring dissolved oxygen [17]. However, titrimetric procedures consume chemical reagents and require manual lab works. Electrochemical DO sensors typically use Clark electrode which relies on the electrocatalytic reaction of oxygen on platinum [18-19]. Nevertheless, several common drawbacks of the electrochemical sensors limit their usage in the in situ water monitoring, including interferences from other ions, requirements of water flow, frequent calibrations and a limited lifetime caused by electrode aging. In contrast, optical DO sensors are based on collisional quenching between oxygen and fluorophores/phosphors in a polymer matrix [20-24]. Optical DO sensors present advantages of no consumable reagent, less interferences from other ions, a long working lifetime, and a reversible, continuous mode of operation.

In the optical DO methods, both fluorescence intensity [20] and lifetime [21] can be used to quantify DO according to Stern-Volmer equation [24]:

$$\frac{I_f^0}{I_f} = \frac{\tau_0}{\tau} = 1 + k_q \tau_0 [Q] \quad (2.1)$$

where k_q is the quenching constant; $[Q]$ is the concentration of dissolved oxygen; I_f and τ are fluorescence intensity and fluorescence lifetime without dissolved oxygen; I_f^0 and τ_0 are fluorescence intensity and fluorescence lifetime in the presence of dissolved oxygen, respectively. Time-resolved fluorescence (trF) based approaches are attractive in automated measurements since intensity variations caused by photobleaching, dye leaching, detector drift, laser output fluctuation, change in optical path, etc., have less effects on the fluorescence lifetime [21-22, 25-26]. However, current optical DO sensors used in

environmental applications are still expensive, large and have high power consumption compared with electrochemical DO sensors.

Frequency-domain method is another way to achieve time-resolved fluorescence measurements with low-cost light sources and detection systems [23-24, 27]. With a sinusoidal excitation light, the fluorescence signal is also modulated but phase shifted relative to the excitation light. Assuming the fluorescence is a single-exponential decay, its lifetime can be estimated from the phase shift between excitation and emission signals at the modulation frequency, as shown in Eq. (2.2):

$$\phi(f) = \tan^{-1}(2\pi f\tau) \quad (2.2)$$

Where f is the modulation frequency; $\phi(f)$ is the relative phase shift; and τ is the fluorescence lifetime.

Recent advances in miniaturized optical and electronic components including lenses, light sources, photo detectors and data acquisition devices enable the instrumentation of portable optical sensors with microfluidic devices. The frequency-domain fluorescence lifetime measurements can be achieved by a low-cost approach which uses a camera with a rolling shutter [28]. Nanotechnologies, such as, core-shell nanoparticles [29] can be used to enhance the change of fluorescence intensity/lifetime in response oxygen concentration. Therefore, a frequency-domain optofluidic device could be a promising approach for DO monitoring in the in situ applications.

In this paper, we report the development of an optofluidic DO sensor for continuous, repeated in situ DO monitoring. A frequency-domain fluorescence detection method is applied to measure oxygen concentration without the need for calibrations in every measurement and suppress long-term drift. The fluorescence signal is enhanced by a total internal reflection (TIR) design, which minimizes background autofluorescence in the water sample. Photobleaching to the samples could be mitigated as the incident light does not enter the microfluid channel. Such an optofluidic platform would allow automated preprocessing of the sample

and enables potential BOD measurements and biomedical applications.

2.2 Materials and Methods

2.2.1 Reagents

Polydimethylsiloxane (PDMS) Sylgard 184 was purchased from Dow Corning (Midland, MI). RuTris (4,7-diphenyl-1,10-phenanthroline) ruthenium (II) dichloride ($\text{Ru}(\text{dpp})_3\text{Cl}_2$) was purchased from Alfa Aesar (Haverhill, MA). Anhydrous alcohol was purchased from Commercial Alcohols Inc. (Brampton, CA).

2.2.2 Sensor Design

As shown in Fig. 2-1(a), the fluidic module of the DO sensor consists four layers: (i) a microfluidic chamber with a cap, (ii) a DO sensitive layer, (iii) a glass slide as substrate, and (iv) a prism. Water flow is confined in the PDMS cap and the total volume of the water channel is about 192 μl ($L \times W \times H$: 16 \times 8 \times 1.5 mm). The DO sensitive layer consists of PDMS and $\text{Ru}(\text{dpp})_3\text{Cl}_2$. An excitation beam is coupled into the DO sensitive layer with an incident angle θ , as shown in Fig. 2-1(a). The wedged angle of the prism is the same as the incident angle θ to make sure the excitation beam is perpendicular to the entry surface of the prism.

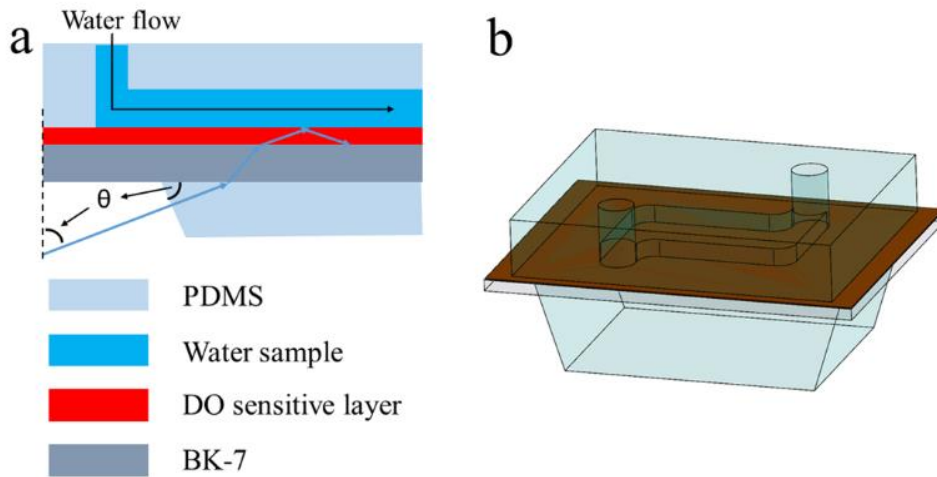


Figure 2-1. Schematic of fluidic module. (a) Side and (b) 3D schematic view of the DO sensor

2.2.3 Chip Fabrication

$\text{Ru}(\text{dpp})_3\text{Cl}_2$ is dissolved in anhydrous alcohol (1:10 w/w) and then mixed in PDMS which is mixed with a 10:1 ratio of base: curing agent. The weight ratio of $\text{Ru}(\text{dpp})_3\text{Cl}_2$ to PDMS is 1:200. Next, the complex was coated on the microscope slide by spin coating at 3000 rpm for 60 s. This process produced a DO sensitive layer of 15 μm in thickness. Finally, the DO sensitive layer is cured by heating at 90°C for 12 hours.

2.2.4 Simulation and Optimization

The incident angle θ (defined in Fig. 2-1) is optimized by ray tracing simulation in Zemax™. Two design configurations of sensors are used in the simulation: (a) the proposed design with a prism and (b) a design without a prism, as shown in Fig. 2-2(a) and Fig. 2-2(b). Parallel excitation beams with different incident angles were induced and the fluorescence intensities generated by the DO sensitive layer were calculated using the ray tracing model.

As shown in Fig. 2-2(c), the fluorescence intensity increases by 7 times at

80 degree in the proposed design. When θ is larger than 70 degrees, total internal reflection of the excitation beam takes place at the surface between the DO sensitive layer and the sample. As a result, the optical path of the excitation light within the DO sensitive layer increases, leading to an increased absorption of excitation light. Conversely, in the design without the prism (Fig. 2-2(b)), when the incident angle is larger than 60 degrees, the high reflection rate of the excitation beam at the air/glass interface and the glass/PDMS interface results in the reduction of fluorescence intensity.

Ray tracing simulation is performed to demonstrate that the autofluorescence generated in the water sample can be reduced using the proposed design with a prism. Assuming that fluorophores are present in the water sample, excitation beams with different incident angles θ were induced and fluorescence intensities generated by the water sample were calculated. When θ is larger than 70 degrees, TIR limits the excitation of bulk water. As a result, the fluorescence from water channel is reduced as shown in the blue curve in the Fig. 2-2(d).

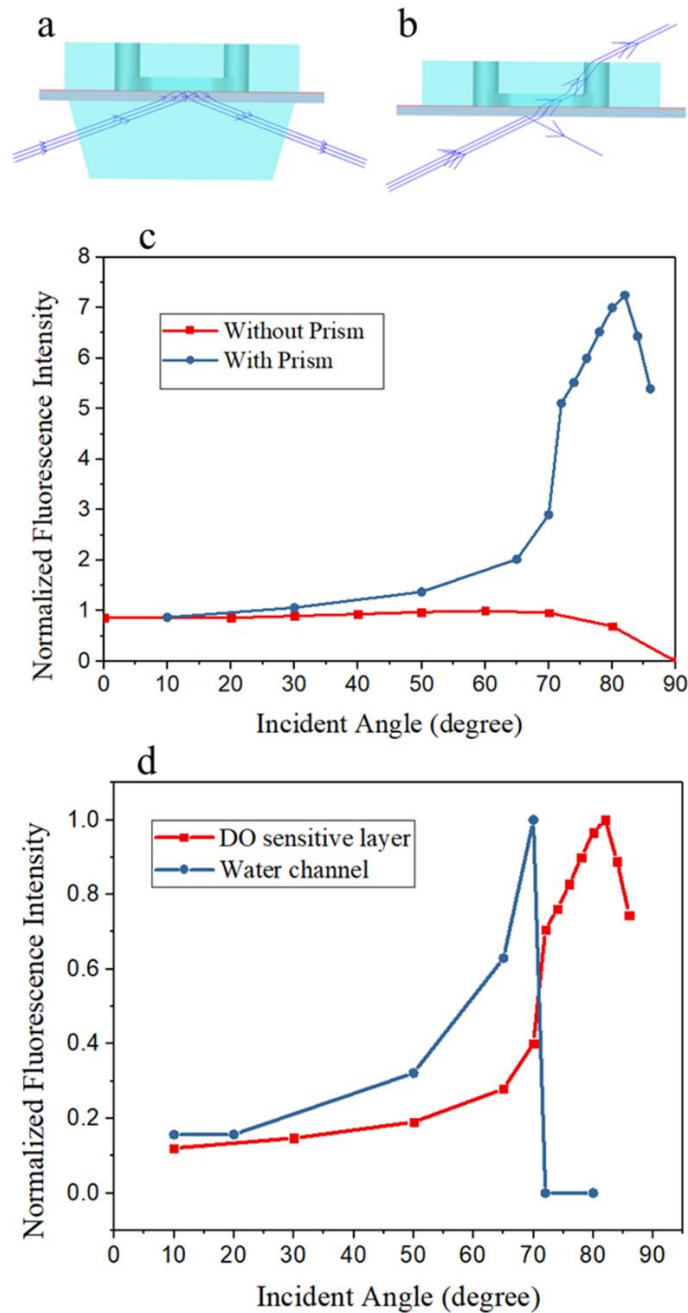


Figure 2-2. Ray tracing models and simulation results. (a) A proposed design with prism coupling and (b) a control design without prism coupling. (c) Normalized fluorescence intensity based on the ray tracing simulation of the two designs. The fluorescence intensity is normalized by the maximum intensity in the control group (i.e. the 60 degree point). (d) Normalized fluorescence intensity generated in the DO sensitive layer and fluidic channel in the TIR design. Refraction indexes used in the simulation are water:1.33, air:1.01, PDMS:1.416 and glass slide: 1.51.

Therefore, the θ is chosen to be 80 degree in the DO sensor to enhance the fluorescence and mitigate the unintended autofluorescence in the water sample. These simulation results indicate that fluorescence generated by DO sensitive layer can be enhanced by using the TIR design. At the same time, the background autofluorescence from the water sample can be reduced.

2.3 Experimental Setup

Following the design optimization in the simulation, a customized frequency domain DO setup was built (Fig. 2-3). A 450 nm laser (450, Wuhan Besram Technology Inc, Wuhan, China) is modulated by a square signal with a frequency of 160 kHz and the output power after the pin hole is 15.5 mW. The excitation beam is coupled into the DO sensor with an incident angle of 80 degrees. The emitted fluorescent light is coupled into a photoelectric detector (APD 120A, Thorlabs, Newton, NJ) with a relay assemble consists of two aspherical lenses (EFL = 20 mm, ACL2520U-A, Thorlabs). An emission filter (BrightLine® FF01-609/181-25, Semrock, Rochester, NY) with a center wavelength of 609 nm and a bandwidth of 180 nm is used to block the excitation light.

The square modulation signal from a waveform generator and the distorted square signal from the photoelectric detector are sent to a digitizer (PicoScope, Pico Technology, Cambridgeshire, UK). Then resulting signal at frequency of 160kHz is decomposed from square waves and distorted square waves with Fast Fourier Transform. The phase shift between the two sinusoidal signals were measured to quantify the DO concentration in the water sample. The water samples were prepared by bubbling oxygen or nitrogen through the drinking water to get a certain DO concentration. It was then delivered into the water channel with a syringe pump at 50 μ l/s. Before delivery, the DO concentration in the sample are measured with a commercial DO sensor (ExStik® DO600, Extech Instruments, Waltham, MA). All experiments are performed at room temperature. This setup

can be miniaturized in a low-cost and portable design with customized printed circuit boards and embedded software in the future.

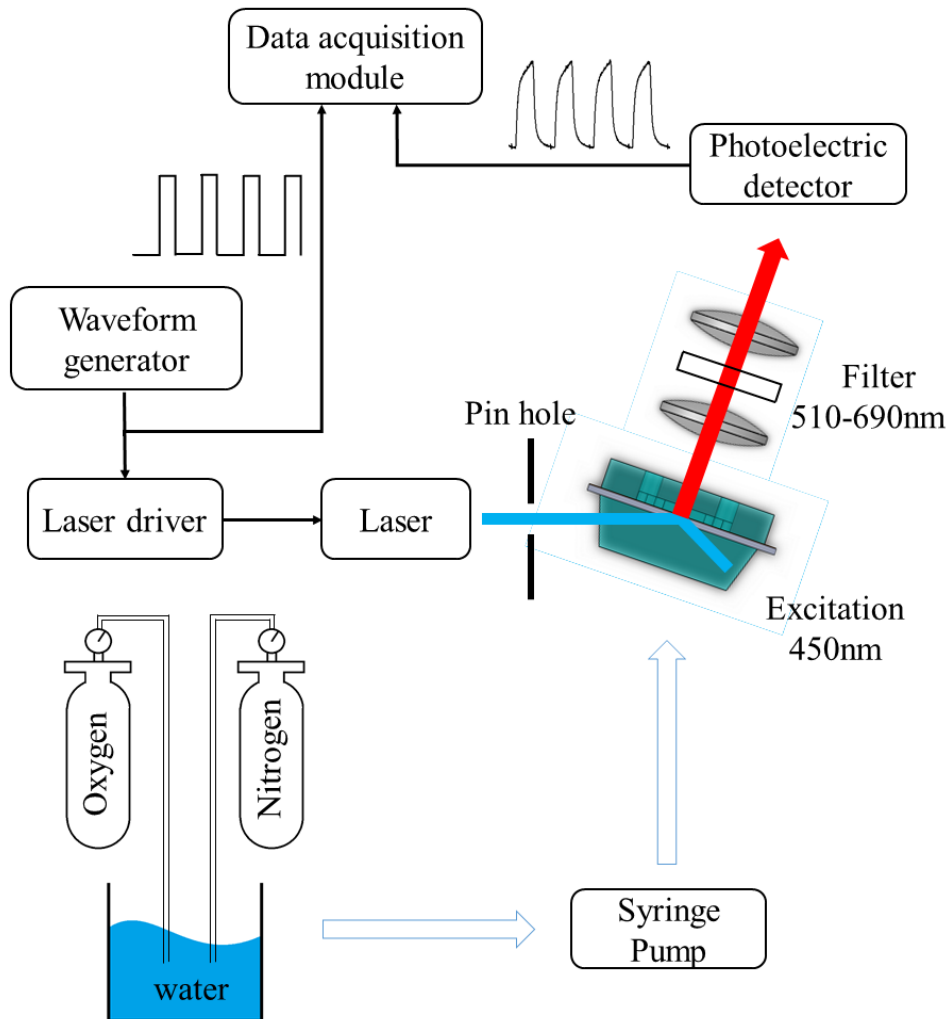


Figure 2-3. Customized frequency domain DO setup

2.4 Results and Discussion

2.4.1 Enhancement of Fluorescence Signal

To verify to the enhancement of fluorescence intensity by the TIR design and prism coupling, two excitation configurations are compared: 1) excitation

without meeting the TIR condition, i.e. the excitation beam was coupled from the bottom chip at the incident angle of 45 degrees; and 2) excitation with the TIR at the optimum excitation angle of 80 degrees. The fluorescence intensity is measured with a power meter. Then two excitation configurations are used sequentially, and the measurements were repeated 8 times, as shown in the Fig. 2-4(a). The results shown in Fig. 2-4(b) indicate that the collected fluorescence intensity is increased by 2.7 times by using prism coupling with an incident angle of 80 degrees. The enhancement factor is lower than that in the simulation, which may be the result of scattering in the DO sensitive layer. The enhancement of fluorescence intensity contributes to a better SNR (signal noise ratio) of photodetector output which is a key factor that affects the limit of detection. Alternatively, lower power lasers and low-cost photo detectors can be used to miniaturize the overall system size with reduced cost. These improvements will enable potential integration of all component on a single detection chip in the future.

2.4.2 DO Sensing Performance

To evaluate the performance of DO sensor, sensing resolution, repeatability and response time are tested. The DO sensor is calibrated against the commercial DO sensor reading using water samples at seven different DO concentrations: 12.80 ppm, 9.90 ppm, 7.65 ppm, 5.65 ppm, 4.05 ppm, 1.71 ppm, and 0.10 ppm. For each sample, 6 separate measurements were taken respectively. For each one measurement, 256 cycles of a square signal are sent to a laser driver, and the total exposure time is 0.8 ms. The phase shift caused by instrumentation response was measured with a reference microfluidic chip without the Ru complex in the DO sensitive layer. As shown in Fig. 2-5, the phase shift decreases as the DO concentration increases. Then a calibration curve is obtained using linear interpolation between the calibration points.

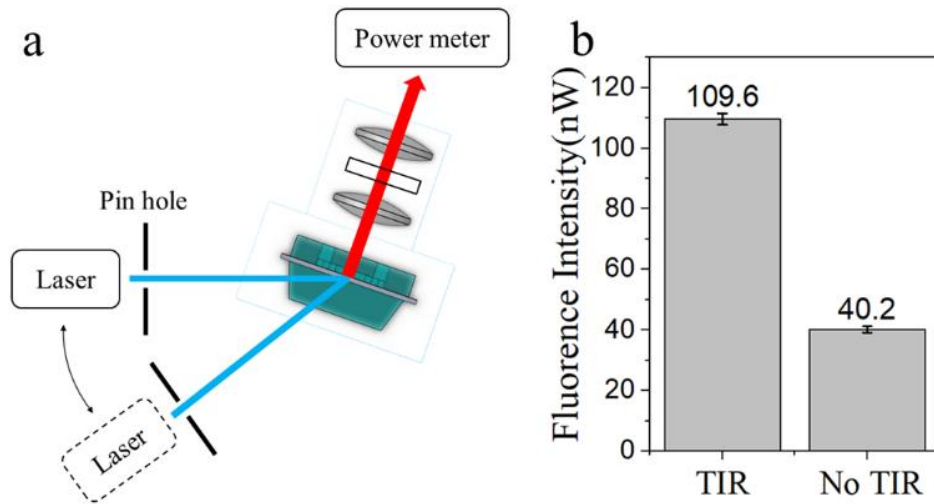


Figure 2-4. Comparison of fluorescence intensity between two excitation configurations: TIR and no TIR. (a) experimental configurations. Laser and pinhole are moved to switch excitation configurations. (b) experimental results. The error bar is standard deviation over 4 repeated measurements. This error is caused by slight alignment difference among measurements.

The resolution of DO measurements at each point can be obtained using the production of standard deviation (SD) of the phase shift among 6 measurements and the slope of the oxygen concentration-phase shift curve. As a result, a measurement resolution of 0.19 ppm is obtained at 9.90 ppm where the SD of measured DO is largest. The standard error for SD estimation is 0.03ppm. This measurement resolution is comparable to some commercially available optical DO sensors [30] with a resolution of 0.1ppm, which are commonly used in environmental and biological applications. There are two approaches that can improve the DO resolution of proposed device when better a measurement resolution is required: (i) using moving average with a long time period (ii) using a fluorophore with higher oxygen sensitivity, such as, Pt complex [29].

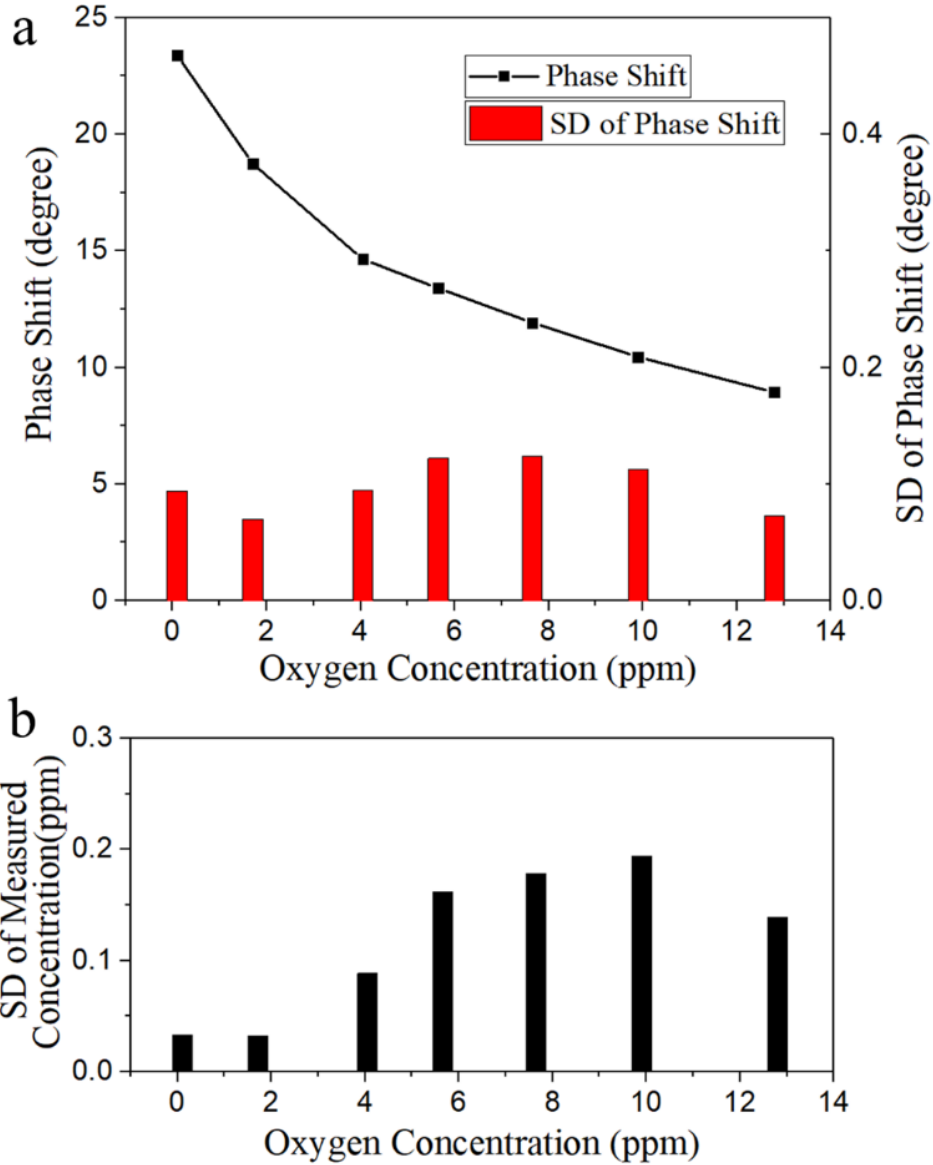


Figure 2-5. Measured phase shift as a function of DO concentration. (a) A calibration curve is obtained to predict the DO concentration of unknown phase shift. Linear interpolation is used between 7 calibration points. The standard deviation of the phase shift over 6 repeated measurements is shown at each calibration point. (b) The resolution of measured DO concentrations.

The measurement repeatability was characterized using samples at two different oxygen concentration: 0.10 ppm and 7.59 ppm. The samples were prepared at the two oxygen concentrations, which were verified by the commercial DO sensor. Then they were measured sequentially 150 seconds after each water

sample injection. The measurements were repeated 8 times. The measurement results indicate an excellent repeatability of the DO sensing: ± 0.2 ppm at 7.59 ppm and ± 0.05 ppm at 0.10 ppm, as shown in Fig. 2-6.

The response time of the frequency domain DO device was characterized. The response time is defined as 90% of the response (or recovery) time when switching between two samples at two different oxygen concentration: 0.10 ppm and 7.59 ppm. As shown in Fig. 2-7, the water switch occurs after 8 seconds measurements begin, and there is a lag time before the measured DO concentration become stable. The main contributor of this lag time is the oxygen diffusion between water and the PDMS membrane until equilibrium is reached. Therefore, a thinner DO sensitive layer is helpful to reduce response time. However, a thinner DO sensitive layer may have a negative effect on DO sensitivity due to weak fluorescence intensity [20]. Currently, this frequency domain DO device has a response time of 23 s when switching from deoxygenated water to oxygenated water and 40 s when switching from oxygenated water to deoxygenated water. These results show that the frequency domain DO device can response to oxygen variation in less than one minute which is fast enough for most of water monitoring applications [31].

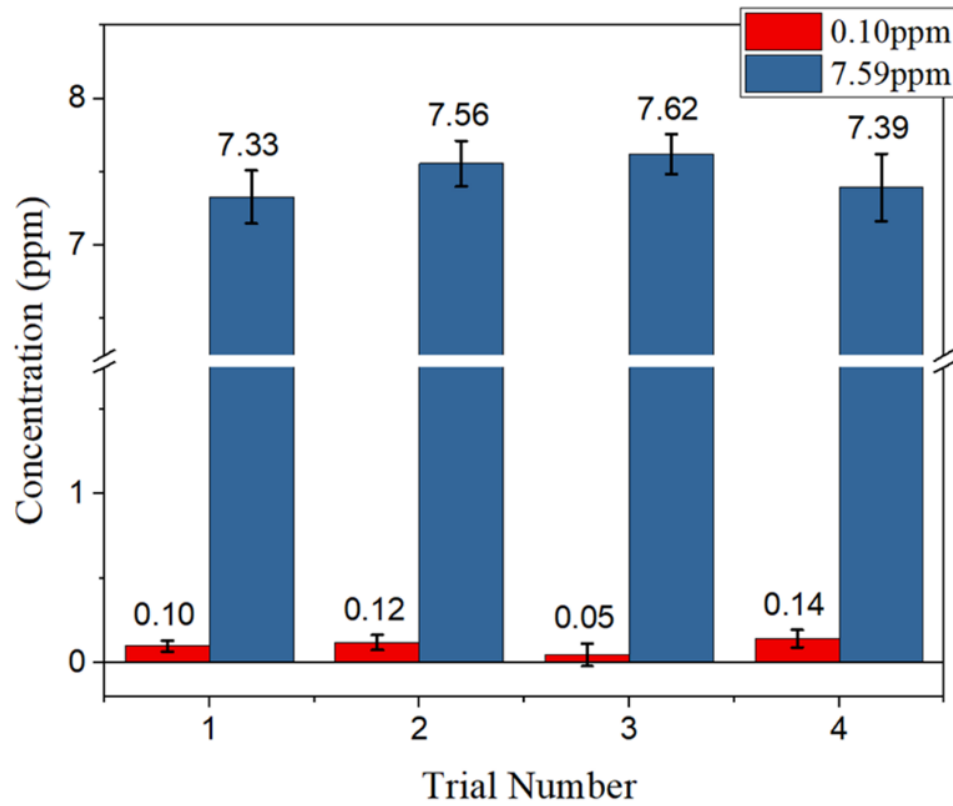


Figure 2-6. Repeatability results of DO measurements using two samples. Red: using water sample with 0.10 ppm DO. Blue: using water sample with 7.59 ppm DO. The error bars are calculated from the standard deviation (SD) of 6 measurements.

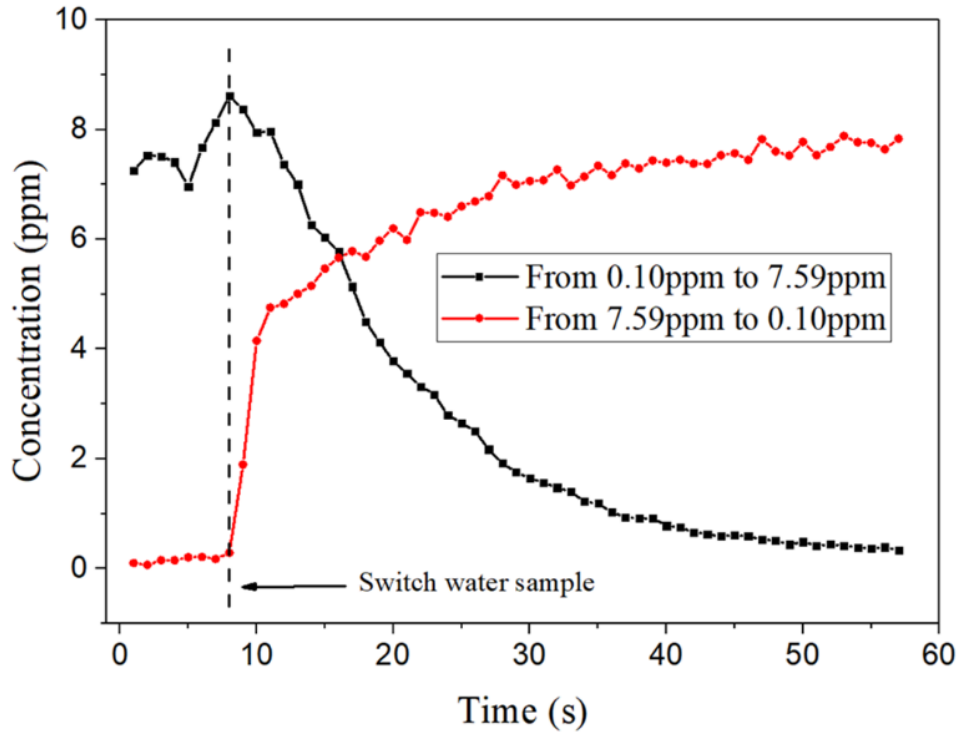


Figure 2-7. Response curves of frequency domain DO device when switching between two samples at two different oxygen concentration: Red line shows the measured DO when switching from 0.10 ppm sample to 7.59 ppm sample. Black line shows the measured DO when switching from 7.59 ppm sample to 0.10 ppm sample. DO concentration is measured with a sampling rate of 1 Hz.

2.4.3 Accelerated Photobleaching Test

An accelerated photobleaching test is performed to estimate the photobleaching effect on the frequency domain optofluidic platform. A 128 s exposure was used to induce photobleaching, which corresponds to 80,000 DO measurements ($80k = 128 * 160 k / 256$). Water sample with a DO concentration of 8.38 ppm is injected and the DO concentration is monitored with the optofluidic platform. Assuming that the DO measurement is taken 6 times per hour in a long-term monitoring setting, this 128 s exposure corresponds to 18 months of regular use. As shown in Fig. 2-8, the measured fluorescence intensity decreases about 20% during 128 s. According to Equation (1), the decrease of fluorescence intensity can result in a drift when DO is quantified by static fluorescence intensity

measurements. When the frequency domain method is used, fluctuation of the measured DO concentration is about ± 0.4 ppm and the drift is suppressed dramatically. These results show that the proposed frequency-domain optofluidic platform is suitable for long-term monitoring because frequency-domain methods could be less sensitive to photobleaching or other variations of fluorescence intensity.

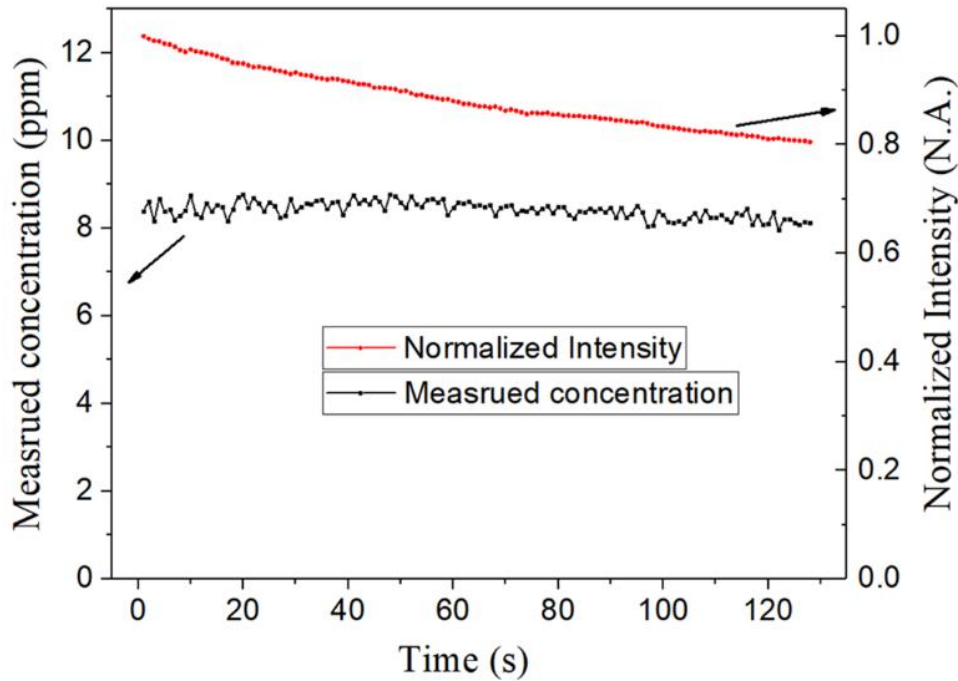


Figure 2-8. Accelerated photobleaching test of frequency domain DO device. Red line and black line show the normalized fluorescence intensity and measured DO concentration over 128 s, respectively. DO concentration is measured with a sampling rate of 1 Hz.

2.5 Conclusion

In summary, a frequency domain optofluidic dissolved oxygen sensor with a TIR enhancement is developed. The DO sensor has a resolution of 0.2 ppm over a concentration range of 0.1 ppm to 12.8 ppm. This platform is suitable for long-term monitoring owing to the frequency-domain method and an efficient TIR design. The use of microfluidic platforms allows preprocessing of the sample,

such as temperature control and adding reagent. Thus, cell culture BOD monitoring could be enabled in the optofluidic platform.

TIR design increased fluorescence signal and minimized background autofluorescence from fluorophore in the sample fluidic channel since the excitation is confined within the non-fluidic layers. Consequently, enhanced sensitivity could enable in situ monitoring of oxygen concentrations in biological samples as well as oxygen consumption rates. When combined with the TIR design, measurements can be conducted without optically damaging the cells themselves or photobleaching intrinsic fluorophores as the excitation light does not enter the fluid channel. The design could have applications in cell culture monitoring and embryo assessment [11-12, 32].

A low-cost luminescent lifetime imaging method that developed recently can be potentially applied to this design [14]. FLIM measurement of fluorescent films or foils have been explored as a method for monitoring extracellular oxygen as an indication of the oxygenation and oxygen consumption of cells and tissues [12, 31]. Although these films are not able to visualize the distribution of oxygen within individual cells, they are easy to fabricate, low-cost, and do not negatively impact cell viability as the indicator does not need to be delivered into the cells [11]. Fabricating fluid channels or micro-wells above oxygen sensitive phosphorescent films enables monitoring the oxygenation of fluids being delivered to cell cultures or monitoring the microenvironment of individual wells [32].

Acknowledgment. This project is supported in part by the Natural Science and Engineering Research Council (NSERC) of Canada, the Province of Ontario through an Ontario Research Fund (ORF-RE). QF held the Canada Research Chair in Biophotonics. BX holds a Chinese Scholarship Council PhD scholarship and EM held an Ontario Graduate Scholarship and a McMaster Faculty of Engineering Dean's PhD Excellence Scholarship.

References

- [1] U.S. Environmental Protection Agency, “Chapter 9: Dissolved oxygen and biological oxygen demand,” in *Voluntary Estuary Monitoring Manual: A Methods Manual*, 2nd ed. Washington, DC, USA: U.S. Environmental Protection Agency, Office of Wetlands Oceans and Watersheds, Mar. 2006.
- [2] Zoumis T, Schmidt A, Grigorova L, Calmano W. Contaminants in sediments: remobilisation and demobilisation. *Science of the total environment*. 2001 Feb 5;266(1-3):195-202.
- [3] Lee JH, Hodgkiss IJ, Wong KT, Lam IH. Real time observations of coastal algal blooms by an early warning system. *Estuarine, Coastal and Shelf Science*. 2005 Oct 1;65(1-2):172-90.
- [4] Hou D, Song X, Zhang G, Zhang H, Loaiciga H. An early warning and control system for urban, drinking water quality protection: China’s experience. *Environmental Science and Pollution Research*. 2013 Jul 1;20(7):4496-508.
- [5] Garrido JM, Van Benthum WA, Van Loosdrecht MC, Heijnen JJ. Influence of dissolved oxygen concentration on nitrite accumulation in a biofilm airlift suspension reactor. *Biotechnology and bioengineering*. 1997 Jan 20;53(2):168-78.
- [6] Åmand L, Carlsson B. The optimal dissolved oxygen profile in a nitrifying activated sludge process—comparisons with ammonium feedback control. *Water science and technology*. 2013 Aug;68(3):641-9.
- [7] Barker DJ, Mannucchi GA, Salvi SM, Stuckey DC. Characterisation of soluble residual chemical oxygen demand (COD) in anaerobic wastewater treatment effluents. *Water Research*. 1999 Aug 1;33(11):2499-510.
- [8] Jouanneau S, Recoules L, Durand MJ, Boukabache A, Picot V, Primault Y, Lakel A, Sengelin M, Barillon B, Thouand G. Methods for assessing biochemical oxygen demand (BOD): A review. *Water research*. 2014 Feb 1;49:62-82.
- [9] Kim M, Kim Y, Kim H, Piao W, Kim C. Evaluation of the k-nearest neighbor method for forecasting the influent characteristics of wastewater treatment plant. *Frontiers of Environmental Science & Engineering*. 2016 Apr 1;10(2):299-310.

- [10] Kusiak A, Verma A, Wei X. A data-mining approach to predict influent quality. *Environmental monitoring and assessment*. 2013 Mar 1;185(3):2197-210.
- [11] Papkovsky DB, Dmitriev RI. Imaging of oxygen and hypoxia in cell and tissue samples. *Cellular and molecular life sciences*. 2018 Aug 1;75(16):2963-80.
- [12] Zhao Y, Liu L, Luo T, Hong L, Peng X, Austin RH, Qu J. A platinum-porphine/poly (perfluoroether) film oxygen tension sensor for noninvasive local monitoring of cellular oxygen metabolism using phosphorescence lifetime imaging. *Sensors and Actuators B: Chemical*. 2018 Sep 15;269:88-95.
- [13] Sanchez T, Venturas M, Aghvami SA, Yang X, Fraden S, Sakkas D, Needleman DJ. Combined noninvasive metabolic and spindle imaging as potential tools for embryo and oocyte assessment. *Human Reproduction*. 2019 Dec 1;34(12):2349-61.
- [14] Chelushkin PS, Tunik SP. Phosphorescence lifetime imaging (PLIM): State of the art and perspectives. In *Progress in Photon Science 2019* (pp. 109-128). Springer, Cham.
- [15] Hou J, Wright HJ, Chan NS, Tran RD, Razorenova OV, Potma EO, Tromberg BJ. Correlating two-photon excited fluorescence imaging of breast cancer cellular redox state with seahorse flux analysis of normalized cellular oxygen consumption. *Journal of biomedical optics*. 2016 Jun;21(6):060503.
- [16] Jahn K, Buschmann V, Hille C. Simultaneous fluorescence and phosphorescence lifetime imaging microscopy in living cells. *Scientific reports*. 2015 Sep 22;5:14334.
- [17] Carpenter JH. THE ACCURACY OF THE WINKLER METHOD FOR DISSOLVED OXYGEN ANALYSIS 1. *Limnology and Oceanography*. 1965 Apr;10(1):135-40.
- [18] Clark Jr LC, Lyons C. Electrode systems for continuous monitoring in cardiovascular surgery. *Annals of the New York Academy of sciences*. 1962 Oct;102(1):29-45.

- [19] Hsu L, Selvaganapathy PR, Brash J, Fang Q, Xu CQ, Deen MJ, Chen H. Development of a low-cost hemin-based dissolved oxygen sensor with anti-biofouling coating for water monitoring. *IEEE Sensors Journal*. 2014 Jun 24;14(10):3400-7.
- [20] Mahoney EJ, Hsu HH, Du F, Xiong B, Selvaganapathy PR, Fang Q. Optofluidic dissolved oxygen sensing with sensitivity enhancement through multiple reflections. *IEEE Sensors Journal*. 2019 Aug 2;19(22):10452-60.
- [21] Quaranta M, Borisov SM, Klimant I. Indicators for optical oxygen sensors. *Bioanalytical reviews*. 2012 Dec 1;4(2-4):115-57.
- [22] Morris KJ, Roach MS, Xu W, Demas JN, DeGraff BA. Luminescence lifetime standards for the nanosecond to microsecond range and oxygen quenching of ruthenium (II) complexes. *Analytical chemistry*. 2007 Dec 15;79(24):9310-4.
- [23] Bambot SB, Holavanahali R, Lakowicz JR, Carter GM, Rao G. Phase fluorometric sterilizable optical oxygen sensor. *Biotechnology and bioengineering*. 1994 May;43(11):1139-45.
- [24] Chu CS, Lo YL, Sung TW. Review on recent developments of fluorescent oxygen and carbon dioxide optical fiber sensors. *Photonic Sensors*. 2011 Sep 1;1(3):234-50.
- [25] McDonagh C, Kolle C, McEvoy AK, Dowling DL, Cafolla AA, Cullen SJ, MacCraith BD. Phase fluorometric dissolved oxygen sensor. *Sensors and Actuators B: Chemical*. 2001 Apr 15;74(1-3):124-30.
- [26] Yeh SC, Patterson MS, Hayward JE, Fang Q. Time-resolved fluorescence in photodynamic therapy. In *Photonics 2014 Dec* (Vol. 1, No. 4, pp. 530-564). Multidisciplinary Digital Publishing Institute.
- [27] Liu R, Zhao Z, Zou L, Fang Q, Chen L, Argento A, Lo JF. Compact, non-invasive frequency domain lifetime differentiation of collagens and elastin. *Sensors and Actuators B: Chemical*. 2015 Nov 1;219:283-93.
- [28] Xiong B, Fang Q. Luminescence lifetime imaging using a cellphone camera with an electronic rolling shutter. *Optics Letters*. 2020 Jan 1;45(1):81-4.

[29] Chu CS, Lo YL, Sung TW. Enhanced oxygen sensing properties of Pt (II) complex and dye entrapped core-shell silica nanoparticles embedded in sol-gel matrix. *Talanta*. 2010 Aug 15;82(3):1044-51.

[30] <https://www.ysi.com/pro20> (2020).

[31] Lo JF, Wang Y, Blake A, Yu G, Harvat TA, Jeon H, Oberholzer J, Eddington DT. Islet preconditioning via multimodal microfluidic modulation of intermittent hypoxia. *Analytical chemistry*. 2012 Feb 21;84(4):1987-93.

[32] Zhu F, Baker D, Skommer J, Sewell M, Wlodkowic D. Lab-on-a-chip technology for a non-invasive and real-time visualisation of metabolic activities in larval vertebrates. In *Bio-Mems and Medical Microdevices Ii 2015 Jun 1* (Vol. 9518, p. 951813). International Society for Optics and Photonics.

Chapter 3.

Paper II - Dual-modality imaging optofluidic cytometer for onsite detection and identification of phytoplankton

Bo Xiong,¹ Herbert Schellhorn² and Qiyin Fang^{1*}

¹School of Biomedical Engineering, McMaster University, Ontario, L8S 4L8, Canada

²Department of Biology, McMaster University, Ontario, L8S 4L8, Canada

This manuscript has been submitted to Advanced Photonics.

Introduction to Paper II:

Detection of microbes, such as phytoplankton, parasites, and pathogenic bacteria, is necessary for water quality monitoring. This chapter describes the development of an imaging-based optofluidic platform for onsite microbe detection. Phytoplankton detection was demonstrated on this platform using imaging processing algorithms that allow automated cell counting and classification. To mitigate dependence on bulky microscopes in imaging-based optofluidic devices, a portable and low-cost imaging system that can observe morphological features as well as fluorescent features was developed.

In this work, a low-cost and portable imaging optofluidic cytometry approach with two imaging modalities was developed. Shadows and interference patterns are captured by a lensless camera in the lensless imaging mode. Fluorescence emitted from each particle are measured by a separate low-cost and compact camera in the fluorescence imaging mode. The developed imaging-based optofluidic platform was demonstrated by measuring *Chlamydomonas*, *Euglena*, and 10 μm non-fluorescent beads in separate and mixed flow samples. This work shows the effectiveness of imaging-based optofluidic platform with dual-modality imaging approach as a solution for onsite monitoring.

I was inspired to develop an optofluidic platform for phytoplankton monitoring in my comprehensive exam in November 2018. I developed a concept of dual imaging modality for optofluidic platforms. And I designed and built the imaging system with the help of Mr. Ian Phillips and Dr. Eric Mahoney. I performed experiments and analyzed results with the help of Mr. Tianqi Hong. I took a lead role in the manuscript writing.

Contents of Paper II

Abstract

Phytoplankton monitoring is essential for better understanding and mitigation of phytoplankton bloom formation. We present an optofluidic cytometer with two imaging modalities for onsite detection and identification of phytoplankton: the lensless imaging mode for morphological features and the fluorescence imaging mode for autofluorescence signal of phytoplankton. Both imaging modes are realized by miniaturized devices, while achieving a field-of-view (FoV) of 3.7 mm x 2.4 mm and a depth of field (DoF) of 0.8 mm. The particles in the water flow channel can be detected and classified with automated image processing algorithms and machine learning models using integrated morphology and fluorescence features. The performance of the device was demonstrated by measuring *Chlamydomonas*, *Euglena*, and 10 μm non-fluorescent beads in both separate and mixed flow samples. The recall accuracy for *Chlamydomonas* and *Euglena* was better than 93%. The dual-modality imaging approach enabled observing both morphology and fluorescence features with a large DoF and FoV which contribute to high-throughput analysis. Moreover, this imaging flow cytometer platform is portable, low-cost and shows potential in the onsite phytoplankton monitoring.

3.1 Introduction

Phytoplankton play a vital role in the aquatic ecosystem [1][2]. However, species composition, concentration, and distribution of phytoplankton change frequently while the drivers of these changes are not fully understood [3]. Phytoplankton bloom, a rapid growth in the algal population, can readily occur under favorable environmental conditions, posing a threat to human and ecosystem

health, and resulting in economic losses in agriculture [4]. For example, some phytoplankton species produce toxins are harmful to both fish and human [5]; algae bloom can result in oxygen depletion, killing fish and benthic organisms [6]. Therefore, it is necessary to closely monitor the phytoplankton bloom development for better mitigation strategies [7-9]. Conventional phytoplankton detection relies on its autofluorescence signatures and morphological features. Currently, both methods are performed by laboratory instruments (e.g., fluorometers and microscopes) and require manual sampling handling [10-12]. This approach is time-consuming and expensive due to the needs of manual steps by experienced technical staff. Thus, there is a pressing need for low-cost and efficient identification techniques that can detect the species composition and concentration of phytoplankton in situ.

Several commercial instruments based on fluorescent spectroscopic sensing are available for onsite phytoplankton monitoring where concentration of chlorophyll and other pigments (such as phycocyanin, phycoerythrin, and carotenoids) can be estimated based on their autofluorescence [13][14]. With these instruments, the phytoplankton can be classified into a few major groups based on their color, such as green algae, red algae, and blue-green algae. That said, the fluorometers cannot count phytoplankton cells/colonies and further classification of phytoplankton species is difficult when multiple species of phytoplankton are presented in the water sample [15].

Imaging-based flow cytometry, which combines microscopy and flow cytometry, has become a powerful technology that can be used for observation and identification of phytoplankton at the cellular level [16-19]. A sheath flow is used to confine the sample particles to a focus point of a microscope objective lens. Then morphology features and autofluorescence can be measured for particle classification. To capture images with micrometer-level resolution, microscope objectives with high numerical aperture are used. As a result, the field of view (FoV) and depth of focus (DoF) are reduced, leading to limited volumetric throughput and

the need for focus adjustments [20]. At present, the imaging-based flow cytometers are typically bulky and expensive [20-22], limiting their use in onsite monitoring.

Lensless imaging provides an alternative microscopic approach in which the shadow of a sample is recorded on an image sensor directly [23][24]. Lensless imaging has several advantages over conventional microscopes including large FoV and DoF, simple alignment, cost-effectiveness, and portability. When a coherent light source is used, the shadows with fringe interference patterns can be observed. Then the samples in a wide range of depths can be observed with high-spatial resolution after holographic reconstruction [25,26]. Recently, lensless imaging has been used for morphological observation of particles/cells in the fluidic samples, such as, characterization of microplastics [27], urine analysis [28, 29], blood analysis [30] and phytoplankton analysis [31]. Nevertheless, a separate fluorescence analysis measurement is still commonly required in phytoplankton identification [12,17,21,22,32]. A lensless setup can be configured to provide fluorescence imaging by an emission filter between image sensor and fluidic channel [23]. However, the resolution of lensless fluorescence imaging is limited by the point spread function (PSF), which is dominated by the distance between particles/cells and image sensor [23]. Considering a typical distance of 200 μm , the imaging resolution is about 200 μm [23][33][34], which is insufficient for phytoplankton analysis. Recently, a number of techniques have been investigated to improve the resolution of fluorescence lensless imaging including hardware designs and computational algorithms [23]. Spatial resolution can be improved by digital deconvolution of incoherent PSF which require precise distance between the detected cell and imager [33]. However, this distance is varied and unknow when a cell is flowing flow through a fluidic channel without hydrodynamic focusing. Custom-fabricated imagers with nanostructures/microstructures designs have been investigated to improve the resolution of fluorescence lensless imaging [35]. High resolution can be realized when the sample are closed to the nanostructures/microstructures or placed at particular “points”. However, these

methods typically reduce DoF and FoV [36] and increase complexity, limiting their use in onsite phytoplankton monitoring.

In this work, we developed a dual-modality imaging optofluidic cytometry approach with large FoV and DoF, while keep device cost low and portable for onsite detection and identification of phytoplankton. This dual-modality imaging approach allows single-cell analysis without using bulky and expensive microscope setups. In the lensless imaging mode, shadow and fringe patterns of each particle are captured by a lensless camera. In the fluorescence imaging mode, autofluorescence emitted from each particle are measured by another low-cost and compact camera with a separate excitation light and an emission filter. Image processing algorithms and machine learning models have been developed to facilitate automated phytoplankton detection and classification in the water samples with integrated morphology and fluorescence features. The performance of the device was demonstrated by measuring *Chlamydomonas*, *Euglena*, and 10 μm non-fluorescent beads in both separate and mixed flow samples.

3.2 Materials and Methods

3.2.1 Materials

Phytoplankton samples, *Chlamydomonas* (CPCC 243) and *Euglena* (CPCC 95), were purchased from Canadian Phycological Culture Centre (Waterloo, ON). *Chlamydomonas* and *Euglena* contain Chlorophyll α , which emits fluorescent light with a peak of 690 nm under blue or ultraviolet excitation [37]. For comparison purposes, 10 μm polystyrene (PS) beads (Polysciences, Warrington, PA) are used. Excitation and illumination diode lasers at 405 nm and 632 nm were used (Wuhan Besram Technology, Wuhan, China). Low-cost cameras (Raspberry Pi camera v2) were used to build customized camera modules. Customized glass slides with a thickness of 0.33mm (Luoyang Ancient Glass Ltd Co., Luoyang, China) and Polydimethylsiloxane (PDMS) (Sylgard 184, Dow Corning, Midland, MI) were used to build the microfluidics channels.

3.2.2 System Design

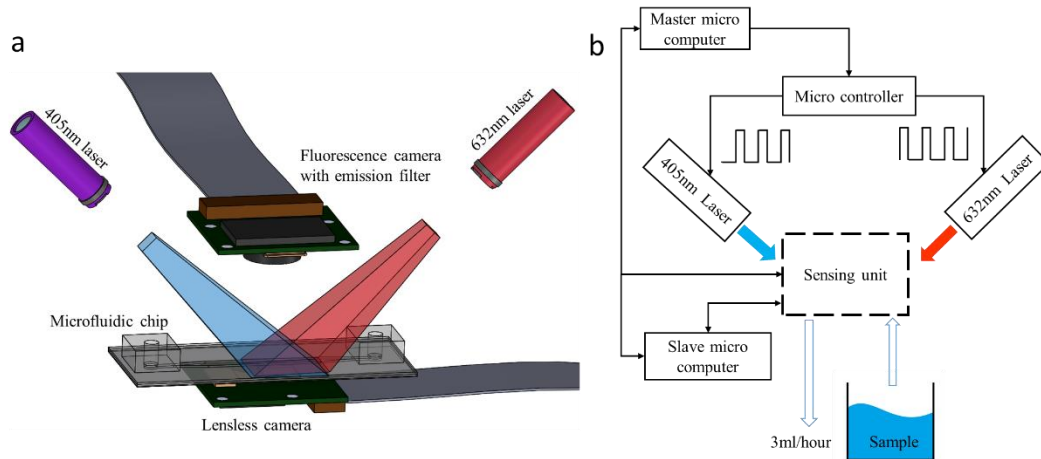


Figure 3-1. (a) A schematic of optofluidic imaging flow cytometer, including a microfluidic chip, a lensless camera, a fluorescence camera and two lasers. A fluidic channel is illuminated by a 405 nm laser and a 632 nm laser alternatively in time. The lensless camera is placed beneath a microfluidic chip and matches the illumination area. The fluorescence camera is placed above the microfluidic chip. A 590 nm log-pass filter is mounted on the camera lens to block the 405 nm excitation light for fluorescence imaging. (b) A block diagram of experimental setup. The sensing unit in the block diagram includes two cameras and a microfluidic chip.

A schematic of the optofluidic imaging flow cytometer with two cameras is shown in Fig. 3-1(a). An imaging lens was removed from a camera for lensless imaging. A microfluidic chip was placed above the image sensor. The FoV of the lensless camera is 3.7 mm x 2.4 mm which is equal to the dimension of the image sensor. In the lensless imaging mode, a 632 nm laser is used for illumination. Thus, the particles' shadows and the interference patterns can be recorded on the image sensor. In the lensless imaging mode, the 405 nm excitation laser must be switched off to mitigate over exposure, since the 405 nm laser was much powerful than the 632 nm laser. Another camera with a built-in lens was placed 2.5 cm above the microfluidic chip to acquire the fluorescence images. The built-in lens position was adjusted to allow focusing on the fluidic channel. A low-cost emission filter

(WRATTEN No. 29, $\lambda > 590$ nm, Eastman Kodak, Rochester, NY) was mounted on the lens of fluorescence camera to reject the 405 nm excitation light. Thus, red fluorescence images can be captured in the fluorescence imaging mode when 405 nm laser is switched on.

A block diagram of the experimental setup is shown in Fig. 3-1(b). A microcontroller (Uno, Arduino) sent two synchronized 1.8 Hz square waves to two lasers. Since the phase difference between two square waves was 180 degree, the illuminations from two lasers are separated in time. Fluid samples were delivered into microfluidic channel with a flow rate of 3 ml/h ($0.83 \mu\text{l/s}$). Two microcomputers (Raspberry pi 4) were used as a master and a slave to control two cameras and record videos at 25 frames per second (fps). The master microcomputer controlled the slave microcomputer and the microcontroller to maintain the synchronization between the cameras and lasers. The recorded videos were processed off-line on a separate computer workstation. A few frames are shown in Fig. 3-2 to illustrate lensless images and fluorescence images (see a video in Supplement 1). The total cost of the main modules, including sensing unit, microcomputers, microcontroller, and lasers is less than \$300 USD.

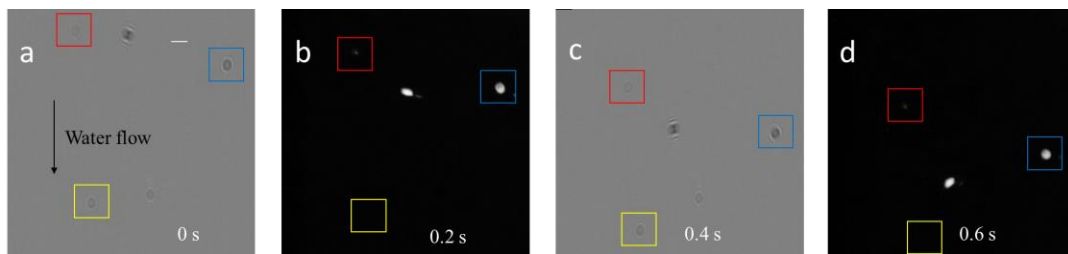


Figure 3-2. Four frames captured at 0 s, 0.2 s, 0.4 s, and 0.6 s respectively. (a) and (c) are captured in the lensless imaging mode. (b) and (d) are captured in the fluorescence imaging mode. The direction of water flow and 100 μm scale bar is shown in (a). A *Chlamydomonas* cell (red), a *Euglena* cell (blue) and a 10 μm PS bead (yellow) are labeled in these four frames.

3.2.3 Microfluidic Chip Design

The microfluidic chip design features a removable flow module separate from the lensless camera. As shown in the Fig. 3-3(a), the removable flow module consisted of three glass slides: a top layer, a middle layer, and a bottom layer. The height of fluidic channel was 0.33 mm which depends on the thickness of middle layer. The width of water channel was 2.6 mm, covering an active area of 6.2 mm^2 ($2.6 \text{ mm} \times 2.4 \text{ mm}$) on the image sensor. A PDMS adaptor was bonded to the top layer for tubes insertion. The removable flow module was mounted on the lensless camera using a 3D printed adaptor. The distance between the fluidic channel and the image sensor was about 1 mm. After each use the removable flow module can be cleaned by detergent, and it can be replaced by a new one if necessary.

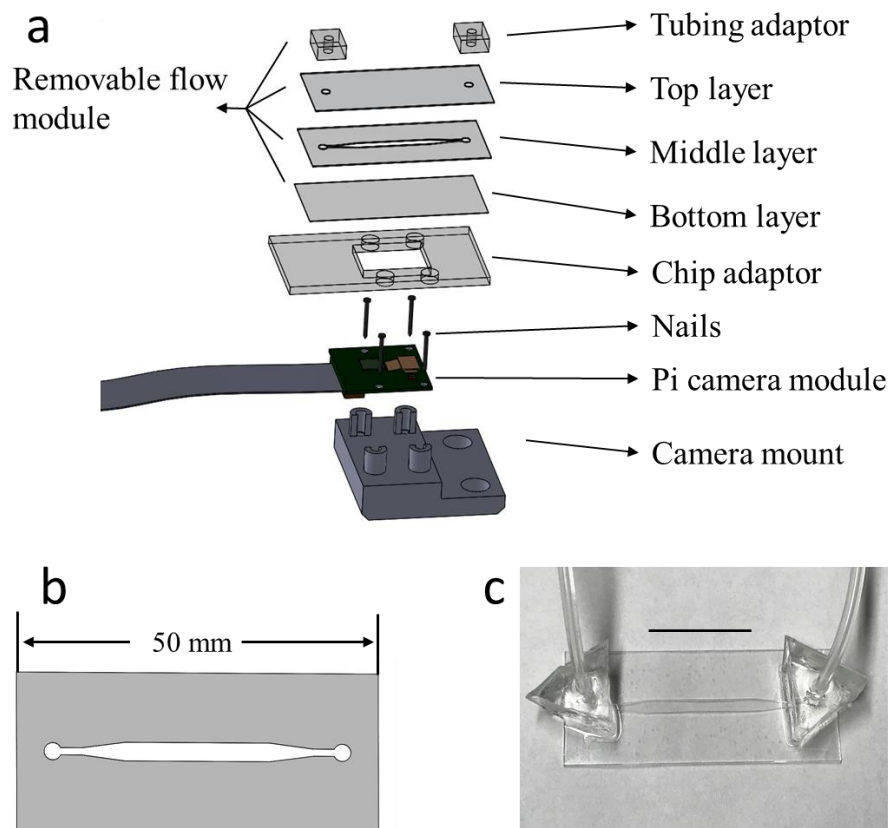


Figure 3-3. Description of chip design. (a) A explode view of the microfluidic chips and lensless

camera. (b) A top view of the middle layer which determine the shape and thickness of the fluidic channel. (c) A photo of the removable flow module.

3.2.4 Image Processing Algorithms

Detection and tracking algorithms were developed in Python with the OpenCV and Sklearn packages, as shown in Fig. 3-4. Background is subtracted to remove the particles adhering to the microfluidic channel walls in the videos. Histogram of oriented gradients (HOG) and support vector machine (SVM) were used to detect particles in the lensless imaging mode [38]. Once a particle was detected, Discriminative Correlation Filter with Channel and Spatial Reliability (CSR-DCF) was used to track particles between frames [39]. Alternatively, particles were tracked with Kalman filter when the fluorescence imaging mode was on or the CSR-DCF tracker was failed. The view of fluorescence camera was aligned with the view of lensless camera; therefore, particles can be tracked between both imaging modes.

Particle classifications make use of a combination of fluorescence and morphology features. In the lensless imaging mode, the particles' morphology features were extracted using HOG descriptor from their corresponding cropped images. Here, raw holograms without holographic reconstruction were used for morphology analysis to reduce intensive computation. In the fluorescence imaging mode, the particles' fluorescent features including total pixel value, averaged pixel value, dimension, and peak pixel value were calculated from their corresponding cropped images. Then two SVM classifiers were trained for lensless imaging mode and fluorescence imaging mode, respectively. As a particle was detected and tracked in the consecutive frames, classification was performed once per frame using either of SVM classifiers. The results obtained in each frame cast a weighted vote for the final particle classification results.

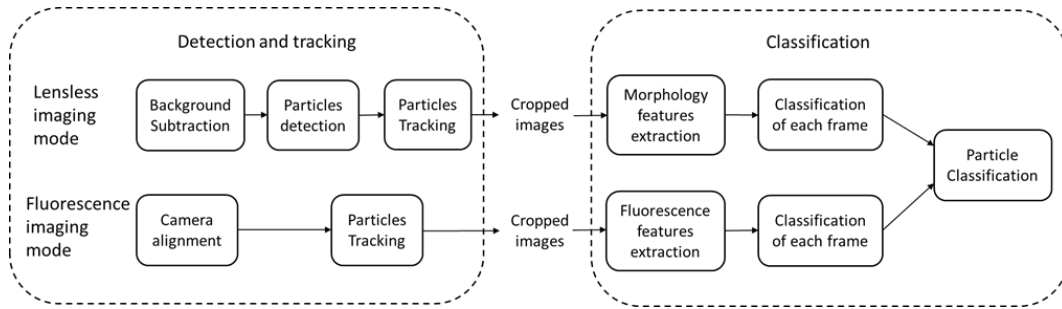


Figure 3-4. The logic flow of image processing algorithms. Particles are detected and tracked in the consecutive frames and both cropped lensless images and cropped fluorescence images are obtained. Then particles can be classified with integrated morphology features and fluorescence features.

3.2.5 Sample Preparation

In order to obtain the ground truth for classifier training and testing, three samples were prepared by diluting *Chlamydomonas*, *Euglena* and PS beads samples in Bold's Basal Medium (BBM), respectively. To evaluate the system performance, six more samples were prepared. Three samples were prepared by diluting a *Chlamydomonas* sample using different dilution ratios. The other three samples were prepared by mixing *Chlamydomonas*, *Euglena*, PS beads samples and BBM. Their ingredients are shown in Table. 3-1. We found that unintended contaminations were presented in both *Chlamydomonas* and *Euglena* samples. Since these particles are not fluorescent, they can be distinguished with phytoplankton cells clearly with fluorescence images.

Table 3-1. Ingredient of samples

Sample ID	<i>Chlamydomonas</i>	<i>Euglena</i>	PS beads	BBM media	Total
#1	0 ml	0 ml	1 ml	29 ml	30 ml
#2	0 ml	2 ml	0 ml	28 ml	30 ml
#3	1.5 ml	0 ml	0 ml	28.5 ml	30 ml
#4	0.5 ml	0 ml	0 ml	29.5 ml	30 ml
#5	1 ml	0 ml	0 ml	29 ml	30 ml
#6	2 ml	0 ml	0 ml	28 ml	30 ml
#7	0.33ml	0.67ml	0ml	29ml	30 ml
#8	0.33ml	1.33ml	0ml	28.33ml	30 ml
#9	0.33ml	0.67ml	0.4ml	28.6ml	30 ml

3.3 Results

3.3.1 Particle Classification

The particle classification algorithms were trained and tested using *Chlamydomonas*, *Euglena* and PS beads samples (sample #3, #2, and #1). A dataset was generated for SVM classifier training and testing, as shown in the Fig. 3-5. The dataset contains 1152 fluorescent particles found in the *Chlamydomonas* sample, 1049 fluorescent particles found in the *Euglena* sample, 1350 non-fluorescent particles found in the PS beads sample. The non-fluorescent contamination found in the *Chlamydomonas* and *Euglena* samples were excluded. These particles are linked to 73,068 cropped lensless images and 72,444 cropped fluorescent images obtained from the videos using the detection and tracking algorithms.

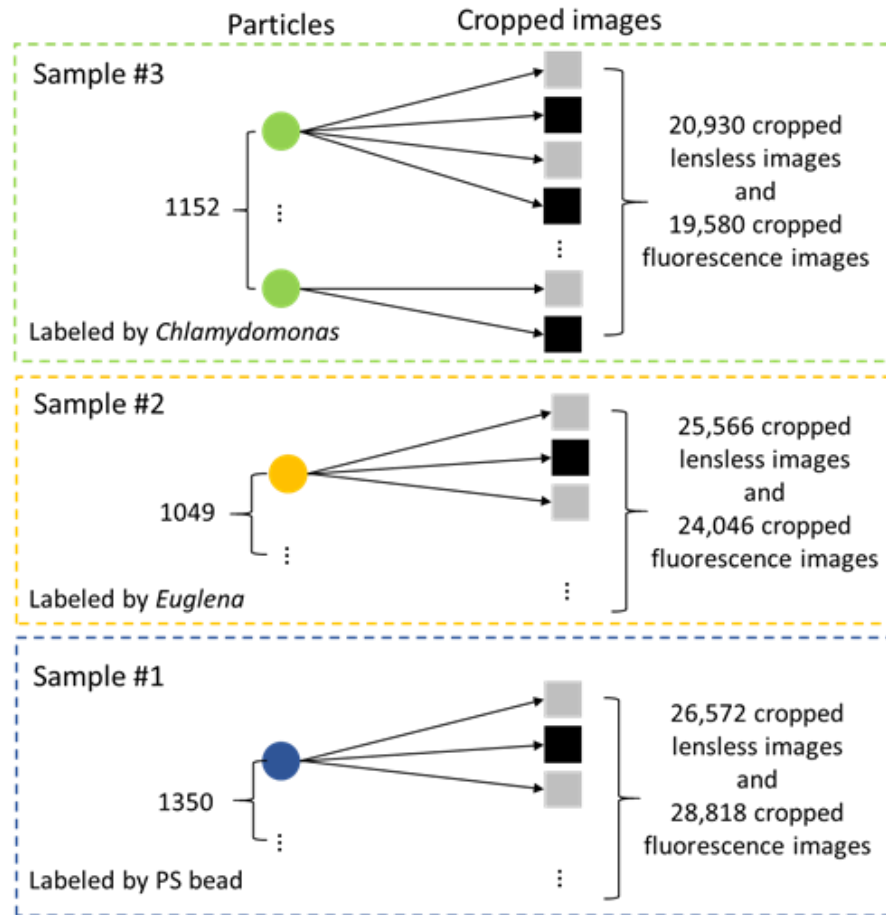


Figure 3-5. Overview of a particle dataset. Totally, there are 3551 particles and their corresponding 145,512 cropped images in the dataset. These particles and cropped images are labelled by Chlamydomonas, Euglena, and PS beads.

A 10 μm polystyrene bead, a Chlamydomonas cell and a Euglena cell were observed by dual-modality imaging. The cropped images captured in the fluorescence imaging mode are shown in Fig.6 (a-c). The cropped images captured in the lensless imaging mode are shown in Fig.6 (d-f). For better visualization of cropped images captured in the lensless imaging mode, holographic reconstruction was performed with angular spectrum method [40]. These reconstructed images are shown in Fig. 6 (h-g). The samples were moved to another lab and observed with a benchtop microscope, and the typical images of Chlamydomonas, Euglena and PS beads under a microscope were shown in the Fig. 6 (k-m). Since Chlamydomonas

and *Euglena* contain Chlorophyll α , they can be seen in the fluorescence imaging mode. On the other hand, PS beads are hardly observed in the fluorescence imaging mode due to lacking fluorophore. *Euglena* cell is typically larger than *Chlamydomonas*. As a result, *Euglena* cell emits stronger fluorescence, and their shadow and optical fringes are more intense. *Chlamydomonas* cells and PS beads have similar size and shape, as shown in Fig. 6. As a result, it could be difficult to distinguish them using morphology features in the lensless imaging mode.

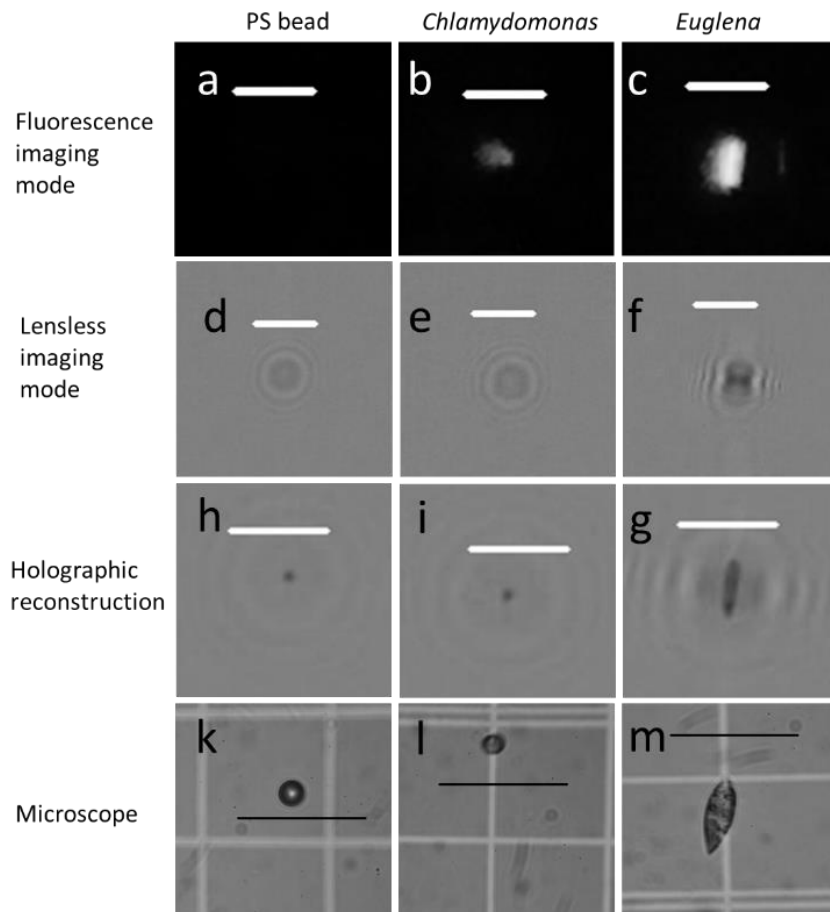


Figure 3-6. Images of 10 μm polystyrene bead, *Chlamydomonas* cell and *Euglena*. (a-c) are captured in the fluorescence imaging mode. (d-f) are captured in the lensless imaging mode. For better visualization, holographic reconstructed images are shown in (d-f). Samples were observed a microscope with a magnification of 400. Their typical images are shown in (k-m). Scale bars are 100 μm.

The dataset was split into a training set and a testing set with a 50-50 ratio. Then two SVM classifiers were trained using the training set. The morphology features were extracted from the cropped lensless images to train the first SVM classifier; The fluorescence features were extracted from the cropped fluorescence images to train the second SVM classifier. The particles in the testing set were classified by integrating two SVM classifiers, and the results of particle classification are shown in Table 3-2. For comparison purposes, the particles were also classified with individual classifiers, and the results are shown in Table 3-3 and Table 3-4. When both SVM classifiers and dual-modality imaging are used, the classification accuracy is the best among three groups of testing results. The recall accuracy of *Chlamydomonas*, *Euglena* and 10 μm PS beads are 0.936, 0.944, 1.000 respectively. These results demonstrate the efficiency of particles classification in the dual-modality imaging approach.

Table 3-2 Confusion matrix of classifier using lensless images and fluorescent images

Class	Predicted: <i>Chlamydomonas</i>	Predicted: <i>Euglena</i>	Predicted: PS bead
Actual: <i>Chlamydomonas</i>	0.936	0.005	0.059
Actual: <i>Euglena</i>	0.016	0.944	0.041
Actual: PS bead	0.000	0.000	1.000

Table 3-3 Confusion matrix of classifier using fluorescent images. PS beads cannot be detected in the fluorescence imaging mode since their fluorescence is too weak.

Class	Predicted: <i>Chlamydomonas</i>	Predicted: <i>Euglena</i>	Predicted: PS bead
Actual: <i>Chlamydomonas</i>	0.831	0.005	0.163
Actual: <i>Euglena</i>	0.016	0.897	0.087
Actual: PS bead	\	\	\

Table 3-4 Confusion matrix of classifier using lensless images

Class	Predicted: <i>Chlamydomonas</i>	Predicted: <i>Euglena</i>	Predicted: PS bead
Actual: <i>Chlamydomonas</i>	0.817	0.028	0.155
Actual: <i>Euglena</i>	0.043	0.924	0.033
Actual: PS bead	0.040	0.022	0.937

3.3.2 Particle Counting

The imaging flow cytometer was tested with four *Chlamydomonas* samples with different dilution ratios (Sample #3 to Sample #6). Fig. 3-7 shows the automated counting results response to the *Chlamydomonas* concentration. The dotted line shows a result of liner fitting and its correlation coefficient is 0.9835. These results demonstrate the efficiency of automate particles counting with detection and tracking algorithms. The obtained error bars were larger than the theoretical detection of limits since the imaging flow cytometer should be able to detect single particle in the samples. There are two reasons to explain large error

bars: (i) the actual cell counts in every 150ul samples could be different. (ii) the detection and tracking algorithms are not optimized and tuned well yet.

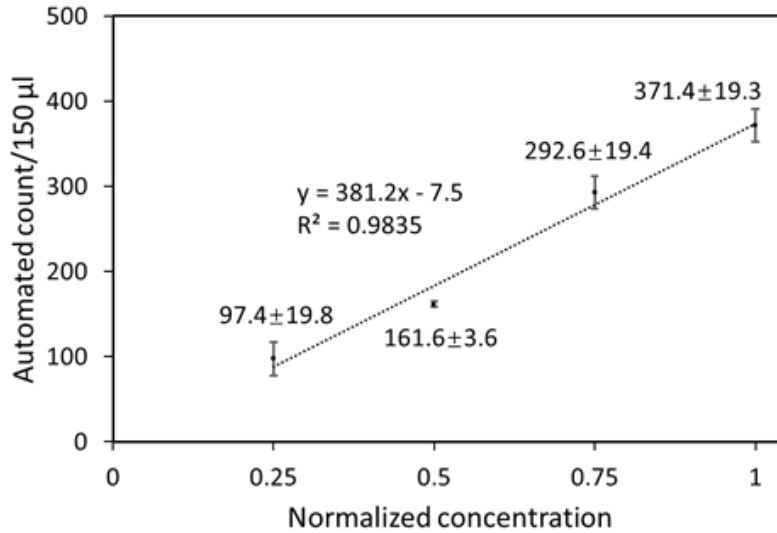


Figure 3-7. The *Chlamydomonas* count per 150 ul in the four samples. The ratio of *Chlamydomonas* concentration among sample #4, #5, #3, and #6 are 1:2:3:4. The error bar is estimated using standard deviation (SD) among 5 trials at each point. Each trial took 3 min as 150 ul water sample flow through the water channel.

The imaging flow cytometer was tested with three mixed samples to demonstrate its efficiency in detecting and counting specific cells. The sample #7 contained *Chlamydomonas* and *Euglena*. The concentration of *Euglena* in sample #8 was doubled compared with that in the sample #7. In sample #9, the concentration of *Chlamydomonas* and *Euglena* were same with that in the sample #7, while additional PS beads were added. The automated counting results of these mixed samples are shown and compared in Fig. 8. A baseline is measured with Sample #7 for comparison purposes. Note that detected non-fluorescent particles are contamination in the sample #7. Fig. 8 (a) shows the doubling of *Euglena* concentration (182.6 ± 24.9 vs. 106.7 ± 11.2) was correctly detected and counted. Fig. 8 (b) shows that both *Chlamydomonas* concentration (52.1 ± 9.2 vs. 63.4 ± 13.5) and *Euglena* concentration (111.7 ± 15.0 vs. 106.7 ± 11.2) are correctly

detected and counted when additional PS beads were presented. It also shows non-fluorescent PS beads were detected and counted. These results demonstrate that dual modality system can detect and count phytoplankton cells (*Chlamydomonas* and *Euglena*) when these two species and non-fluorescent particles are mixed in a sample.

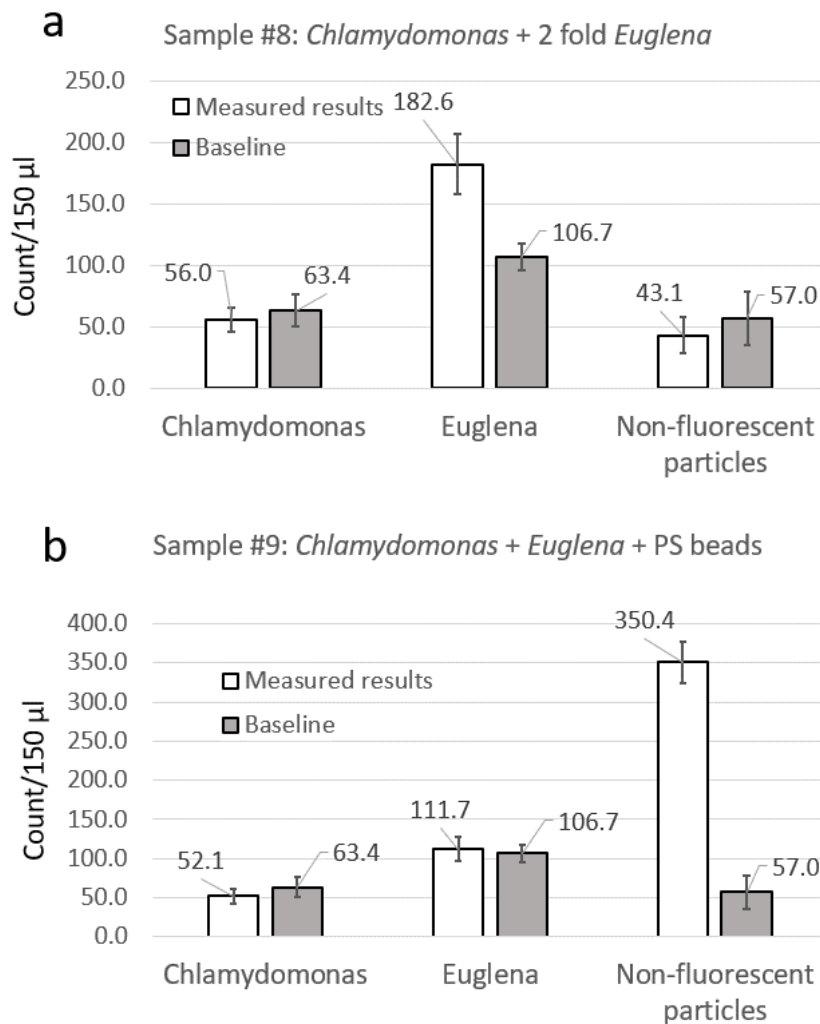


Figure 3-8. The measurement results of mix samples. Baseline is measured with Sample #7 for comparison purposes. Measured results of sample #8 and sample #9 were shown in (a) and (b) respectively. The error bar is estimated using standard deviation (SD) among 5 trails at each point. Each trail takes 3 min as 150ul water sample flow through the water channel.

3.4 Discussion

3.4.1 Performance of Fluorescence Camera

The fluorescence imaging mode relayed on a compact camera with a built-in lens and a fixed aperture of $f/2.8$. Although its spatial resolution does not match up with that of benchtop microscopes, this fluorescence camera has a long DoF and a capability of detecting *Chlamydomonas* cells. To demonstrate this, a few *Chlamydomonas* cells were imaged multiple times as the height offset of image plane was varied from -1 mm to 0.6 mm. *Chlamydomonas* cells can be detected using fluorescence camera even if these cells are off-focus, as shown in the Fig. 3-9 (b, c, e). However, their morphology features are hard to obtain because the observed *Chlamydomonas* cells are blurred and have varied sizes in response to height offset. The radius of observed *Chlamydomonas* cells was calculated and shown in Fig. 3-9(a). These results indicate that the fluorescence camera can detect the fluorescence signals generated by *Chlamydomonas* cells with a DoF of more than 0.8 mm. The large DoF can provide two advantages: (i) higher volumetric throughput since thick fluid channel can be applied (ii) better resistance to the unintended focus change. Since the morphology features can be obtained in the lensless imaging mode, the identification of particles is less affected by the poor spatial resolution of fluorescence camera.

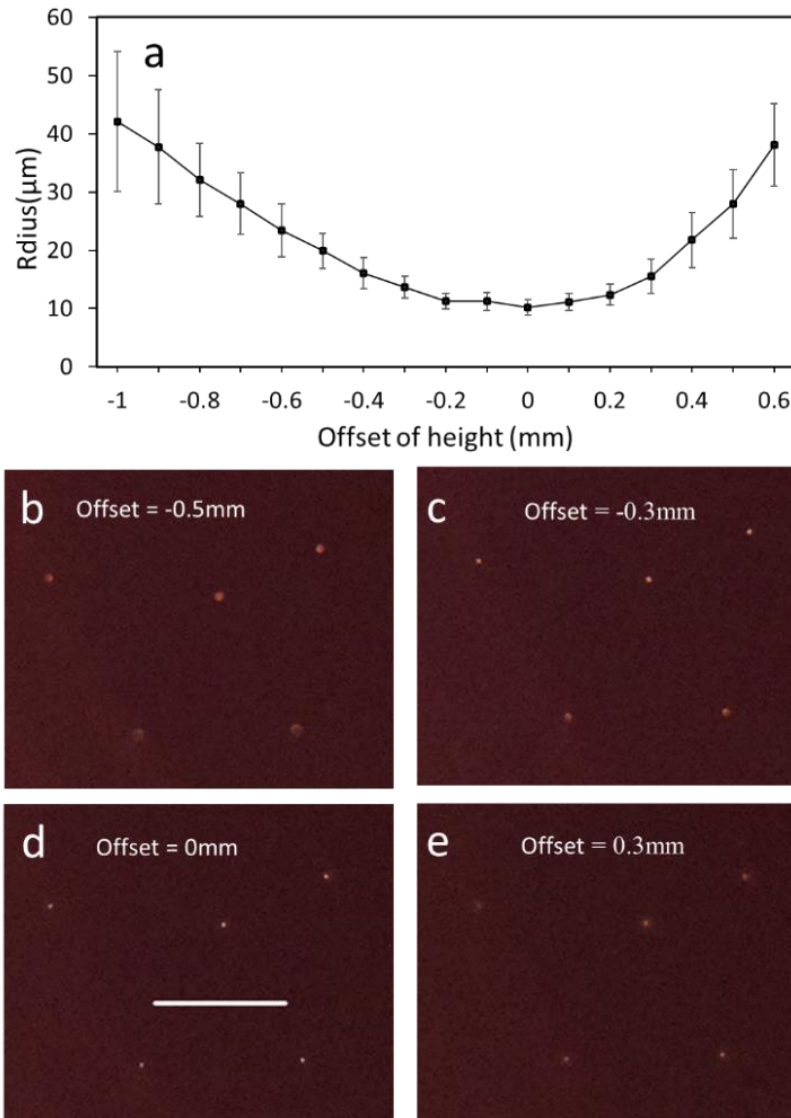


Figure 3-8. (a) The radius of observed *Chlamydomonas* cells in response to the offset of image plane. The plane with 0 offset is determined by the focus plane where radius of observed *Chlamydomonas* cells is minimum. The radius is defined as the distance between the peak value and 10% value. (b-e) shows the fluorescence images captured at offsets of -0.5 mm, -0.3 mm, 0 mm, 0.3mm. The Scale bar is 500 μm .

3.4.2 Volumetric Throughput

The volumetric throughput of this imaging flow cytometer platform is determined by several factors, including FoV, DoF, camera frame rate, and sensitivity of image sensor (ISO). Compared with traditional microscopes, the proposed dual-modality imaging approach offers advantages of large FoV and large DoF. In the current platform, the volumetric throughput is limited by the performance of low-cost cameras. The frame rate of Pi camera is low, leading to errors in particles tracking and counting when flow rate is high. Moreover, the sensitivity of image sensor is low. Therefore, fluorescence imaging requires long exposure time, resulting in motion blurring when particles move fast. Since the camera technologies are evolving rapidly, mostly benefiting from the mobile device market, these limitations of low-cost cameras could be overcome in the future.

3.4.3 Analysis of Natural Water

Natural water samples were manually collected from Lake Ontario (Bayfront Park, Hamilton, Ontario), followed by observation using the dual-modality imaging system. Some suspended particles that could be phytoplankton cells or colonies were detected by the dual-modality imaging system. Fig. 3-10 shows three particles found in the natural water samples. Their fluorescence features can be observed in the fluorescence mode. Their morphology features can be observed in the raw images captured in the lensless mode as well as the holographic reconstructed images. Classifiers that take advantages of morphology and fluorescence features can be trained for phytoplankton identification of natural water samples in the future. The video encoder on the Raspberry Pi deteriorated interference patterns in the raw holograms, reducing the quality of reconstructed images. Thus, the presented imaging processing algorithms still use morphology features extracted from raw holograms by HOG. Advance hardware and algorithms could be used to assist holographic reconstruction, improving morphology analysis

in the future.

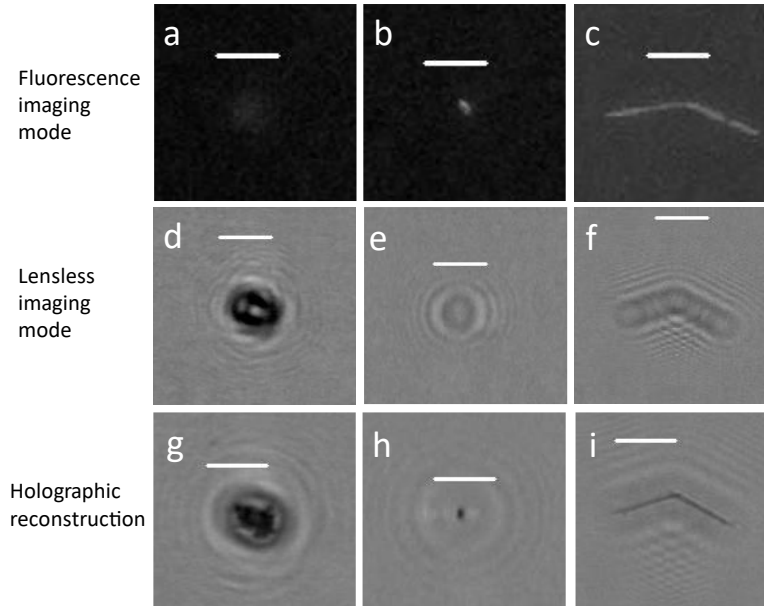


Figure 3-10. Images captured using natural water. (a-c) are captured in the fluorescence mode. (d-f) are captured in the lensless mode. (g-i) are holographic reconstruction results of (d-f). We believe these three particles are phytoplankton since they are autofluorescent. Scale bar is 100 μm .

3.5 Conclusion

We present a dual-modality imaging optofluidic cytometer for onsite phytoplankton monitoring. Morphology features of particles are acquired in the lensless imaging mode; Autofluorescence features of particles are acquired in the fluorescence imaging mode. The dual-modality imaging approach enabled observing both morphology and fluorescence features in a thick fluidic channel (0.33 mm) which contributes to high-throughput analysis. Experiments with *Chlamydomonas*, *Euglena*, 10 μm PS beads, and mixed samples have been performed to demonstrate the efficiency of particle counting and cellular-level classification. The cost-effectiveness and compactness of this design make it promising approach for onsite water monitoring.

Conflicts of interest

The authors declare no conflict of interests.

Acknowledgements

This project is supported in part by the Natural Science and Engineering Research Council (NSERC) of Canada, the Province of Ontario through an Ontario Research Fund (ORF-RE). QF held the Canada Research Chair in Biophotonics. BX holds a Chinese Scholarship Council PhD scholarship.

References

- [1] Field CB, Behrenfeld MJ, Randerson JT, Falkowski P. Primary production of the biosphere: integrating terrestrial and oceanic components. *Science*. 1998 Jul 10;281(5374):237-40.
- [2] Carpenter SR, Kitchell JF, Hodgson JR, Cochran PA, Elser JJ, Elser MM, Lodge DM, Kretchmer D, He X, von Ende C. Regulation of lake primary productivity by food web structure. *Ecology*. 1987 Dec;68(6):1863-76.
- [3] Benincà E, Huisman J, Heerkloss R, Jöhnk KD, Branco P, Van Nes EH, Scheffer M, Ellner SP. Chaos in a long-term experiment with a plankton community. *Nature*. 2008 Feb;451(7180):822-5.
- [4] Sahoo D, Seckbach J, editors. *The algae world*. Dordrecht: Springer; 2015 Dec 16.
- [5] Grattan LM, Holobaugh S, Morris Jr JG. Harmful algal blooms and public health. *Harmful algae*. 2016 Jul 1;57:2-8.
- [6] Hallegraeff GM. A review of harmful algal blooms and their apparent global increase. *Phycologia*. 1993 Mar 1;32(2):79-99.
- [7] Gallardo-Rodríguez JJ, Astuya-Villalón A, Llanos-Rivera A, Avello-Fontalba V, Ulloa-Jofré V. A critical review on control methods for harmful algal blooms. *Reviews in Aquaculture*. 2019 Aug;11(3):661-84.

- [8] Martin JL, Hanke AR, LeGresley MM. Long term phytoplankton monitoring, including harmful algal blooms, in the Bay of Fundy, eastern Canada. *Journal of Sea Research*. 2009 Jan 1;61(1-2):76-83.
- [9] Lee JH, Hodgkiss IJ, Wong KT, Lam IH. Real time observations of coastal algal blooms by an early warning system. *Estuarine, Coastal and Shelf Science*. 2005 Oct 1;65(1-2):172-90.
- [10] Lomax AS, Corso W, Etno JF. Employing unmanned aerial vehicles (UAVs) as an element of the Integrated Ocean Observing System. In *Proceedings of OCEANS 2005 MTS/IEEE 2005 Sep 17* (pp. 184-190). IEEE.
- [11] Coltelli P, Barsanti L, Evangelista V, Frassanito AM, Gualtieri P. Water monitoring: automated and real time identification and classification of algae using digital microscopy. *Environmental Science: Processes & Impacts*. 2014;16(11):2656-65.
- [12] Wilde EW, Fliermans CB. Fluorescence microscopy for algal studies. *Transactions of the American Microscopical Society*. 1979 Jan 1:96-102.
- [13] Beutler M, Wiltshire KH, Meyer B, Moldaenke C, Lüring C, Meyerhöfer M, Hansen UP, Dau H. A fluorometric method for the differentiation of algal populations in vivo and in situ. *Photosynthesis research*. 2002 Apr 1;72(1):39-53.
- [14] Izydorczyk K, Carpentier C, Mrówczyński J, Wagenvoort A, Jurczak T, Tarczyńska M. Establishment of an Alert Level Framework for cyanobacteria in drinking water resources by using the Algae Online Analyser for monitoring cyanobacterial chlorophyll a. *Water Research*. 2009 Mar 1;43(4):989-96.
- [15] Shin YH, Barnett JZ, Gutierrez-Wing MT, Rusch KA, Choi JW. A hand-held fluorescent sensor platform for selectively estimating green algae and cyanobacteria biomass. *Sensors and Actuators B: Chemical*. 2018 Jun 1;262:938-46.
- [16] Wert EC, Dong MM, Rosario-Ortiz FL. Using digital flow cytometry to assess the degradation of three cyanobacteria species after oxidation processes. *Water research*. 2013 Jul 1;47(11):3752-61.

- [17] Wu J, Li J, Chan RK. A light sheet based high throughput 3D-imaging flow cytometer for phytoplankton analysis. *Optics express*. 2013 Jun 17;21(12):14474-80.
- [18] Park J, Kim Y, Kim M, Lee WH. A novel method for cell counting of *Microcystis* colonies in water resources using a digital imaging flow cytometer and microscope. *Environmental Engineering Research*. 2019;24(3):397-403.
- [19] Rutten TP, Sandee B, Hofman AR. Phytoplankton monitoring by high performance flow cytometry: a successful approach?. *Cytometry Part A: The Journal of the International Society for Analytical Cytology*. 2005 Mar;64(1):16-26.
- [20] Han Y, Gu Y, Zhang AC, Lo YH. Imaging technologies for flow cytometry. *Lab on a Chip*. 2016;16(24):4639-47.
- [21] Dashkova V, Malashenkov D, Poulton N, Vorobjev I, Barteneva NS. Imaging flow cytometry for phytoplankton analysis. *Methods*. 2017 Jan 1;112:188-200.
- [22] Olson RJ, Sosik HM. A submersible imaging-in-flow instrument to analyze nano-and microplankton: Imaging FlowCytobot. *Limnology and Oceanography: Methods*. 2007 Jun;5(6):195-203.
- [23] Ozcan A, McLeod E. Lensless imaging and sensing. *Annual review of biomedical engineering*. 2016 Jul 11;18:77-102.
- [24] Roy M, Seo D, Oh S, Yang JW, Seo S. A review of recent progress in lens-free imaging and sensing. *Biosensors and Bioelectronics*. 2017 Feb 15;88:130-43.
- [25] Seo S, Su TW, Tseng DK, Erlinger A, Ozcan A. Lensfree holographic imaging for on-chip cytometry and diagnostics. *Lab on a Chip*. 2009;9(6):777-87.
- [26] Mudanyali O, Bishara W, Ozcan A. Lensfree super-resolution holographic microscopy using wetting films on a chip. *Optics express*. 2011 Aug 29;19(18):17378-89.
- [27] Merola F, Memmolo P, Bianco V, Paturzo M, Mazzocchi MG, Ferraro P. Searching and identifying microplastics in marine environment by digital holography*. *The European Physical Journal Plus*. 2018 Sep 1;133(9):350.

- [28] Kun J, Smieja M, Xiong B, Soleymani L, Fang Q. The Use of Motion Analysis as Particle Biomarkers in Lensless Optofluidic Projection Imaging for Point of Care Urine Analysis. *Scientific reports*. 2019 Nov 21;9(1):1-2.
- [29] Mahoney E, Kun J, Smieja M, Fang Q. Point-of-care urinalysis with emerging sensing and imaging technologies. *Journal of The Electrochemical Society*. 2019 Dec 11;167(3):037518.
- [30] Fang Y, Yu N, Wang R, Su D. An on-chip instrument for white blood cells classification based on a lens-less shadow imaging technique. *PloS one*. 2017 Mar 28;12(3):e0174580.
- [31] Göröcs Z, Tamamitsu M, Bianco V, Wolf P, Roy S, Shindo K, Yanny K, Wu Y, Koydemir HC, Rivenson Y, Ozcan A. A deep learning-enabled portable imaging flow cytometer for cost-effective, high-throughput, and label-free analysis of natural water samples. *Light: Science & Applications*. 2018 Sep 19;7(1):1-2.
- [32] Boddy L, Morris CW, Wilkins MF, Al-Haddad L, Tarran GA, Jonker RR, Burkill PH. Identification of 72 phytoplankton species by radial basis function neural network analysis of flow cytometric data. *Marine Ecology Progress Series*. 2000 Mar 31;195:47-59.
- [33] Coskun AF, Su TW, Ozcan A. Wide field-of-view lens-free fluorescent imaging on a chip. *Lab on a Chip*. 2010;10(7):824-7.
- [34] Shanmugam A, Salthouse CD. Lensless fluorescence imaging with height calculation. *Journal of Biomedical Optics*. 2014 Jan;19(1):016002.
- [35] Paiè P, Martínez Vázquez R, Osellame R, Bragheri F, Bassi A. Microfluidic based optical microscopes on chip. *Cytometry Part A*. 2018 Oct;93(10):987-96.
- [36] Pang S, Han C, Lee LM, Yang C. Fluorescence microscopy imaging with a Fresnel zone plate array based optofluidic microscope. *Lab on a Chip*. 2011;11(21):3698-702.
- [37] French CS, Young VK. The fluorescence spectra of red algae and the transfer of energy from phycoerythrin to phycocyanin and chlorophyll. *The Journal of general physiology*. 1952 Jul 20;35(6):873-90.

- [38] Dadi HS, Pillutla GM. Improved face recognition rate using HOG features and SVM classifier. IOSR Journal of Electronics and Communication Engineering. 2016 Apr;11(04):34-44.
- [39] Kristan M, Leonardis A, Matas J, Felsberg M, Pflugfelder R, ˇCehovin Zajc L, Vojir T, Bhat G, Lukezic A, Eldesokey A, Fernandez G. The sixth visual object tracking vot2018 challenge results. In Proceedings of the European Conference on Computer Vision (ECCV) Workshops 2018.
- [40] Latychevskaia T, Fink HW. Practical algorithms for simulation and reconstruction of digital in-line holograms. Applied optics. 2015 Mar 20;54(9):2424-34.

Chapter 4.

Paper III - Luminescence lifetime imaging using cellphone camera with electronic rolling shutter

Bo Xiong¹, Qiyin Fang^{1,2,*}

¹School of Biomedical Engineering, McMaster University, Ontario, L8S 4L8, Canada

²Department of Engineering Physics, McMaster University, Ontario, L8S 4L8, Canada

Published in Optics Letters; 45(1): 81-84, 2020

Printed with permission

doi: 10.1364/OL.45.000081

Introduction to the Paper III:

Fluorescent lifetime imaging (FLIM) is a powerful technique for biological and chemical analysis, which are commonly required in water quality monitoring. However, current FLIM system are typically complex and expensive instruments targeting bench-top applications. This chapter develops a portable and low-cost FLIM approach which is suitable for onsite monitoring.

In this work, FLIM was realized by a cellphone camera with an electronic rolling shutter when a sample was illuminated with modulated excitation light. The fluorescent lifetime is measured by analyzing the optical fringes captured by the low-cost and portable camera with the frequency domain method. This FLIM approach is demonstrated by mapping a dissolved oxygen sensitive film with a varied emission lifetime. This work provided an approach that allows integrating the FLIM modules in portable and low-cost optofluidic platforms.

My contributions of this work include proposing the FLIM approach, developing experimental setups, performing the experiments, analyzing the results, and writing the manuscript.

Contents of Paper III

Abstract

Luminescence lifetime imaging systems are typically complex and expensive instruments targeting bench-top applications. We present a low-cost approach for video frame rate luminescence lifetime imaging on the microsecond scale based on a cellphone camera. The luminescence lifetime is mapped by measuring the phase shift of optical fringes captured by a camera with an electronic rolling shutter at 30 frames per second. Luminescence lifetime imaging is validated by observing a PtTFPP/polystyrene film with a non-uniform lifetime distribution. Experimental results indicate a lifetime resolution of 580 ns when a lifetime of 22 s is measured. This device is portable, low-cost, and shows the potential in point-of-care diagnostic and environment applications that measure long lifetime luminescence.

4.1 Introduction

Luminescence lifetime imaging is an emerging technique that measures emission decay rate from fluorophore, phosphors, or any other luminescent probe. It has been explored in biomedical [1,2] and environmental applications [3,4]. Particularly, recent advances in the development of long-lifetime ($> 1\mu\text{s}$) luminescent probes such as, transition-metal complexes [5,6], lanthanide chelates [7,8] and up-conversion nanoparticles [9,10] and their applications are driving factors in long (microseconds to milliseconds) lifetime imaging technologies.

Time-gated sampling and Time-Correlated Single Photon Counting (TCSPC) are common lifetime imaging techniques. In the time-gated sampling method, a camera with a fast, global shutter (“time-gate”) is synchronized with light

sources and repetitively samples the luminescence decay [11,12]. In TCSPC, the emission is collected one photon at a time to build a histogram in the time-domain to retrieve lifetime, then raster scanning in the spatial domain to form a time-resolved image [13,14]. Both techniques are complex, expensive, and generally used in bench-top research settings [15-17]. Low-cost and miniaturized complementary metal–oxide–semiconductor (CMOS) imagers are widely used in the mobile devices with an electronic rolling shutter (ERS). In ERS, each line of pixels has the same exposure time in each frame, but the exposure of each line occurs at different times [18,19]. An ERS in cellphones can typically scan more than 100,000 lines per second [20]. As a result, the rolling line-by-line exposure may be an alternative to time-gated sampling method to achieve luminescence lifetime imaging.

Here we report a low-cost luminescence lifetime imaging device based on a cellphone CMOS imager with an ERS. The luminescence lifetime imaging is validated by mapping interaction of oxygen and an oxygen sensitive luminescent film. This device is portable, low-cost and shows the potential in point-of-care and applications that require portable devices.

4.2 Materials and Methods

The schematic of the proposed luminescence lifetime imaging device is shown in Fig. 4-1(a). A microcontroller (Uno, Arduino) sends TTL signals (4 kHz and 35% duty cycle) to modulate a 405 nm diode laser (405 LD, Wuhan Besram Technology, Wuhan, China). A luminescent sample is placed on a stainless-steel holder which hardly emit auto fluorescence. The laser excites the sample, shown in Fig. 4-1(c), and both the reflected/scattered excitation light and emission light are collected by the camera. A long pass emission filter (WRATTEN No. 29, $\lambda > 590\text{nm}$, Eastman Kodak, Rochester, NY) is held on a 3D printed mount in front of the camera aperture. As shown in Fig. 4-1(b) and Fig. 4-1(c), the emission filter is

placed 1 cm away from cellphone and covers 70% of the field of view (FoV). As shown in Fig. 4-1(d), the camera FoV is split into two regions by the emission filter: the sample area and the reference area. The reflection/back scattering of the excitation beam can reach the reference area, while the luminescence image can be measured in the sample area. The whole device can be packaged in a small box, as shown in Fig. 4-1(a). The total cost of main modules, i.e., microcontroller, laser, emission filter and mounting are less than \$50 USD. In this setup, a cellphone with a Sony IMX315 camera (3840 x 2160 at 30 frames per second/fps) was used to acquire the images and perform image processing at a maximum 64.8k lines/s rolling shutter. The cellphone camera is manually controlled by 'Moment', which is an IOS application bought from iPhone App store. In practice, a stand-alone camera module, such as the Raspberry Pi Camera can be used along with a Raspberry Pi computing platform: putting the total lifetime imaging system hardware cost below \$100.

A 25 mm round coverslip was coated by PtTFPP (Platinum(II)-5,10,15,20-tetrakis-(2,3,4,5,6- pentafluorphenyl)-porphyrin, CAS 109781-47-7, Sigma Aldrich)/polystyrene (CAS 9003-53-6, Sigma Aldrich) film to demonstrate luminescence lifetime imaging. PtTFPP shall generate emission light with a peak of 650nm.

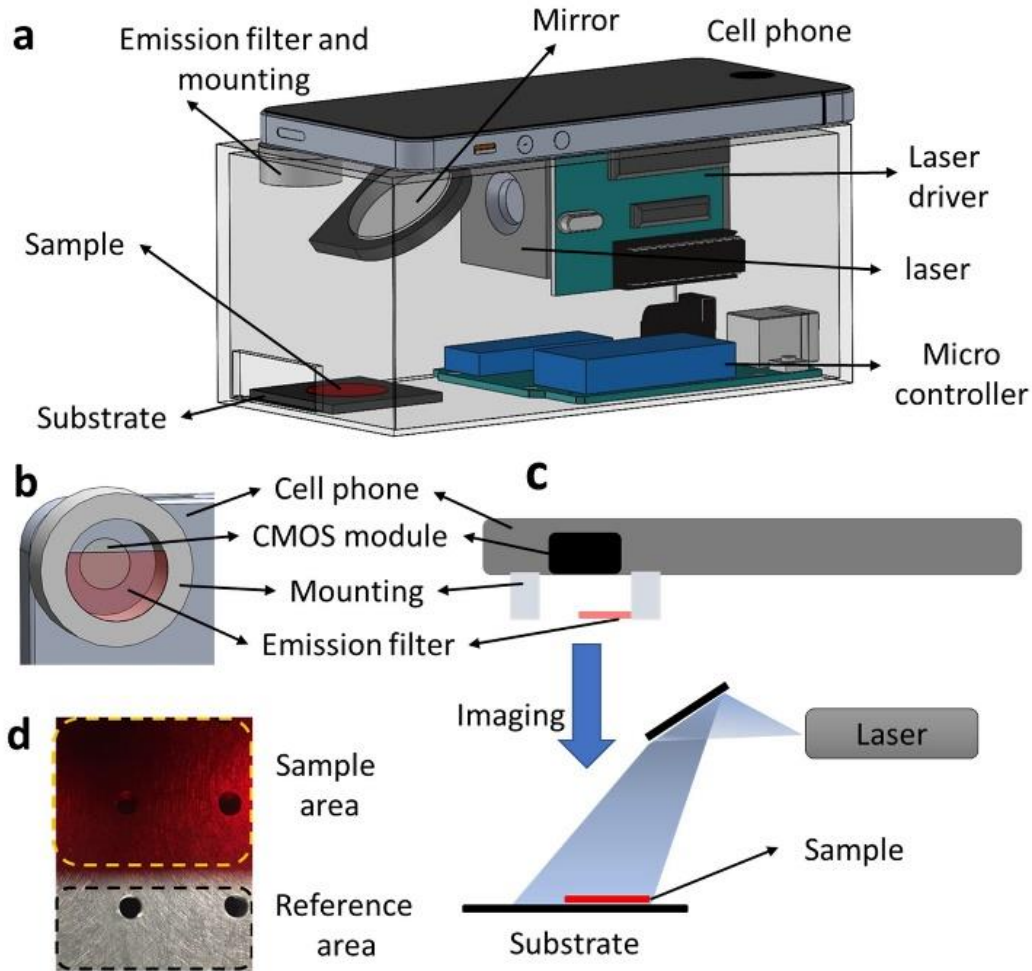


Figure 4-1. Conceptual design of the fluorescence lifetime imager. (a) Schematic of 3D System design. (b) Emission filter and a 3D printed mount on the cellphone. (c) Schematic of the optical path. Excitation light covers both sample and a part of substrate. The red line on top of the substrate indicates the sample area, whose emission will pass the emission filter. (d) Camera's view without a sample, illuminated by a white light source.

In the rolling shutter-based cameras, each line of pixels is activated sequentially. When the modulation frequency of the excitation light is higher than the frame rate of video, optical fringes can be observed in one image frame due to the rolling shutter effect [18][19]. In our experiment, an intensity image is captured with exposure time of 91 s, as shown in Fig. 4-2(a). The rolling shutter scans each line of pixels from left to right, therefore, vertical optical fringes are observed. And

luminescence lifetime images can be calculated using these optical fringes. First, the whole image is split into an array of sub-images, as shown in Fig. 4-2(c). A sub-image in the reference area and a sub-image in the sample area are labeled by a blue square and a red square respectively, as shown in the Fig. 4-2(b). Since these two sub-images are in the same column, they should be captured at same time. Fig. 4-2(d) shows the fringes profiles in the two labeled sub-images. And optical fringes in the red square labeled sub-image is shift towards right side compared with the fringes in the blue square labeled sub image due to the delay of luminescent emission. Second, the dominated sinusoid component of fringe profiles, which corresponds to excitation modulation, is decomposed using fast Fourier transform (FFT) in each sub-image. Then the phase of optical fringes in each sub-image can be obtained using Eq. (4.1).

$$\angle X = \tan^{-1} \left(\frac{X_{im}}{X_{re}} \right) \quad (4.1)$$

Where $\angle X$ is the phase of the dominated sinusoid component, and X_{im} and X_{re} are the corresponding imaginary and real components of the FFT results. The fringes could be distorted in some sub-images due to non-uniform emission/excitation intensity, leading to an error on the observed $\angle X$. This effect is more significant in a single frame, and it can be reduced over multiple averaged frames. The phase of two labeled sub-images are shown in Fig. 4-2(e). Third, the luminescence lifetime τ in the sample area can be obtained using the frequency domain method [21], as shown in Eq. (4.2):

$$\phi(f) = \tan^{-1}(2\pi f\tau) \quad (4.2)$$

Where f is modulation frequency, $\phi(f)$ is phase shift. The phase shift can be obtained by subtracting the sample sub-image's phase from the corresponding reference phase of sub-image which is aligned in same column in the array.

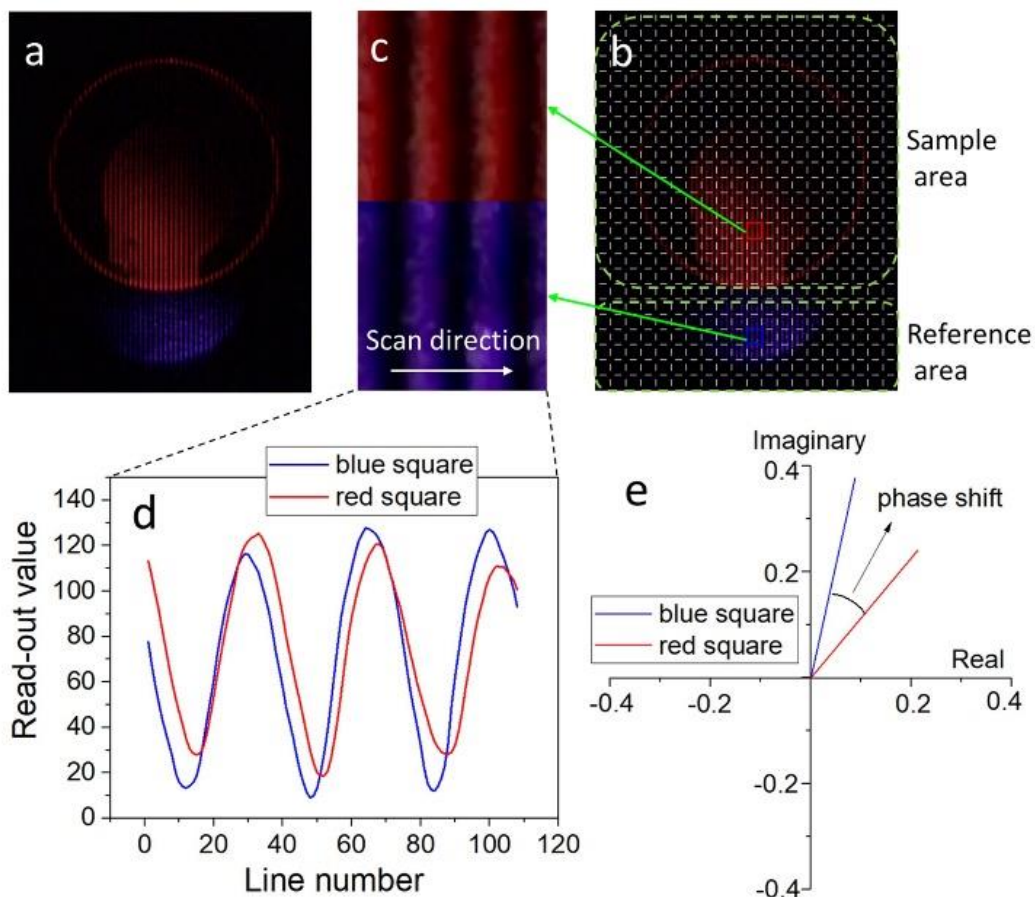


Figure 4-2. Luminescence lifetime calculation in the captured images. (a) An image captured by a cellphone camera. (b) The image is split into sub-images. A sub-image in the reference area is labeled by a blue square. A sub-image in the sample area is labeled by a red square. (c) The details of two labeled sub-images. (d) The fringes profiles in two labeled sub-images. (e) Vectors corresponding to the dominated sinusoid components of fringe profiles are obtained from the complex numbers of FFT results. Two vectors obtained from two labeled sub-images are shown. Phase shift can be obtained as shown.

4.3 Results and Discussion

The luminescence lifetime imaging is validated by mapping the interaction of PtTFPP and oxygen, where PtTFPP luminescence lifetime can be reduced in the presence of oxygen in the polystyrene film due to collisional quenching [6]. Measurements were taken for a duration of 60 seconds. At the 23rd second, a

droplet of 2% sodium sulfate solution was placed on the PtTFPP/polystyrene film. There is no dissolved oxygen in the solution since oxygen is consumed by sodium sulfate. As a result, the luminescence lifetime of PtTFPP/polystyrene film should increase once the film is in contact with the sodium sulfate solution due to oxygen diffusion. The camera recorded a video (2700x2160 pixels) for 60 seconds at 30 fps (See Supplementary Visualization 1). The luminescence lifetime images were calculated from every frame, then averaging all 30 frames in each second. A frame obtained after droplet placed is shown in the Fig. 4-3(b). Three sub-images, which refer to reference area, sample area with oxygen and sample area without oxygen, are labeled by a blue square, red square and green square respectively. Fig. 4-3(c) and Fig. 4-3(d) show the measured lifetime images before and after droplet placed respectively. In the center of coverslip where droplet placed, the lifetime of green square labeled sub-image increased from 24.2 μs to 66.8 μs . On the other hand, the red square labeled sub-image has a stable lifetime ($\sim 22 \mu\text{s}$). These results demonstrate that the proposed device can detect the luminescence lifetime variation on the PtTFPP film.

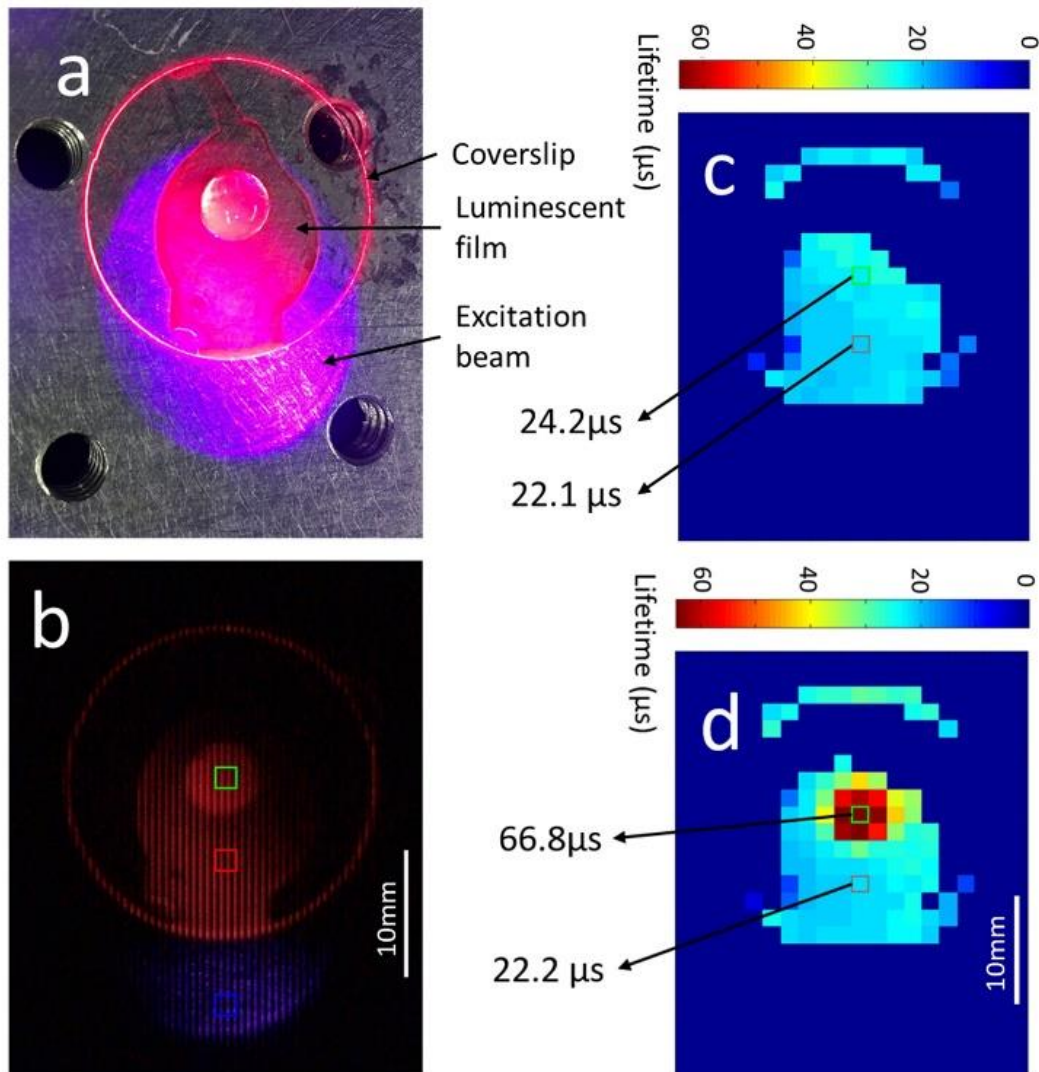


Figure 4-3. Measured luminescent lifetime images and raw images. (a) A picture of the coverslip captured by another camera without filter after the sodium sulfate solution dropped. (b) A frame captured after the sodium sulfate solution dropped. Three sub-images, which refer to the reference area, the sample area with oxygen and the sample area without oxygen, are labeled by a blue square, a red square and a green square respectively. (c, d) Measured luminescent lifetime images before and after the sodium sulfate solution dropped. The lifetime is set to zero where luminescent light is too weak.

As shown in Fig. 4-4, the measured lifetime in the center of the sample, which is labeled by green square in the Fig. 4-3(b), increases after 23 s due to the

placement of sodium sulfate droplet. On the other hand, the measured lifetime of the sub image on the film exposed to air, which is labeled by red square in the Fig. 4-3(b), is stable. Considering that the resolution of the lifetime measurement is estimated using 3 times of standard deviation of measured lifetime in the red square labelled sub image. A lifetime resolution of 580 ns is obtained from the averaged lifetime of 22.4 μ s with 60 sampling points. According to Equation (2), the accuracy of measured lifetime depends on the errors of modulation frequency f and errors of phase shift $\phi(f)$. The errors of f can be calibrated by measuring the modulation signal with a precise oscilloscope. Most of systematic errors of phase shift $\phi(f)$ can be eliminated in the proposed design, because it measures both luminescence signal and excitation (reference) signal with a CMOS camera at same time.

The spatial resolution of this design is determined by the resolution of the camera and the size of each sub image. Recent advances in CMOS technology have led to high pixel count cameras with very low cost. Since the FoV is split into a reference area and a sample area, this approach can only use a fraction (~70%) of the FoV of the camera, typically not a major issue in the targeted lifetime imaging applications.

There are two approaches can be used to improve the lifetime resolution of proposed technique: (i) using moving average with a larger number of time period (ii) using a camera with a faster rolling shutter. As shown in Fig. 4-4, random noise dominates the fluctuation of the measured lifetime in the red square labelled sub image. These noises can be reduced with a longer time period in moving average. Using a faster rolling shutter can increase the sampling rate as more lines of pixels are scanned per second. Although a line of pixel can be activated by ERS in a short time, reading and saving data from pixels require relative longer time which limits the rolling shutter speed in the CMOS imagers. The speed of rolling shutter in a commercial cellphone camera increased rapidly in the recent years. To our best knowledge, the cellphone camera can read-out up to 690k lines/ second by March

2019 [22] and it reaches 1382k lines/second by October 2019 [23]. Customized CMOS imagers can read out 2 million lines of pixels per seconds with advanced column-parallel ADCs and in the lab [24].

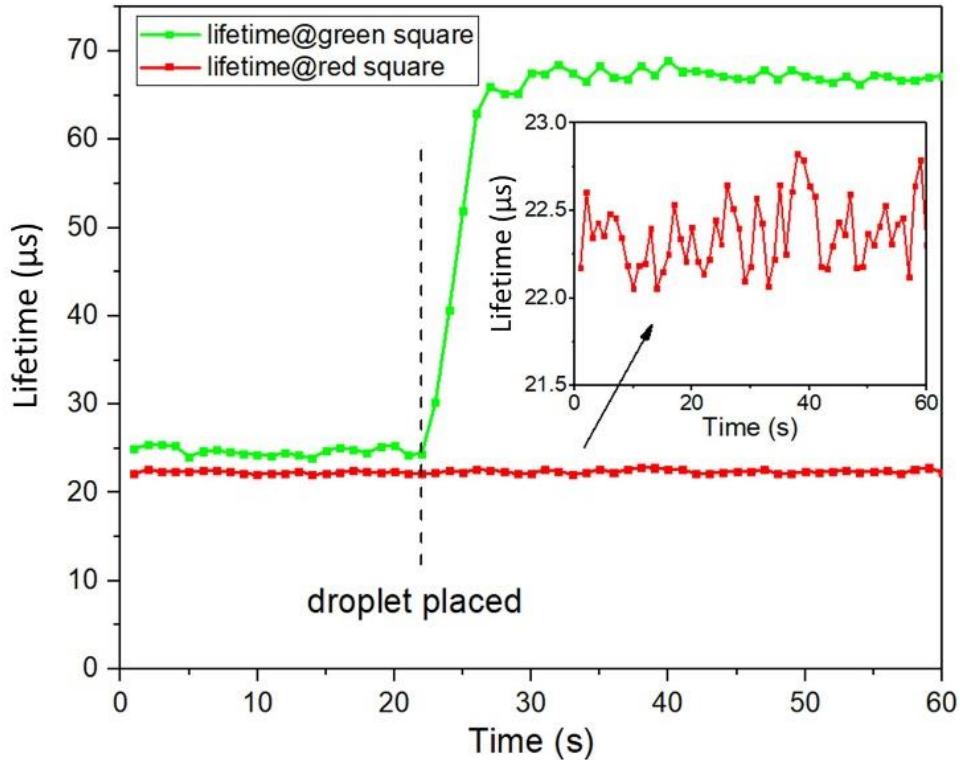


Figure 4-4. Measured luminescence lifetime curve of two sub-images. Green line refers to the sub-image labeled by a green square in Fig. 4-3(b). Red line refers to the sub image labeled by a red square in Fig. 4-3(b).

4.4 Conclusion

In summary, a low-cost luminescence lifetime imaging device using a cellphone with an ERS is developed. The luminescence lifetime is obtained from optical fringes, while, no additional electronic device required to make laser modulation and camera synchronized. The luminescence lifetime imaging is validated by mapping a PtTFPP/polystyrene film with a varied emission lifetime. A lifetime resolution of 580 ns is obtained at a sampling frequency of 1 Hz. These

results indicate that this device is suitable to measure emission lifetime in the microsecond or longer regime. The device could motivate the usage of long-lifetime luminescent probes in point-of-care diagnostic and environment applications where low-cost and portable devices are required.

Funding. Natural Science and Engineering Research Council (NSERC) of Canada; the Province of Ontario through an Ontario Research Fund-Research Excellence grant; and Canadian Foundation of Innovation.

Acknowledgment. B. Xiong acknowledge a PhD fellowship from the Chinese Scholarship Council.

Conflict of interest

The authors declare that they have no conflict of interest.

References

- [1] Becker W. Fluorescence lifetime imaging–techniques and applications. *Journal of microscopy*. 2012 Aug;247(2):119-36.
- [2] Zhang KY, Yu Q, Wei H, Liu S, Zhao Q, Huang W. Long-lived emissive probes for time-resolved photoluminescence bioimaging and biosensing. *Chemical reviews*. 2018 Feb 28;118(4):1770-839.
- [3] Liebsch G, Klimant I, Frank B, Holst G, Wolfbeis OS. Luminescence lifetime imaging of oxygen, pH, and carbon dioxide distribution using optical sensors. *Applied Spectroscopy*. 2000 Apr;54(4):548-59.
- [4] Jakobs S, Subramaniam V, Schönle A, Jovin TM, Hell SW. EGFP and DsRed expressing cultures of Escherichia coli imaged by confocal, two-photon and fluorescence lifetime microscopy. *FEBS letters*. 2000 Aug 18;479(3):131-5.

- [5] Zhang C, Liu M, Liu S, Yang H, Zhao Q, Liu Z, He W. Phosphorescence Lifetime Imaging of Labile Zn²⁺ in Mitochondria via a Phosphorescent Iridium (III) Complex. *Inorganic chemistry*. 2018 Aug 13;57(17):10625-32.
- [6] Mao Y, Gao Y, Wu S, Wu S, Shi J, Zhou B, Tian Y. Highly enhanced sensitivity of optical oxygen sensors using microstructured PtTFPP/PDMS-pillar arrays sensing layer. *Sensors and Actuators B: Chemical*. 2017 Nov 1;251:495-502.
- [7] Faulkner S, Pope SJ, Burton-Pye BP. Lanthanide complexes for luminescence imaging applications. *Applied Spectroscopy Reviews*. 2005 Jan 1;40(1):1-31.
- [8] Eliseeva SV, Bünzli JC. Lanthanide luminescence for functional materials and bio-sciences. *Chemical Society Reviews*. 2010;39(1):189-227.
- [9] Wen S, Zhou J, Zheng K, Bednarkiewicz A, Liu X, Jin D. Advances in highly doped upconversion nanoparticles. *Nature communications*. 2018 Jun 20;9(1):1-2.
- [10] Dong, Hao, et al. "Versatile spectral and lifetime multiplexing nanoplatform with excitation orthogonalized upconversion luminescence." *ACS nano* 11.3 (2017): 3289-3297. [11] Hirvonen, Liisa M., and Klaus Suhling. "Wide-field TCSPC: methods and applications." *Measurement Science and Technology* 28.1 (2016): 012003.
- [12] Hirvonen LM, Festy F, Suhling K. Wide-field time-correlated single-photon counting (TCSPC) lifetime microscopy with microsecond time resolution. *Optics letters*. 2014 Oct 1;39(19):5602-5.
- [13] Requejo-Isidro J, McGinty J, Munro I, Elson DS, Galletly NP, Lever MJ, Neil MA, Stamp GW, French PM, Kellett PA, Hares JD. High-speed wide-field time-gated endoscopic fluorescence-lifetime imaging. *Optics letters*. 2004 Oct 1;29(19):2249-51.
- [14] Dahan M, Laurence T, Pinaud F, Chemla DS, Alivisatos AP, Sauer M, Weiss S. Time-gated biological imaging by use of colloidal quantum dots. *Optics letters*. 2001 Jun 1;26(11):825-7.

- [15] Wei L, Yan W, Ho D. Recent advances in fluorescence lifetime analytical microsystems: Contact optics and CMOS time-resolved electronics. *Sensors*. 2017 Dec;17(12):2800.
- [16] Chelushkin PS, Tunik SP. Phosphorescence lifetime imaging (PLIM): State of the art and perspectives. *InProgress in Photon Science 2019* (pp. 109-128). Springer, Cham.
- [17]<https://www.picoquant.com/products/category/fluorescence-microscopes/microtime-200-time-resolved-confocal-fluorescence-microscope-with-unique-single-molecule-sensitivity> (accessed on Sep 2019).
- [18] Chow CW, Chen CY, Chen SH. Visible light communication using mobile-phone camera with data rate higher than frame rate. *Optics express*. 2015 Oct 5;23(20):26080-5.
- [19] Chow CW, Chen CY, Chen SH. Enhancement of signal performance in LED visible light communications using mobile phone camera. *IEEE Photonics Journal*. 2015 Oct;7(5):1-7.
- [20] <https://www.apple.com/ca/iphone-11/specs/> (accessed on Sep 2019).
- [21] Liu R, Zhao Z, Zou L, Fang Q, Chen L, Argento A, Lo JF. Compact, non-invasive frequency domain lifetime differentiation of collagens and elastin. *Sensors and Actuators B: Chemical*. 2015 Nov 1;219:283-93.
- [22] <https://www.samsung.com/global/galaxy/galaxy-s10/specs/> (accessed on Sep 2019).
- [23] <https://consumer.huawei.com/cn/phones/mate30-pro/specs/>(accessed on Nov 2019).
- [24] Yasue T, Tomioka K, Funatsu R, Nakamura T, Yamasaki T, Shimamoto H, Kosugi T, Jun SW, Watanabe T, Nagase M, Kitajima T. A 33Mpixel CMOS imager with multi-functional 3-stage pipeline ADC for 480fps high-speed mode and 120fps low-noise mode. *In2018 IEEE International Solid-State Circuits Conference-(ISSCC) 2018 Feb 11* (pp. 90-92). IEEE.

Chapter 5. Summary and Future Work

5.1 Discussion and Future Work

5.1.1 Fluorescence-based Optofluidic Platform

A fluorescence-based optofluidic platform with frequency domain TRF approach and prism assisted coupling is presented in **Chapter 2**. The precision of DO sensor was better than 0.19 ppm in a range of 0 – 13 ppm. The limit of detection was 0.10 ppm which is three times of SD of measured DO in the deoxygenated water sample. The sensing specificity could be evaluated with future experiments. The accuracy of natural water sensing could be affected by long-term degradation and cross-talking. More experiments could be performed when the sensors are deployed onsite. Although dissolved oxygen measurements have been conducted and the advantages of the existing platform have been demonstrated, there are still hurdles to pass before onsite deployment. The two main hurdles, which are sensing film improvements and device miniaturization, are addressed in the following paragraphs. Furthermore, future work on adapting the existing platform for alternative target analytes is discussed.

5.1.1.1 Sensing Film Improvement

The fluorophore functionalized sensing film is essential to sense sensitivity and stability. There are five main criteria to evaluate the usability of a sensing film in the existing platform, namely (i) brightness, (ii), sensitivity (iii) fluorescence lifetime, (iv) photostability, and (v) long-term degradation. These criteria and the methods for sensing film improvements are discussed.

- (i) Brightness refers the intensity of the total fluorescent light emitted from a sensing film under a specific excitation light source. A brighter film shall

increase the SNR of photoelectric signals, leading to a better limit of detection. The brightness depends on main three factors: (a) molar extinction coefficient, (b) quantum efficiency and (c) the quantity of fluorophores in the film. Hence, fluorophores with high extinction coefficient and quantum efficiency are preferred in the sensing film [1][2], such as PtTFPP. The quantity of fluorophores can be increased by using high fluorophore concentration during chip fabrication. However, high fluorophore concentration can prevent the forming of sensing film. Therefore, more experiments should be conducted to find the optimized fluorophore and solvent concentration.

- (ii) Sensitivity is defined as the ratio of reduction of fluorescence intensity/lifetime to the original fluorescence intensity/lifetime when dissolved oxygen is present in the fluidic sample. The fluorescence sensing can be deteriorated when the sensitivity is too high or too low. Under an extremely high sensitivity, the fluorescent intensity shall be too weak to be detected in the presence of dissolved oxygen; under an extremely low sensitivity, the change of fluorescent intensity/lifetime can hardly be detected. According to the Stern-Volmer equation, the sensitivity depends on two factors: the quenching constant and the quencher concentration in the film at equilibrium. The quenching constant depends on the intrinsic properties of the fluorophore and matrix [3]. Quencher concentration in the sensing film at equilibrium depends on gas permeability of film's matrix [3]. Therefore, both the fluorophore and matrix should be selected carefully to realize a desirable sensitivity.
- (iii) Fluorescence lifetime is the time duration for the fluorophore to return from the excited state to the ground state. The fluorophores with a long lifetime are desired in the TRF-based sensing platforms since long lifetime reduce dependence on expensive and bulky devices, such as high-frequency light

sources, fast-response detectors and data acquisition modules with a high sampling rate.

- (iv) Photostability of sensing film depends on photostability and film degradation effects. Photostability refers an ability of fluorophore to resist photobleaching. Photobleaching can results in a reduction of emission intensity, deteriorating the precision of both TRF and static measurements [4]. Thus, fluorophores with good photostability are desired for onsite monitoring applications where long sensing operation lifetime are required.
- (v) Film degradation could be caused by biofouling and matrix aging. Biofouling is the accumulation of microorganisms, plants, algae, blocking light path and generating unintended background fluorescence signals. Thus, filtration and anti-fouling coating could be applied in the sensor to combat with biofouling. Matrix aging could change the gas permeability and diffusivity, inducing a time drift in long-term monitoring applications.

5.1.1.2 Miniaturization

Device miniaturization is necessary before deploying the fluorescence-based optofluidic platform in the field. Electronic components, such as the data acquisition module and the wave generator, should be replaced by miniaturized devices. Furthermore, the coupling of emission light can be improved for device miniaturization. Thanks to TIR design and prism assisted coupling, most of excitation lights are confined in the sensing film and does not reach the emission filter. Thus, the background noise caused by residual excitation light that is common in the other compact optical designs can be mitigated. This allows integration of the detector, emission filter and microfluidic channel on a chip or in a compact device, as shown in **Figure 5-1**.

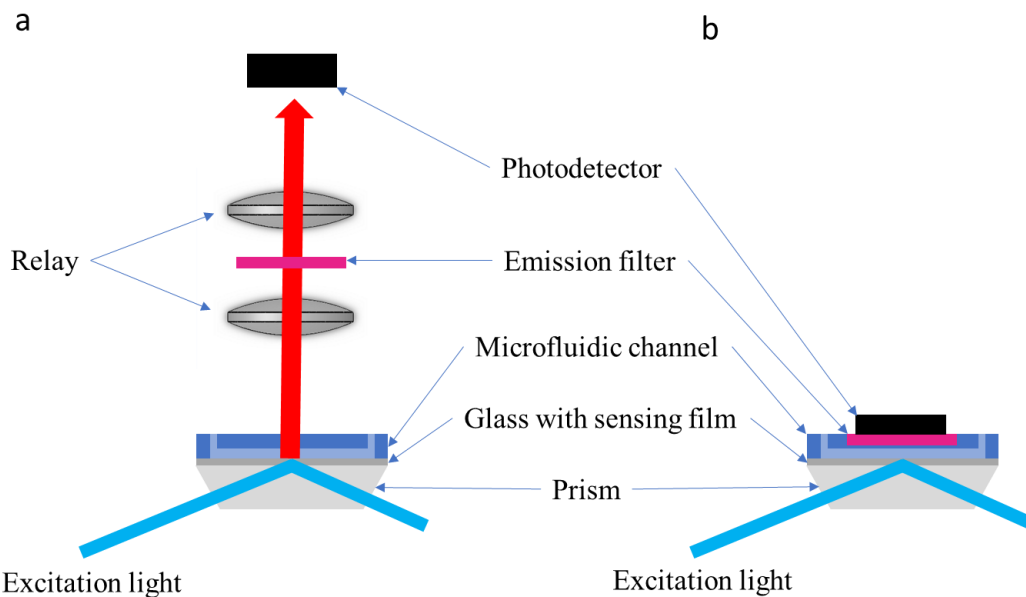


Figure 5-1. A potential solution for coupling of emission light. (a) The schematic of the current design for collection of emission light. The relay in the current design is expensive, low-efficient, and increasing the size of device. (b) A potential compact design for collection of emission lights. Emission lights can be detected by a photoelectronic placed closed to the microfluidic channel.

5.1.1.3 Potential Applications

This fluorescence-based optofluidic platform could be modified to realize the detection of other chemical elements in the water.

In addition to dissolved oxygen, a variety of dissolved gases can be detected by measuring the fluorescence emitted from thin sensing films which contains gas sensitive fluorophores and gas permeable matrices. For instance, free chlorine silicone can be detected using a film with Ru-bipy and a silicone rubber matrix [5]. Dissolved ammonia can be detected using a film with Ir-coumarin complex and a cellulose esters matrix [6]. To realize the TIR design, the wedged angle of the prism and the incident angle of the excitation beam need to be readjusted according to the refraction index of the sensing films.

Some fluorescence-based sensing relies on the chemical reaction between target chemical elements and induced reagents in the fluidic channel, such as

microcystin detection with fluorescent enzyme [7] and heavy-metal ions detection with rhodamine dye [8]. The proposed optofluidic platform can be modified for measuring fluorescence that is emitted from the fluidic channel. When the excitation light is coupled with a proper incident angle, the excitation light can be guided into a fluidic channel and confined in the microfluidic chip, as shown in the **Figure 5-2**.

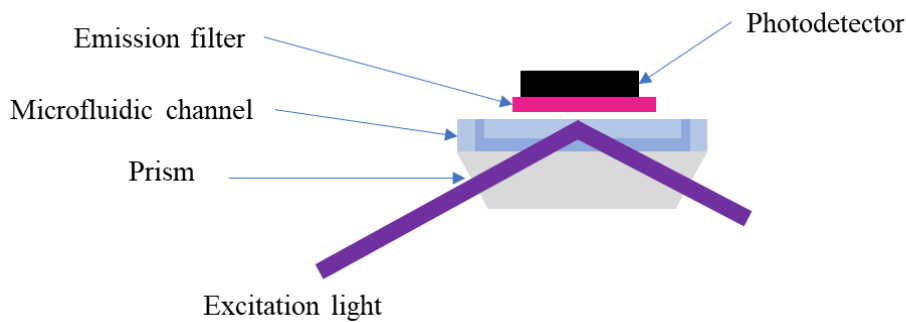


Figure 5-2. The schematic of a compact design for fluorescence sensing. The excitation light interacts with fluidic sample, while confined with in a sensing chip.

5.1.2 Imaging-based Optofluidic Platform

A dual-modality imaging optofluidic device is developed for onsite phytoplankton analysis in **Chapter 3**. While experiments with *Chlamydomonas*, *Euglena*, 10 μm polystyrene beads, and mix samples have demonstrated the feasibility of the device design, this prototype is not powerful enough to analyze natural water samples since the current algorithms are designed for a simplified scenario where only three types of particles are presented. Thus, development of imaging/video processing algorithms that can detect, track, and identify a variety of microbes in natural water samples is the first priority. The algorithms shall include three main image processing technologies: object detection, object tracking, holographic reconstruction. These imaging/video processing technologies are described in the following paragraphs. Furthermore, cameras and fluidic channel

were discussed.

5.1.2.1 Object Detection Algorithms

Object detection is an image processing technology for detecting and locating instances of objects of a certain class. HOG feature descriptors and SVM are used to realize object detection in the imaging-based optofluidic platform, as presented in **Chapter 3**. The main advantages of using this approach include high speed and simplicity. However, the spatial resolution of object localization is low, leading to a poor accuracy for object classification and object tracking. As shown in **Figure 5-3**, the raw image is divided into small connected cells, and HOG is compiled on each cell. Then the SVM classifier can determine the existence of objects of a certain class in a sliding window. As a result, the spatial resolution of localization is limited by the size of the cell, which is the smallest unit in the sliding window. Furthermore, the dimension and shape of the object cannot be evaluated, since the SVM was compiled on the sliding window with a fixed dimension. Thus, the performance of the current approach was not good enough when a variety of microbes with wide size ranges are present in the water channel.

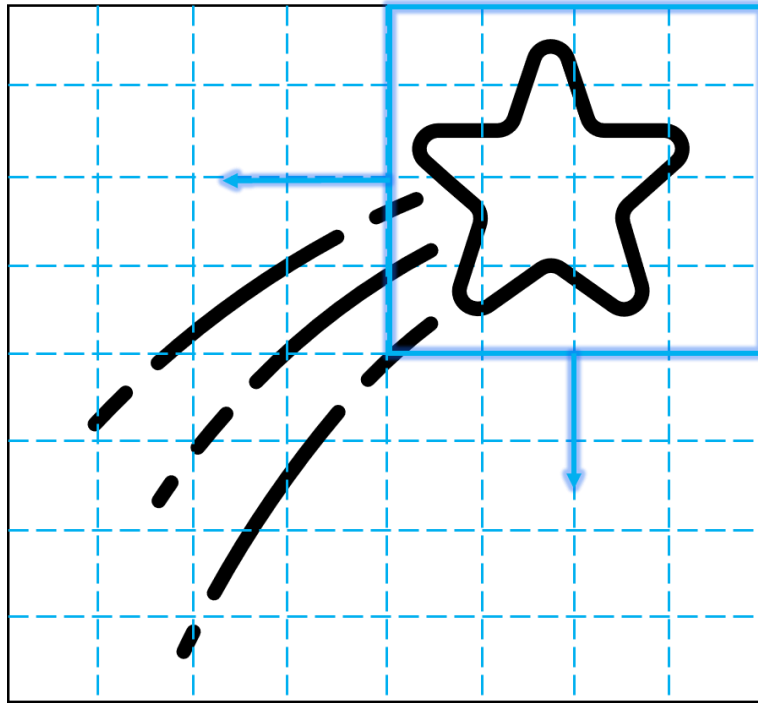


Figure 5-3. Object detection using HOG and SVM. In this example, an image is divided into 8x8 connected cells. A sliding window consisting of 4x4 cells are used to detect and locate instances of objects of a certain class.

Convolutional neural networks (CNN) have been widely used in object detection [9]. The main component of a CNN is the convolutional layer which produces feature maps using the convolution operation by sliding filters over the input image. After the convolutional layers, pooling layers are usually applied to reduce the dimensionality of the feature map. After multiple convolutions and pooling, fully connected layers are commonly added to deal with the feature map. Thus, both regression and classification problems can be solved. Many deep learning architectures have been proposed for object detection. Here, we identified two deep learning-based solutions that can improve object detection in the proposed optofluidic imaging device.

- (i) PP-Yolo

In PP-Yolo, a ResNet, which is a CNN with skipped connections, is used to extract feature maps at different scales [10]. Then, the selected feature maps obtained are sent to a feature pyramid network (FPN) to build a feature pyramid [11]. Finally, a detection head predicts the class of the object as well as the objectless score of each pixel in the feature pyramid. Moreover, a box bounding regression is performed to indicate the location and the dimension of the object with a high spatial resolution.

(ii) Mask R-CNN

Mask R-CNN realizes object detection using two stages [12]. At the first stage, the region of interest is predicted using a feature map output from a CNN. At the second stage, mask R-CNN predicts the class of the object, box bounding and binary masks according to the region of interest proposed from the first stage. Since this generates masks at the pixel level rather than a bounding box, the outline of an object can be obtained. However, mask R-CNN is slower than PP-Yolo and training a mask R-CNN model require more data.

5.1.2.2 Object Tracking Algorithms

Object tracking is a process of locating the moving object in the sequential frames using initial set of object detections [13]. It is essential for cells counting in imaging-based flow cytometry. Correlation filters are used to achieve object tracking in the imaging-based optofluidic platform as presented in **Chapter 3**. In this approach, the correlation output is calculated using the convolution of input cropped holograms and correlation filters. Then the object localization in the sequential frames can be achieved by finding the maximum in the correlation output maps.

However, the raw hologram shows ring-shaped optical fringes, resulting in multiple local maximums in the correlation output maps. Therefore, the current tracking algorithm is not efficient and false tracking results often occur. We believe that CNN-based trackers are feasible solutions to improve the tracking algorithms

[13]. Firstly, the convolutional layers are used to extract features from raw holograms. Secondly, a correlation filter is generated using the output features maps. Thirdly, a response map can be obtained using the cross-correlation of correlation filter and features maps. Finally, the maximum in the response map can refer the position of the object.

Overlapping issue also have a significant impact on the object tracking. The object overlapping could result in a false object detection or a missing observation. Here, we identify two potential solutions to address this issue. (i) Developing a decision-making strategy for multi-object tracking problem using a Markov Decision Process (MDP) framework [14]. (ii) Alternatively, object tracking could be improved using optical flow which refers to the pixelwise apparent velocities of the movement of an image pattern [15].

5.1.2.3 Holographic Reconstruction

The developed object detection algorithms rely on raw holograms captured by the imaging-based optofluidic platform, as presented in **Chapter 3**. However, raw holograms could be inefficient for modeling since detailed morphology features cannot be observed directly from holograms. Furthermore, the distances between particles and an imaging sensor can affect holographic patterns, creating challenges in the modeling. Holographic reconstruction is a good solution to address this problem.

Practical methods for reconstruction of in-line digital holograms have been presented [16]. An object is considered as an object plane which is described by a transmission function in which attenuation and phase delay are varied spatially. Then the wave propagation can be described by the Fresnel-Kirchhoff diffraction formula [16]. Several technologies are developed to model propagation of a wave field and retrieve the transmission function, such as angular spectrum methods [16]. However, it is difficult to localize the object plane before holographic reconstruction since the distance between the particles and imaging

sensor is unknown in an imaging-based flow cytometer without hydrodynamic focusing. Therefore, reconstructing a stack of images in multiple planes with a variety of distances are typically required. Then an optimal reconstructed image and object plane can be obtained based on the sharpness of each reconstructed image. This approach is effective but computationally intensive.

Compared with traditional holographic microscopes, imaging-based flow cytometers need rapid imaging processing algorithms since particles are flowing through the fluidic channel. The computationally intensive reconstruction processing may reduce the sensing throughput which is crucial to detection of rare cells in the fluidic sample. With the rapid development of deep learning, the reconstruction processing could be speed-up, while maintaining high performance [17, 18]. Herein, we proposed two potential architectures for rapid holographic reconstruction as shown in the **Figure 5-4**.

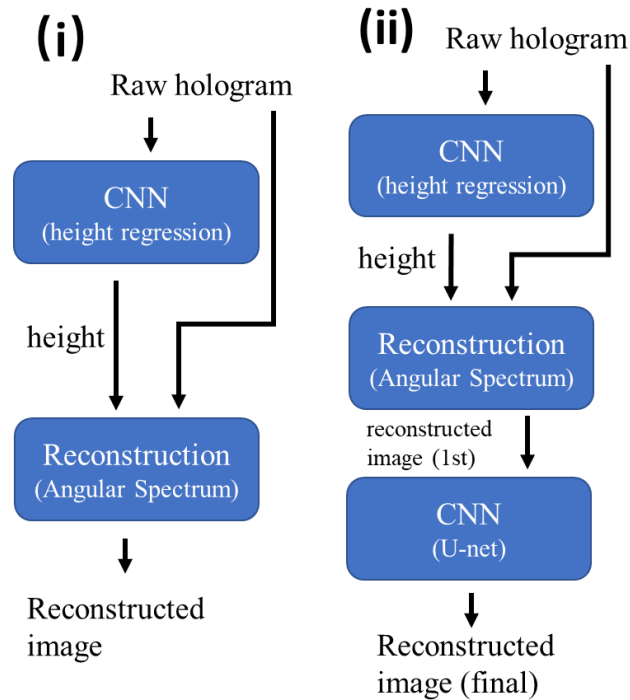


Figure 5-4. Two potential architectures for rapid holographic reconstruction.

(i) Autofocusing with deep learning

In this approach, CNN-based autofocusing is performed before conventional holographic reconstruction. We can cast the autofocusing as a regression problem. The focal distance, i.e., the distance between the object plane and imaging sensor can be predicted by a CNN model by providing an input raw hologram. Then the angular spectrum method can be used to retrieve amplitude and phase images in an object plane with a predicted focal distance. This approach can reduce execution times dramatically since it eliminates reconstructing a stack of images out of the focused plane and calculating the sharpness of each reconstructed images.

(ii) Autofocusing and image enhancement with deep learning

There are three steps in this approach. The first two steps are autofocusing and reconstruction using the angular spectrum method which are similar with the first architecture. The error of the predicted focal distance can result in residential fringes and blurring in the reconstructed images. To mitigate the effect of this error, the third step is applied. A U-Net CNN can be used to enhance the images by suppressing residential fringes and providing edge enhancement [19].

5.1.2.4 Discussion of Cameras

Image sensor are essential components in the dual-modality imaging platform. In the current platform, the volumetric throughput and morphology observation are limited by the performance of pi cameras. The desired image sensor in the existing platform were discussed.

In terms of fluorescence mode, image sensors with high ISO and high frame rate are desired. ISO (international standards organization) sensitivity is a measure of the camera's ability to capture light. In the existing platform ISO was set to 800 which is the maximum. If ISO can be raised, same exposure can be achieved with a short exposure time which can reduce the effect of motion blurring. High frame

rate is essential to high throughput since particles shall take less time to flow through the field of view.

In terms of lensless imaging mode, image sensors with low readout noise, small pixel size, large dimension, and high frame rate are recommended. Readout noises depend on photo shot noise, dark current, fixed pattern noise, and other noises. Low readout noise is necessary for acquiring high-quality holograms. The spatial resolution of a reconstructed image is equal to the resolution of a raw hologram. Thus, small pixel size is essential to morphology observation. Large dimension and high frame rate are desired, since they contribute to a high volumetric throughput.

5.1.2.5 Discussion of Fluidic Channel

Regarding fluidic channel, a channel with a larger thickness is expected to increase the volumetric throughput. Coarse filtrations could be used to prevent clogging, meanwhile allow microbes and small particles get into the channel. Anti-biofouling coating could be implemented to enlarge working lifetime of channel. Furthermore, regular natural water flushing could be used to remove some of cells and particles attached to the fluidic channel, combating biofouling issues. Experiment will be conducted to optimize the cleaning protocol and enlarge the working lifetime of fluidic channel.

5.1.3 FLIM under Low-Cost CMOS Format

Luminescence with long lifetime (20-50 us) are measured to demonstrate a novel FLIM approach under a low-cost CMOS format in **Chapter 4**. A lifetime precision of 580 ns is obtained at a sampling frequency of 1 Hz. However, majority of fluorophores and phosphors possess shorter emission lifetimes. Thus, it is desirable to explore methods to improve the precision of lifetime measurement. Moreover, the potential applications of this FLIM approach are discussed.

5.1.3.1 Improvements of lifetime measurement

Here, we identify four potential solutions to precision of lifetime measurement.

(i) Increasing the sampling rate

The sampling rate in the proposed FLIM approach is mainly limited by the speed of the CMOS imager, i.e., the execution time for a camera module to read one line of pixels on the CMOS imager. High-speed and low-cost cameras can be used to improve the sampling rate.

(ii) Increasing the number of frames used in the moving average

Moving averages can reduce random noise by averaging a number of fluorescence lifetime maps calculated from captured frames. Thus, the error shall be suppressed when more frames are used. However, increasing the number of frames also increases the response time of the device.

(iii) Using large sub-images

In the current approach, the whole image is split into an array of sub-images which each contain three optical fringes. Then the fluorescence lifetime is calculated in each sub-image using the phase results of the FFT. The sub-image can be enlarged to include more integers of optical fringes, thus the precision of the FFT phase result can be improved. However, larger sub-image has a negative impact on the spatial resolution of calculated fluorescence lifetime maps.

(iv) Improving calibration methods

In the current work, the phase shift between excitation and emission was calculated using the FFT. However, the amplitude of excitation and emission signals was spatially varying due to a non-uniform excitation spot. Therefore, additional errors are added in the FFT results since the inputs were not stationary signals. Thus, development of calibration methods for combating non-uniform excitation spot was identified as a promised solution to minimize these errors.

5.1.3.2 Development of Time-Gate Method

The developed FLIM approach is based on the frequency domain method and phase shift measurements. Thus, both excitation light and emission light need to be measured simultaneously by one imaging sensor. As a result, the camera FoV was split into a sample area and a reference area, increasing the difficulty of optical design. To simplify the optical path and optomechanical components, time-gated methods under the low-cost CMOS format can be developed to eliminate the need of measurements of excitation light. The CMOS exposures with rolling shutters can be regarded as a time-gated windows. The width of the time-gated window is equal to the CMOS exposure duration; Time-gated windows are scanned as each line of pixels is activated sequentially. Thus, the fluorescence/luminescence lifetime can be calculated with the emission intensities in the two time-gated windows that corresponds to the pixel values of two lines, as shown in **Figure 5-5**.

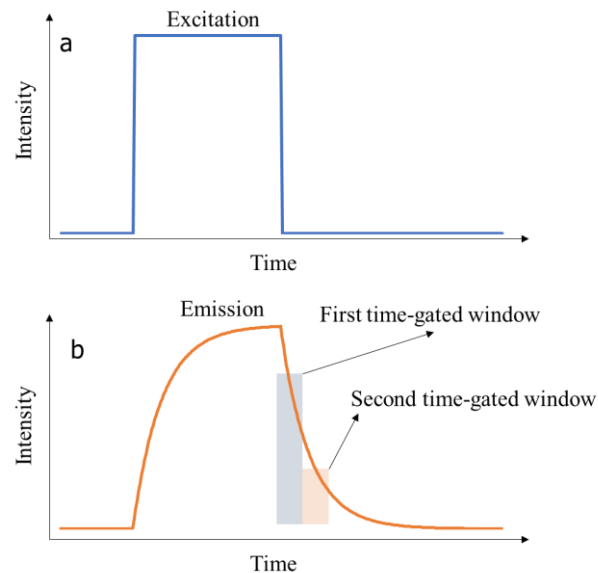


Figure 5-5. Illustration of a time-gated method for TRF. (a) Excitation signals with square waves and (b) corresponding emission signals are shown. The fluorescence lifetime can be calculated with the emission intensities measured in the two time-gated windows. This approach does not require

measurements of excitation signals.

In addition to TRF, the time-gated method under a low-cost CMOS format could be used to detect the fluorophores with long-lifetime emission, while eliminating the effect of short-lifetime emissions. The emission curves of two types of fluorophores are illustrated in **Figure 5-6**. A proper time-gated window can detect the fluorescence with long-lifetime and reject the fluorescence with short-lifetime. Typically, the autofluorescence generated from organisms and biological structures possess a short lifetime (a few nanoseconds). Therefore, this method could be used to mitigate the background autofluorescence for optofluidic devices which use extrinsic fluorescent analytes with long lifetime.

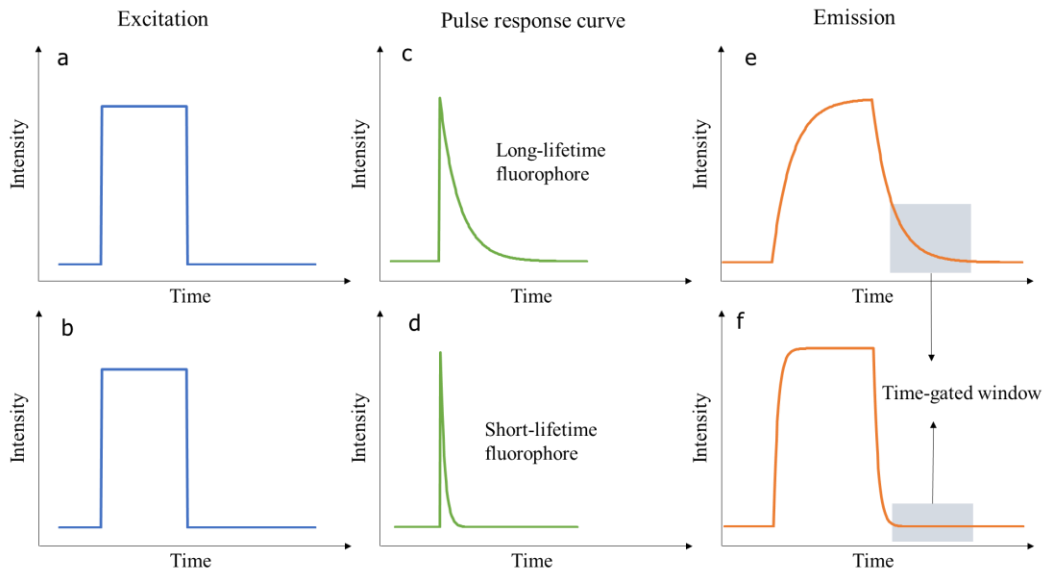


Figure 5-6. Detection of long-lifetime fluorophores with suitable time-gated window. (a, b) Intensity of excitation light. (c, d) pulse response curve of a long-lifetime fluorophore and a short-lifetime fluorophore. (e, f) The curve of emission light generated by a long-lifetime fluorophore and a short-lifetime fluorophore using the shown excitation lights.

5.1.3.3 Potential Applications

The FLIM approach presented in this thesis can be applied into existing optofluidic imaging devices that already have capability of fluorescence imaging.

Since this FLIM approach is compatible with low-cost CMOS, TRF could be realized to improve microbe detection and chemical analysis without changing hardware in the existing optofluidic imaging devices.

Regarding optofluidic fluorescence sensing, integration of sensor arrays on an optofluidic chip has advanced the performance of chemical analysis [20]. For instance, a sensor array with eight chambers can provide discrimination capability of eight different heavy-metal ions at same concentration as low as 50 μM [21]. The FLIM approach presented in this thesis is well-suited for sensor arrays, since it provides spatial resolution for detection of multiple chambers on a chip and enables TRF measurement with low-cost and portable devices. A potential design is illustrated in **Figure 5-7**.

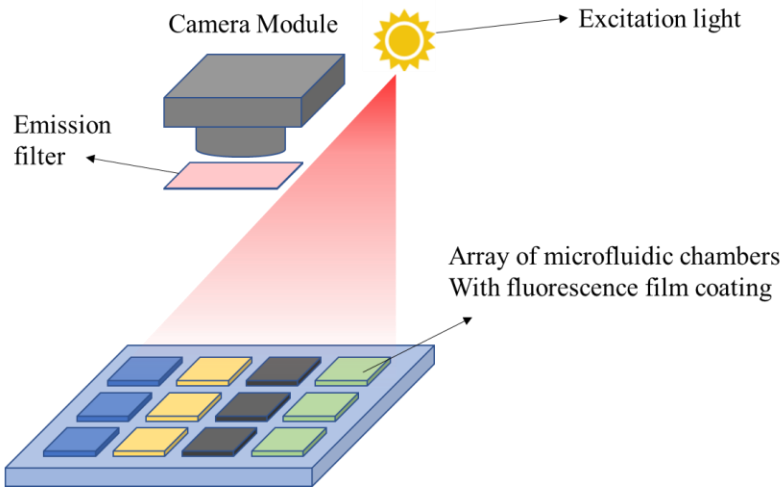


Figure 5-7. A potential optofluidic design that use the FLIM approach under a low-cost CMOS format. All of chambers on a chip can be measured by a camera module.

5.2 Contribution

My research contributions to the field of optofluidic devices are:

- (i) Developed a fluorescence-based optofluidic platform using frequency domain TRF. DO measurements are performed to demonstrate the

- efficiency of this platform in onsite chemical sensing.
- (ii) Provided a fluorescence enhancement approach for fluorescence-based optofluidic devices using a TIR design and prism assisted coupling mechanism. This approach can improve overall sensitivity and minimize background fluorescence.
 - (iii) Developed an imaging-based optofluidic platform that is capable of automated cell counting and cell classification. Phytoplankton analysis is performed to demonstrate the efficiency of this platform in onsite microbe detection.
 - (iv) Provided a dual-modality imaging approach for imaging-based optofluidic platforms. Both morphology and fluorescence features of microbes can be observed with portable and low-cost imaging devices.
 - (v) Developed a FLIM approach under a low-cost CMOS format. This approach allows integrating a FLIM module in portable and low-cost optofluidic platforms for onsite monitoring.

5.3 Conclusion

The work presented in this thesis is dedicated to the development of the optofluidic devices for onsite water quality monitoring. The common optofluidic technologies used for chemical analysis and microbe detection were described in **Chapter 1**. We developed two optofluidic platforms for onsite water quality monitoring: a fluorescence-based optofluidic platform for chemical analysis and an imaging-based optofluidic platform for microbe detection (**Chapter 2, 3**). There has been a collection of advances that can make optofluidic devices compatible for onsite monitoring applications. The stability and sensitivity of fluorescence sensing were improved by applying frequency domain TRF and a prism assisted excitation coupling approach (**Chapter 2**). A portable and low-cost imaging system with dual modalities was developed to observe morphology and fluorescence features for

microbe detection, while eliminating bulky microscopy setup (**Chapter 3**). A low-cost and portable FLIM approach that relies on CMOS imagers with ERS was developed, allowing FLIM-based measurements in portable optofluidic devices (**Chapter 4**). Recommended future works on improving sensing performance, device miniaturization, and potential applications were discussed in **Chapter 5**. The findings of this thesis will act as a springboard to inform future applications of onsite monitoring using optofluidic devices.

References

- [1] Quaranta M, Borisov SM, Klimant I. Indicators for optical oxygen sensors. *Bioanalytical reviews*. 2012 Dec 1;4(2-4):115-57.
- [2] Mahoney EJ, Hsu HH, Du F, Xiong B, Selvaganapathy PR, Fang Q. Optofluidic dissolved oxygen sensing with sensitivity enhancement through multiple reflections. *IEEE Sensors Journal*. 2019 Aug 2;19(22):10452-60.
- [3] Amao Y. Probes and polymers for optical sensing of oxygen. *Microchimica Acta*. 2003 Sep 1;143(1):1-2.
- [4] Grist SM, Chrostowski L, Cheung KC. Optical oxygen sensors for applications in microfluidic cell culture. *Sensors*. 2010 Oct;10(10):9286-316.
- [5] Brook TE, Narayanaswamy R. Polymeric films in optical gas sensors. *Sensors and Actuators B: Chemical*. 1998 Aug 31;51(1-3):77-83.
- [6] Waich K, Borisov S, Mayr T, Klimant I. Dual lifetime referenced trace ammonia sensors. *Sensors and Actuators B: Chemical*. 2009 May 20;139(1):132-8.
- [7] Fontal OI, Vieytes MR, de Sousa JB, Louzao MC, Botana LM. A fluorescent microplate assay for microcystin-LR. *Analytical biochemistry*. 1999 May 1;269(2):289-96.
- [8] Rasheed T, Bilal M, Nabeel F, Iqbal HM, Li C, Zhou Y. Fluorescent sensor based models for the detection of environmentally-related toxic heavy metals. *Science of the Total Environment*. 2018 Feb 15;615:476-85.

- [9] Ren S, He K, Girshick R, Sun J. Faster r-cnn: Towards real-time object detection with region proposal networks. In *Advances in neural information processing systems 2015* (pp. 91-99).
- [10] He K, Zhang X, Ren S, Sun J. Deep residual learning for image recognition. In *Proceedings of the IEEE conference on computer vision and pattern recognition 2016* (pp. 770-778).
- [11] Long X, Deng K, Wang G, Zhang Y, Dang Q, Gao Y, Shen H, Ren J, Han S, Ding E, Wen S. PP-YOLO: An Effective and Efficient Implementation of Object Detector. *arXiv preprint arXiv:2007.12099*. 2020 Jul 23.
- [12] He K, Gkioxari G, Dollár P, Girshick R. Mask r-cnn. In *Proceedings of the IEEE international conference on computer vision 2017* (pp. 2961-2969).
- [13] Bolme DS, Beveridge JR, Draper BA, Lui YM. Visual object tracking using adaptive correlation filters. In *2010 IEEE computer society conference on computer vision and pattern recognition 2010 Jun 13* (pp. 2544-2550). IEEE.
- [14] Xiang Y, Alahi A, Savarese S. Learning to track: Online multi-object tracking by decision making. In *Proceedings of the IEEE international conference on computer vision 2015* (pp. 4705-4713).
- [15] Mikic I, Krucinski S, Thomas JD. Segmentation and tracking in echocardiographic sequences: Active contours guided by optical flow estimates. *IEEE transactions on medical imaging*. 1998 Apr;17(2):274-84.
- [16] Latychevskaia T, Fink HW. Practical algorithms for simulation and reconstruction of digital in-line holograms. *Applied optics*. 2015 Mar 20;54(9):2424-34.
- [17] Lee SJ, Yoon GY, Go T. Deep learning-based accurate and rapid tracking of 3D positional information of microparticles using digital holographic microscopy. *Experiments in Fluids*. 2019 Nov 1;60(11):170.
- [18] Shao S, Mallery K, Kumar SS, Hong J. Machine learning holography for 3D particle field imaging. *Optics Express*. 2020 Feb 3;28(3):2987-99.

- [19] Wu Y, Rivenson Y, Wang H, Luo Y, Ben-David E, Bentolila LA, Pritz C, Ozcan A. Three-dimensional virtual refocusing of fluorescence microscopy images using deep learning. *Nature methods*. 2019 Dec;16(12):1323-31.
- [20] Lin Y, Gritsenko D, Feng S, Teh YC, Lu X, Xu J. Detection of heavy metal by paper-based microfluidics. *Biosensors and Bioelectronics*. 2016 Sep 15;83:256-66.
- [21] Feng L, Li X, Li H, Yang W, Chen L, Guan Y. Enhancement of sensitivity of paper-based sensor array for the identification of heavy-metal ions. *Analytica Chimica Acta*. 2013 May 30;780:74-80.